NASA Technical Memorandum 89428
USAAVSCOM Technical Memorandum 87-A-2

Frequency-Response Identification of XV-15 Tilt-Rotor Aircraft Dynamics

Mark B. Tischler

(NASA-TM-89428) FREQUENCY-RESPONSE
IDENTIFICATION OF XV-15 TILT-ROTOR AIRCRAFT
DYNAMICS (NASA) 191 p Avail: NTIS HC
A09/MF A01 CSCL 01C G3/08

N87-22690

Unclas
0076036

May 1987

National Aeronautics and
Space Administration

US ARMY
AVIATION
SYSTEMS COMMAND
AVIATION RESEARCH AND
TECHNOLOGY ACTIVITY

NASA Technical Memorandum 89428 USAAVSCOM Technical Memorandum 87-A-2

Frequency-Response Identification of XV-15 Tilt-Rotor Aircraft Dynamics

Mark B. Tischler, Aeroflightdynamics Directorate
U.S. Army Aviatiation Research Technology Activity
Ames Research Center, Moffett Field, California

May 1987

National Aeronautics and
Space Administration

Ames Research Center
Moffett Field, California 94035

US ARMY
AVIATION
SYSTEMS COMMAND

AVIATION RESEARCH AND
TECHNOLOGY ACTIVITY
MOFFETT FIELD, CA 94305-1099

FREQUENCY-RESPONSE IDENTIFICATION OF XV-15 TILT-ROTOR AIRCRAFT DYNAMICS

A DISSERTATION
SUBMITTED TO THE
DEPARTMENT OF AERONAUTICS AND ASTRONAUTICS
AND THE COMMITTEE ON GRADUATE STUDIES
OF STANFORD UNIVERSITY
IN PARTIAL FULFILLMENT OF THE REQUIREMENTS
FOR THE DEGREE OF
DOCTOR OF PHILOSOPHY

By
Mark B. Tischler
May 1987

I certify that I have read this thesis and that in my opinion it is fully adequate, in scope and quality, as a dissertation for the degree of Doctor of Philosophy.

A. E. Bryson

(Principal Adviser)

I certify that I have read this thesis and that in my opinion it is fully adequate, in scope and quality, as a dissertation for the degree of Doctor of Philosophy.

J. Victor Lebacqz

I certify that I have read this thesis and that in my opinion it is fully adequate, in scope and quality, as a dissertation for the degree of Doctor of Philosophy.

Gene F. Franklin

(Electrical Engineering)

Approved for the University Committee
on Graduate Studies:

Dean of Graduate Studies

ACKNOWLEDGMENTS

My return to academic life has allowed me to broaden my background and learn from the foremost leaders in the aerospace field. I wish to thank my advisor, Professor Arthur E. Bryson, Jr., for supporting and encouraging my research interests from the outset of my program at Stanford. Through Professor Bryson's courses, I have deepened my appreciation of the value of clear physical explanations and fundamental principles.

I have greatly benefited from the nonlinear and digital courses given by Professor Gene F. Franklin. Thank you, also, for being a reader of my dissertation and providing consistent support.

Special thanks go to two people who have been my advisors, colleagues, and friends over the last four years. Dr. J. Victor Lebacqz and Dr. Robert T. N. Chen have shared much of their time and experience, and have continuously challenged me to be complete and precise. Thank you for all that you both have done for me.

Special thanks also go to my friend and colleague Dr. Joseph G. M. Leung for contributing many ideas and long hours during our development of the FRESPID program.

I am grateful to the U.S. Army Aeroflightdynamics Directorate, my supervisors Mr. David L. Key and Dr. Fred H. Schmitz, and the Tilt-Rotor Project Office for providing financial and technical support.

Thanks also go to Catharine P. Levin, who spent many late evenings preparing the initial draft of this dissertation. I am also indebted to the NASA Publications Branch, Graphics Branch, and D-K Associates for their efforts in the production of the final version.

I dedicate this work to my father, Morris Tischler, and the memory of my mother, Ruth Judith Tischler, and my grandparents, Herbert and Minnie Shafer, who instilled in me the resolve to strive to achieve to the best of my ability.

FREQUENCY-RESPONSE IDENTIFICATION OF XV-15 TILT-ROTOR AIRCRAFT DYNAMICS

Mark B. Tischler, Ph.D.

Stanford University, 1987

The timely design and development of the next generation of tilt-rotor aircraft (JVX) depend heavily on the in-depth understanding of existing XV-15 dynamics and the availability of fully validated simulation models. Previous studies have considered aircraft and simulation trim characteristics, but analyses of basic flight vehicle dynamics have been limited to qualitative pilot evaluations. The present study has the following objectives:

1. Documentation and evaluation of XV-15 bare-airframe dynamics
2. Comparison of aircraft and simulation responses
3. Development of a validated transfer-function description of the XV-15 needed for future studies

A nonparametric frequency-response approach is used which does not depend on assumed model order or structure. Transfer-function representations are subsequently derived which fit the frequency responses in the bandwidth of greatest concern for piloted handling-qualities and control-system applications.

This study involved the planning and execution of flight tests on the XV-15 aircraft and piloted-simulation for four flight conditions from hover to cruise. Improved test techniques and pilot-training procedures were devised. Analytical software tools were developed (or adapted) which allow the identification of high-resolution spectral responses and the derivation and validation of multi-input/multi-output transfer-function models. These techniques were applied in an extensive evaluation of the open-loop flight dynamics of the XV-15 aircraft and simulation mathematical models. Deficiencies in the mathematical models were exposed and documented. Finally, a new, fully validated transfer-function model was derived for the hover and cruise flight conditions. The methods developed in this study have subsequently been applied in a number of other flight-test programs and have been included in the U.S. Army's updated helicopter handling-qualities specification.

Approved for publication:

By A. E. Bry
For Major Department

By
Dean of Graduate Studies

TABLE OF CONTENTS

Page

CHAPTER 1 INTRODUCTION....................................1

1.1 Background and Objectives....................................1

1.2 Dynamics Identification Methods....................................4

1.3 A Historical Summary of Research in Frequency-Response Identification....................................7

1.4 Scope of Research....................................9

1.5 Extensions and Applications....................................10

1.6 Organization of Dissertation....................................11

CHAPTER 2 XV-15 RESEARCH AIRCRAFT AND FLIGHT TEST CONDITIONS.........13

2.1 Aircraft Description....................................13

2.2 Flight Test Conditions....................................20

CHAPTER 3 FREQUENCY-DOMAIN IDENTIFICATION METHOD....................23

3.1 Flight Test Technique....................................23

3.2 Frequency-Response Identification....................................25

3.3 Transfer-Function Modeling....................................48

3.4 Time-Domain Verification of Transfer-Function Models........51

CHAPTER 4 HOVER DYNAMICS....................................55

4.1 Lateral/Directional Dynamics....................................56

4.2 Longitudinal Dynamics....................................84

4.3 Verification of Open-Loop Transfer-Function Models for Hover....................................92

CHAPTER 5 CRUISE DYNAMICS....................................102

5.1 Lateral/Directional Dynamics....................................103

5.2 Longitudinal Dynamics....................................115

5.3 Verification of Transfer-Function Models....................127

CHAPTER 6 CONCLUSIONS....................133
  6.1 Analysis of the XV-15....................133
  6.2 Frequency-Response Identification Method....................135
CHAPTER 7 RECOMMENDATIONS FOR FUTURE STUDY....................136
  7.1 Reconstruction of Physical Stability Derivative Parameters....................136
  7.2 Generalization to MIMO Systems....................137
APPENDIX A CHIRP z-TRANSFORM....................139
  A.1 Resolution....................140
  A.2 Starting Frequency....................141
  A.3 Window Size....................142
APPENDIX B LIMITATIONS IN CLOSED-LOOP IDENTIFICATION....................143
  B.1 Spectral Relationships....................143
  B.2 Numerical Study....................149
  B.3 Conclusions of Closed-Loop Identification Study....................161
REFERENCES....................163

LIST OF TABLES

Table | Page
4.1 Identified Transfer-Function Models for Hover................101
5.1 Summary of Identification Results for Cruise................114

LIST OF ILLUSTRATIONS

Figure Page

1.1. The XV-15 Tilt-Rotor Aircraft. (a) Hover Configuration; (b) Cruise Configuration........2

1.2. Time-Domain Identification Method........4

1.3. Frequency-Response Identification Method........6

2.1. Three-View Layout of XV-15 Tilt-Rotor Research Aircraft......14

2.2. Airspeed-Altitude Envelope........15

2.3. Conversion Corridor........16

2.4. Control Method for Helicopter-Mode Flight........17

3.1. Typical Lateral-Stick Frequency Sweep (δ_{LAT})........24

3.2. Flowchart of Computational Procedures Performed by the FRESPID Program........27

3.3. Sample Command File for FRESPID........28

3.4. Single-Input/Single-Output Open-Loop Response Identification........33

3.5. Uncorrelated Measurement Noise at the Input and Output.......36

3.6. Effect of Secondary Inputs on Single-Input/Single-Output Identification........38

3.7. Single Degree-of-Freedom Closed-Loop Roll-Response Model.....39

3.8. Coupled Roll/Yaw Response Model........43

4.1. Two Lateral-Stick Frequency-Sweeps (δ_{LAT}) in Hover...........56

4.2. Lateral-Stick Input Autospectrum ($G_{\delta_{LAT}\delta_{LAT}}$)........57

4.3. Aileron Surface Deflections (δ_a) during the Lateral-Stick Frequency Sweeps, Reflecting Contributions from Pilot and SCAS Inputs........58

4.4. Aileron Surface Input Autospectrum ($G_{\delta_a\delta_a}$)........58

4.5. Roll-Rate Response (p) during Lateral-Stick Frequency-Sweeps....59

4.6. Roll-Rate Output Autospectrum (G_{pp})....59

4.7. Magnitude of Cross-Spectrum between Aileron Surface Inputs and Roll-Rate Response ($G_{\delta_a p}$)....60

4.8. Roll-Rate Response to Aileron ($p/-\delta_a$). (a) Magnitude; (b) Phase....61

4.9. Coherence Function for Roll-Rate Response Identification ($\gamma^2_{\delta_a p}$)....61

4.10 Comparison of Small-Perturbation Transfer-Function and Frequency-Sweep Responses Obtained from the Simulation; Data Presented are for the Roll-Rate Response to Ailerons, $p/-\delta_a$. (a) Magnitude; (b) Phase....64

4.11. Yaw-Rate Response to Rudder (r/δ_r). (a) Magnitude; (b) Phase....66

4.12. Coherence Function for Yaw-Rate Response Identification ($\gamma^2_{\delta_r r}$)....66

4.13. Transfer-Function Model Identification for Yaw-Rate Response to Rudder (r/δ_r). (a) Magnitude; (b) Phase....69

4.14. Transfer-Function Model Identification for Roll-Rate Response to Ailerons ($p/-\delta_a$). (a) Magnitude; (b) Phase....72

4.15. Locations of Roll-Response Transfer-Function Parameters in the s-Plane....73

4.16. Yaw-Rate Response (r) during Lateral-Stick Frequency Sweeps....75

4.17. Aileron Surface Input Autospectrum 75

4.18. Yaw-Rate Output Autospectrum 76

4.19. Magnitude of Cross-Spectrum between Aileron Surface Inputs and Yaw-Rate Response 77

4.20. Yaw-Rate Response to Ailerons. (a) Magnitude; (b) Phase 77

4.21. Coherence Function for Yaw-Rate Response to Aileron Inputs ($\gamma^2_{\delta_a r}$) 78

4.22. Rudder Surface Deflections (δ_r) during the Lateral-Stick Frequency Sweeps 78

4.23. Coherence Function for Cross-Correlation between Aileron and Rudder Surface Inputs ($\gamma^2_{\delta_a \delta_r}$) 79

4.24. Partial Coherence Function for Yaw-Rate Response to Aileron Inputs ($\gamma^2_{\delta_a r \cdot \delta_r}$) 80

4.25. Multiple Coherence Function for Yaw-Rate Response to Combined Aileron and Rudder Surface Inputs ($\gamma^2_{\delta_a \delta_r : r}$) 81

4.26. Comparison of Flight-Test and Simulator Results for Yaw-Rate Response to Aileron (r/δ_a). (a) Magnitude; (b) Phase 84

4.27. Vertical-Acceleration Response to Power Lever ($-a_z/\delta_c$). (a) Magnitude; (b) Phase 85

4.28. Coherence Function for Vertical-Acceleration Response Identification ($\gamma^2_{\delta_c a_z}$) 86

4.29. Pitch-Rate Response to Elevator ($q/-\delta_e$). (a) Magnitude; (b) Phase 88

4.30. Coherence Function for Pitch-Rate Response Identification ($\gamma^2_{\delta_e q}$) 89

4.31. Roll-Response Model Verification Using SCAS-off Flight Data. (a) Aileron Input; (b) Roll-Rate....................94

4.32. Yaw-Response Model Verification Using SCAS-off Flight Data. (a) Rudder Input; (b) Yaw-Rate......................95

4.33. Lateral-Directional Model Verification (Roll SCAS-off, Yaw SCAS-on). (a) Aileron Input; (b) Rudder Input; (c) Roll-Rate; (d) Yaw-Rate...............................96

4.34. Vertical-Acceleration Response Model Verification. (a) Power Lever Input; (b) Vertical Acceleration...........97

4.35. Pitch-Response Model Verification Using SCAS-off Flight Data. (a) Elevator Input; (b) Pitch-Rate..................98

4.36. Pitch-Response Model Verification Using SCAS-on Flight Data. (a) Elevator Input; (b) Pitch-Rate..................99

5.1. Two Lateral Stick Frequency-Sweeps (δ_{LAT}) in Cruise. (a) Lateral Stick Inputs; (b) Roll-Rate..................104

5.2. Roll-Rate Response to Aileron ($p/-\delta_a$). (a) Magnitude; (b) Phase...105

5.3. Coherence Function ($\gamma^2_{\delta_a p}$) for Roll-Rate Response Identification..106

5.4. Sideslip Response to Rudder ($\beta_{cg}/-\delta_r$). (a) Magnitude; (b) Phase...107

5.5. Coherence Function ($\gamma^2_{\delta_r \beta_{cg}}$) for Sideslip Response Identification..107

5.6. Transfer-Function Model Identification for Roll-Rate Response to Aileron ($p/-\delta_a$). (a) Magnitude; (b) Phase...111

5.7. Transfer-Function Model Identification for Sideslip Response to Rudder ($\beta_{cg}/-\delta_r$). (a) Magnitude; (b) Phase....112

5.8. Location of Roll-Rate Transfer-Function (p/δ_a) Parameters in the s-Plane....113

5.9. Pitch-Rate Response to Elevator ($q/-\delta_e$). (a) Magnitude; (b) Phase....115

5.10. Coherence Function ($\gamma^2_{\delta_e q}$) for Pitch-Rate Response Identification....116

5.11. Vertical-Acceleration Response to Elevator (a_z/δ_e). (a) Magnitude; (b) Phase....118

5.12. Coherence Function ($\gamma^2_{\delta_e a_z}$) for Vertical-Acceleration Response Identification....119

5.13. Transfer-Function Model Identification for Pitch-Rate Response to Elevator ($q/-\delta_e$). (a) Magnitude; (b) Phase....122

5.14. Transfer-Function Model Identification for Vertical Acceleration Response to Elevator (a_z/δ_e). (a) Magnitude; (b) Phase....123

5.15. Roll-Response Model Verification Using SCAS-off Flight Data. (a) Aileron Input; (b) Roll-Rate....127

5.16. Sideslip-Response Verification Using SCAS-off Flight Data. (a) Rudder Input; (b) Sideslip Response....128

5.17. Pitch-Response Model Verification Using SCAS-off Flight Data (h_d = 2800 ft). (a) Elevator Input; (b) Pitch Rate....130

5.18. Pitch and Vertical-Acceleration Response Model Verification Using SCAS-on Flight Data (h_d = 12000 ft). (a) Elevator Input; (b) Pitch Rate; (c) Vertical-Acceleration Response....................................131

B.1. Closed-Loop Identification....................................144

B.2. Identification of Open-Loop Frequency-Response for the Nominal-Gain System, K = 3.0. (a) Magnitude; (b) Phase....................................151

B.3. Coherence Function for Open-Loop Roll-Rate Identification, Nominal-Gain System, K = 3.0....................................151

B.4. Identification of the Closed-Loop Frequency-Response for the Nominal-Gain System, K = 3.0. (a) Magnitude; (b) Phase....................................152

B.5. Coherence Function for Closed-Loop Response Identification, Nominal-Gain System, K = 3.0....................................152

B.6. Identification of the Open-Loop Frequency-Response for the High-Gain System, K = 6.5. (a) Magnitude; (b) Phase....................................153

B.7. Coherence Function for Open-Loop Response Identification, High-Gain System, K = 6.5....................................153

B.8. Identification of the Closed-Loop Frequency-Response for the High-Gain System, K = 6.5. (a) Magnitude; (b) Phase....................................154

B.9. Coherence Function for Closed-Loop Response Identification, High-Gain System, K = 6.5....................................154

B.10. Effect of Noise-to-Signal Ratios $\hat{\sigma} = 0, 0.1, 0.3$ on the Identification of the Open-Loop Frequency-Response for the Nominal-Gain System, $K = 3.0$. (a) Magnitude; (b) Phase; (c) Coherence....................................155

B.11. Effect of Noise-to-Signal Ratios $\hat{\sigma} = 0, 1.0, 10.0$ on the Identification of the Open-Loop Frequency-Response for the Nominal-Gain System, $K = 3.0$. (a) Magnitude; (b) Phase; (c) Coherence....................................156

B.12. Variation in the Total rms Errors with Noise-to-Signal Ratio for the Identification of the Open-Loop Frequency-Response. (a) Magnitude Error; (b) Phase Error...158

B.13. Variation in Normalized Bias Errors with the Noise-to-Signal Ratio for the Identification of the Open-Loop Frequency Response. (a) Normalized Gain Error; (b) Normalized Mode Location Error........................160

SYMBOLS

a_z	vertical acceleration, positive downward, g
b[ ]	bias error
E[ ]	expected value operator
f	frequency, Hz
G_{xx}, G_{yy}, G_{xy}	input autospectrum, output autospectrum, and cross-spectrum functions, respectively; the magnitudes of these "power-spectral" functions are plotted in power-dB = $10 \log_{10}\|G_{xx}\|$, etc.
$G_{xy.z}$, $G_{yy.z}$, $G_{xy.z}$	conditioned input autospectrum, output autospectrum, cross-spectrum with the linear effect of signal z removed; the magnitude of these "power-spectral" functions are plotted in power-dB = $10 \log_{10}\|G_{xy.z}\|$, etc.
H	frequency-response; the magnitude of the frequency-response functions are plotted in dB = $20 \log_{10}\|H\|$
H_d	density altitude, ft

i_N	engine nacelle incidence, $i_N = 0$ refers to cruise configuration, $i_N = 90$ refers to helicopter configuration
L	number of time-history points in the window
N	number of discrete frequency points provided by the Fourier transform algorithm
n	process-noise input
nr	number of multiple time-history records used in concatenation procedure
n_d	number of independent time-history averages
p	roll-rate, positive is right-wing down (looking from the rear forward), deg/sec
q	pitch-rate, positive is nose up, deg/sec
r	yaw-rate, positive is nose right (looking from the top), deg/sec
s	Laplace variable
S	signal-to-noise ratio

$1/T$	inverse time-constant, rad/sec
V_i, V_c, V_t	indicated airspeed, calibrated airspeed, true airspeed, respectively, knots
y/δ_x	frequency-response of output variable y to control input variable δ_x; the magnitude of this quantity is plotted in $\mathrm{dB} = 20 \log_{10}\lvert y/\delta_x \rvert$
$y/\delta_x . \delta_z$	frequency-response of y/δ_x with the linear effects of control δ_z removed; the magnitude of this quantity is plotted in $\mathrm{dB} = 20 \log_{10}\lvert y/\delta_x \cdot \delta_y \rvert$
β_{cg}	sideslip angle at the aircraft center-of-gravity; positive is relative wind from the right (as seen from the rear, forward), deg
γ^2_{xy}	coherence function between variable x and variable y
$\gamma^2_{xy \cdot z}$	partial coherence function between variable x and variable y with the linear effects of variable z removed
$\gamma^2_{xy:z}$	multiple coherence function indicating the total contribution of variables x and y to variable z

δ_a	aileron surface deflection; positive is right-aileron surface deflected down, which results in a negative roll-rate, deg
δ_c	power lever deflection; positive is power increase, which results in a negative vertical acceleration, %
δ_e	elevator surface deflection; positive is elevator trailing edge down which results in a negative pitch-rate, deg
δ_{LAT}	lateral stick deflection; positive is stick right, which results in a positive roll-rate, in.
δ_{LON}	longitudinal stick deflection; positive is stick forward, which results in a negative pitch-rate, in.
δ_{PED}	pedal deflection; positive is right pedal forward, which results in a positive yaw-rate, in.
δ_r	rudder surface deflection; positive deflection is rudder surface trailing edge to the right, which results in a positive yaw-rate, deg
Δf	frequency increment, Hz

Δt	time increment, sec
ε_b	normalized bias error
ε_r	normalized random error
ζ	damping ratio
σ	random error
$\hat{\sigma}$	noise-to-signal rms ratio
τ	time-delay, sec
ω	frequency, rad/sec

Abreviations

AFCS	automatic flight control system
ARC	Ames Research Center
c.g.	center of gravity
CZT	chirp z-transform
DFT	discrete Fourier transform

FFT	fast Fourier transform
FRESPID	frequency-response identification program
ICR	instantaneous center of rotation
LATFIT	transfer-function fitting program for lateral dynamics
LONFIT	transfer-function fitting program for longitudinal dynamics
MIMO	multi-input/multi-output
NAVFIT	generalized transfer-function fitting program
SCAS	stability and control augmentation system
TFTHISTORY	transfer-function time-history verification program
VMS	Vertical Motion Simulator (ARC)

Chapter 1

INTRODUCTION

1.1 Background and Objectives

The tilt-rotor concept combines the hovering advantages of the helicopter with the cruise advantages of a fixed-wing aircraft. Rotor/engine nacelles at the wing tips are rotated to the vertical position for hovering flight and to the horizontal position for cruising flight. The XV-15 research aircraft (Fig. 1.1) was jointly developed by the U.S. Army, NASA, and the Navy to demonstrate tilt-rotor technology. A key objective of this project was to achieve good piloted handling-qualities characteristics in hovering flight by using an advanced stability and control augmentation system (SCAS). This objective was emphasized because of serious handling-qualities deficiencies in hovering flight which were encountered with the original tilt-rotor demonstrator--the XV-3 (Ref. 1). Two XV-15 aircraft were developed under contract to Bell Helicopter Company and delivered to Ames Research Center (ARC) in 1980. One aircraft (N703) was retained at Ames for research and development testing; the other (N702) was leased back to the contractor for operational testing.

Comprehensive real-time and nonreal-time simulation codes (Refs. 2, 3) were developed to support the design and testing of the XV-15. Moving-base simulation facilities at ARC were extensively used for pilot training before the first flight tests, and subsequently for advanced automatic flight control system (AFCS) development. The XV-15 simulation code covers the entire operating envelope, with a full nonlinear

ORIGINAL PAGE IS
OF POOR QUALITY

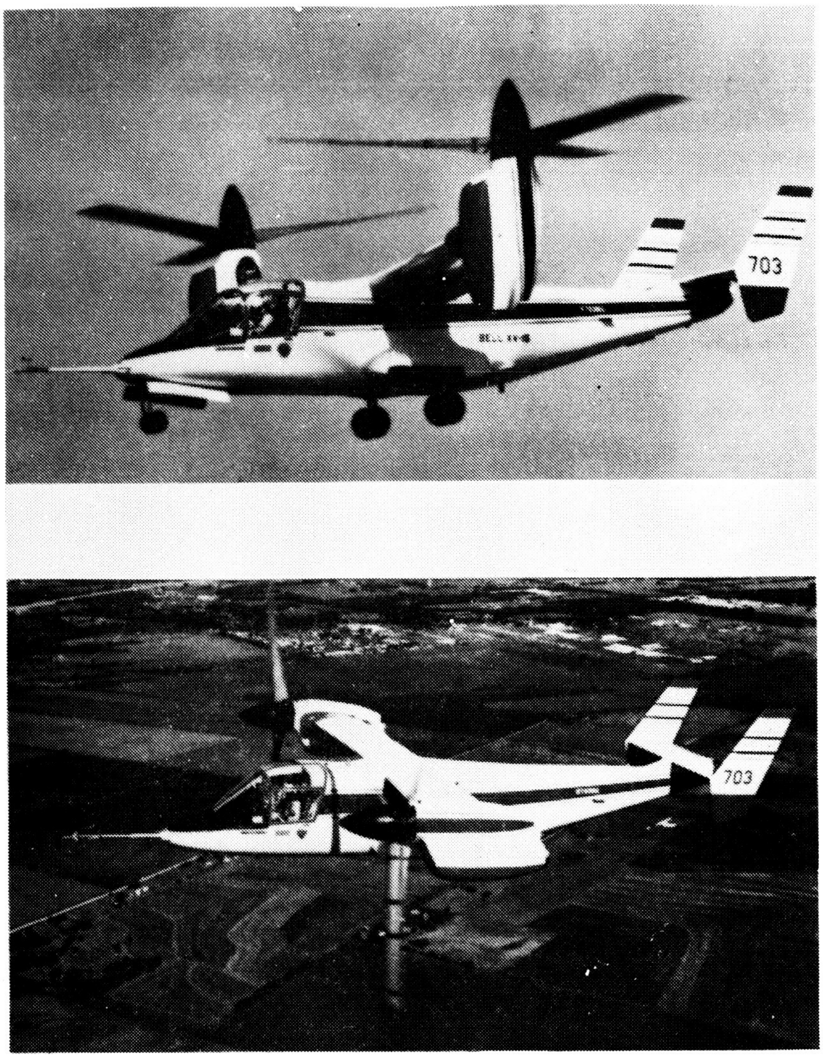

Fig. 1.1. The XV-15 Tilt-Rotor Aircraft. (a) Hover Configuration; (b) Cruise Configuration.

representation of the aircraft. Wing/body/tail aerodynamics are determined from extensive look-up tables of full-scale wind-tunnel data obtained in the NASA 40- by 80-Foot Wind Tunnel facility. Rotor calculations assume quasi-steady flapping and are based on modified Bailey equations with uniform rotor inflow. The aerodynamic interactions between the two rotors, and the rotor interference with the other aircraft elements are modeled in detail. Also modeled are numerous subsystem dynamics such as the engine drive train and governor. The XV-15 mathematical model was the most complex ever developed to that time for real-time piloted simulation at ARC (Ref. 4). The nonreal-time version is routinely used to support control-system development and flight-test planning. The XV-15 simulation mathematical models have been extensively correlated with static trim and performance flight data; the comparison is generally excellent (Ref. 5). However, dynamic checks have been very limited (Ref. 4), with most of the validation in this area centered on pilot subjective comparison of the aircraft and motion-based simulator response.

The author, as a staff member of an Army research team responsible for simulation technology, started in 1983 to conduct a comprehensive study to validate the open-loop dynamic response fidelity of the piloted-simulation mathematical model. An in-depth understanding of XV-15 dynamics and the availability of fully validated simulation models were considered important for the timely design and development of the Joint Services Operational Tilt-Rotor Aircraft--the JVX, now designated the V-22. To fulfill these needs, the study was initiated with the following three major objectives:

1. Document the open-loop dynamic characteristics of the XV-15 aircraft from flight tests for several operating conditions including hover

2. Compare aircraft and simulation response characteristics to identify problem areas in the mathematical modeling

3. Develop a validated transfer-function model description of the XV-15 needed for future studies

Emphasis was initially placed on the hover flight condition, where unstable open-loop dynamics lead to the most critical handling-qualities problems.

A key consideration in planning this study was the selection of an appropriate dynamics identification method.

1.2 Dynamics Identification Methods

Dynamics identification methods generally fall into two categories: frequency domain and time domain. Each approach has its inherent strengths and weaknesses which make it best suited for particular applications.

In time-domain (maximum-likelihood) identification (Fig. 1.2), the aircraft dynamics are modeled by a set of differential equations

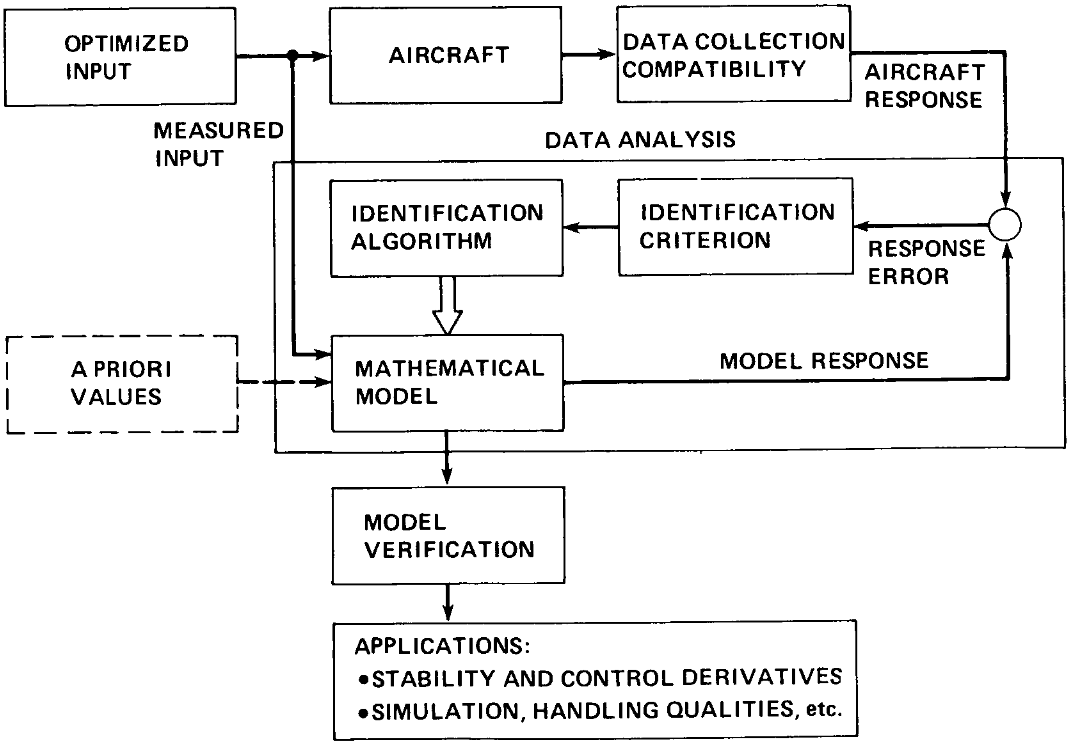
OPTIMIZED INPUT
AIRCRAFT
DATA COLLECTION COMPATIBILITY
AIRCRAFT RESPONSE
MEASURED INPUT
DATA ANALYSIS
IDENTIFICATION ALGORITHM
IDENTIFICATION CRITERION
RESPONSE ERROR
A PRIORI VALUES
MATHEMATICAL MODEL
MODEL RESPONSE
MODEL VERIFICATION
APPLICATIONS:
•STABILITY AND CONTROL DERIVATIVES
•SIMULATION, HANDLING QUALITIES, etc.

Fig. 1.2. Time-Domain Identification Method.

describing the external forces and moments in terms of state and control variables. The unknown coefficients in the equations are the stability derivatives, which are identified by least-squares fitting of the measured time-responses (output-error method). Such an approach allows a direct comparison of stability derivatives obtained in the wind tunnel and those of the actual flight vehicle. Transfer functions and frequency responses may be calculated from the state-space model. A key aspect of time-domain identification is that an a priori model formulation must be assumed. This important step involves consideration of model structure, order, and important nonlinearities. Such information is generally not well known on a new vehicle such as the XV-15, and incorrect model formulation can bias the parameter estimates (Ref. 6). Also, models which provide a good fit in the time-domain do not necessarily yield accurate transfer functions, since time-domain identification techniques weight their results more heavily at low frequency where most of the data points are concentrated.

The frequency-domain identification approach shown in Fig. 1.3 uses spectral analysis methods to extract the frequency responses between selected input and output pairs. The identification results are usually presented in Bode-plot format, that is, log-magnitude and phase of the input-to-output versus log-frequency. These identification results are nonparametric because no model structure is assumed. As such, they are useful for flight-control system design and pilot-in-the-loop handling-qualities studies. Frequency responses obtained from real-time and nonreal-time simulations can be compared directly with the flight data to expose limitations and discrepancies in the simulator models. The fact that this comparison can be made initally without an a priori

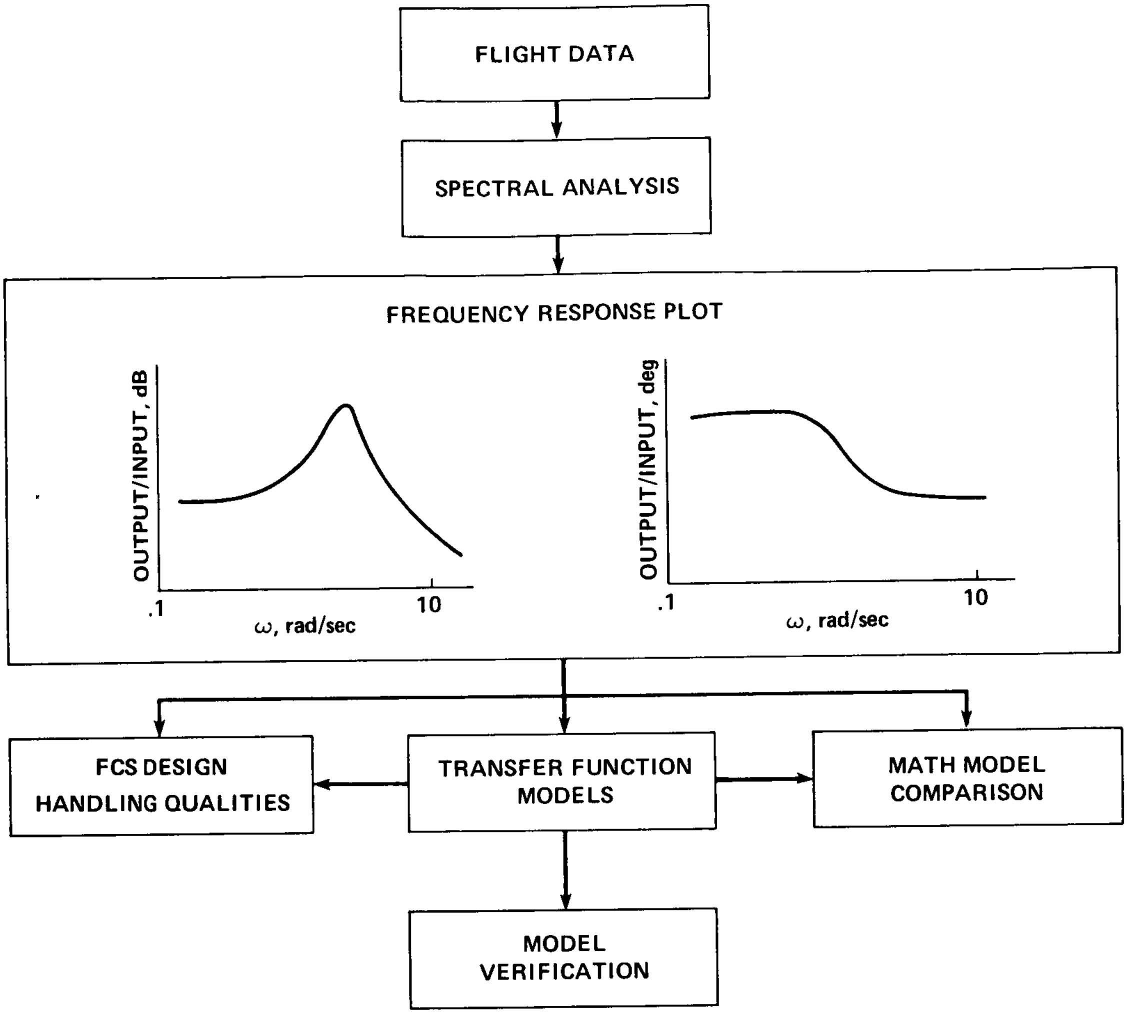
FLIGHT DATA
SPECTRAL ANALYSIS
FREQUENCY RESPONSE PLOT
OUTPUT/INPUT, dB
.1
10
ω, rad/sec
OUTPUT/INPUT, deg
.1
10
ω, rad/sec
FCS DESIGN
HANDLING QUALITIES
TRANSFER FUNCTION
MODELS
MATH MODEL
COMPARISON
MODEL
VERIFICATION

Fig. 1.3. Frequency-Response Identification Method.

assumption of model structure or order is especially important for verifying mathematical models of new aircraft configurations. When the model structure and parametric values are required, they may be obtained by fitting the frequency-responses with transfer-function models to extract modal characteristics. Examples of this application are the testing of handling-qualities specifications given in lower-order equivalent system terms, and the examination of transfer function-based control system designs. Since this fitting procedure is completed after the frequency response is extracted, the order of the transfer function can be selected to avoid an overparameterized model. Multi-input/multi-output (MIMO) frequency-response methods are suitable for extracting a transfer matrix which includes the important coupling effects. Finally, the extracted models are driven with the flight data to verify the time-domain characteristics. Models identified by frequency-domain techniques are often most accurate at mid- and high-frequency (initial time-history transients), which is the region of greatest concern to the pilot. The low-frequency and steady-state response prediction of the extracted models is generally not as good as in the time-domain identification approach.

Since the completion of the preceding objectives depends on obtaining an accurate characterization of the input-to-output transient dynamics and piloted handling-qualities of a new aircraft configuration, rather than on obtaining a stability derivative model (necessary for example to validate the wind-tunnel data base), the frequency-domain approach is the natural choice.

1.3 A Historical Summary of Research in Frequency-Response Identification

The earliest reported research in frequency-response identification of aircraft dynamics from flight-test data was conducted at the Cornell Aeronautical Laboratory beginning in 1945 (summarized in Ref. 7). Steady-state sine-wave inputs were used to (laboriously) extract the frequency responses of the North American B-25J (fixed-wing) aircraft. Then, lower-order transfer-function models were derived from a least-squares fit of the frequency-responses (displayed on a polar plot).

Fourier transform methods were subsequently developed (Refs. 7, 8) to allow frequency-response identification from (shorter-duration) discrete-maneuver data, such as that obtained from step and pulse inputs. These techniques were applied in flight research activities at the Air Force Flight Test Center (Edwards Air Force Base) during the 1950s (see Ref. 9 for a list of references). As pointed out in Ref. 9, all of these early efforts in frequency-response identification suffered from the lack of large-scale computing power. The development of the fast Fourier transform (FFT) algorithms in the 1960s, and the significantly improved computing capabilities of this period led to much greater interest and success in frequency-response identification.

A comprehensive facility for multivariable frequency-response (matrix) identification and analysis (FRA) based on the FFT was developed by Twisdale (1975) at the Edwards Test Center (complete documentation in Ref. 10). One key feature in this identification approach was incorporation of the ordinary, partial, and multiple coherence function calculations which provide an important measure of spectral estimation accuracy (Chap. 3). Identification was achieved from flight data of tracking and refueling handling-qualities tests instead of from data obtained with prescribed inputs.

Marchand and Koehler (Ref. 11), of the Institute for Flight Mechanics (DFVLR) in the Federal Republic of Germany, developed a method for extracting the stability-derivative matrix from identified frequency-responses; flight data were obtained with prescribed "multi-step" inputs--an outgrowth of research in optimal input design (see Ref. 6). Frequency-response identification from flight data obtained with the prescribed "frequency-sweep" input was pioneered by Systems Technology, Inc., (Refs. 12, 13). Advancements in lower-order transfer-function modeling were made by Hodgkinson et al. (Ref. 14), Bischoff and Palmer (Ref. 15), and Mitchell and Hoh (Ref. 16) in support of the development of an updated handling-qualities specification for military fixed-wing aircraft (Ref. 17).

The author was the first to extensively identify frequency-responses and transfer-functions of rotorcraft from flight tests using the frequency-sweep input (Ref. 18). The frequency-domain approach used in this study and depicted in Fig. 1.3 draws heavily on the preceding researchers' efforts. The frequency-response identification (FRESPID) program developed for this effort (Chap. 3) was patterned after the FRA facility (Ref. 10). A major advancement in the FRESPID program is the incorporation of the chirp z-transform, an algorithm for obtaining frequency-responses which are of much higher quality than those obtainable from standard FFT procedures. Also, the author has stressed the importance of deriving physically consistent transfer-function models and verifying those models with time-domain data not used in the identification procedure.

1.4 Scope of Research

This study involved the planning and execution of flight tests on the XV-15 aircraft and piloted-simulation for four flight conditions from hover to cruise. Improved test techniques and associated pilot training procedures were devised. Analytical software tools were developed (or adapted) which allow the identification of high-resolution spectral responses and the derivation and validation of MIMO transfer-function models. These techniques were applied in an extensive evaluation of the open-loop flight dynamics of the XV-15 and simulation mathematical models. Mathematical model deficiencies were clearly exposed and documented. Finally, a new, fully validated transfer-function model was derived for the hover and cruise flight conditions.

1.5 Extensions and Applications

As in most research efforts, the scope of this project grew well beyond the original objectives outlined in Sec. 1.1. The advantages of the frequency-domain approach for documenting the response characteristics of new configurations became readily apparent in the XV-15 study and led to the use of this technique in a variety of related helicopter flight test projects.

Frequency-domain testing of the Bell 214-ST single-rotor helicopter was completed by the author in October 1985 to support the Army's development of an updated handling-qualities specification (Ref. 19). A discussion of the testing procedures and identification results for the Bell 214-ST is presented in Ref. 20. This project demonstrated the feasibility of frequency-sweep testing and frequency-domain identification as a specification-compliance documentation tool. Further, the results showed that very low order transfer-function models can accurately predict the large motion time-domain behavior of single-rotor helicopters--even in hover.

The frequency-domain identification method was also used to document the dynamic characteristics of the CH-47B research aircraft (Refs. 6, 21). Current research by the author and Kaletka (Ref. 22) under a memorandum-of-understanding between the United States and the Federal Republic of Germany is concerned with comparing frequency and time-domain identification results for the open-loop XV-15 dynamics in hover. Research by the author and Acree (Ref. 23) concerns identification of XV-15 structural dynamics using the frequency-domain approach.

1.6 Organization of Dissertation

The central focus of this dissertation is the documentation and analysis of the dynamics of a unique vehicle--the XV-15. Chapter 2 describes the general vehicle configuration and important subsystems, and reviews the flight test conditions. The frequency-domain method, briefly overviewed in the present chapter, is discussed in detail in Chapter 3. Chapters 4 and 5 present the dynamics identification results for the hover and cruise flight conditions. Frequency responses and transfer-function models extracted from flight tests are compared with real-time and nonreal-time simulation results. Time-history verification responses show the ability of the extracted lower-order transfer-function models to accurately predict large-amplitude response characteristics of the XV-15 in hover and cruise. Chapter 6 reviews the key conclusions and contributions of this work. Recommendations for future research in frequency-response identification are discussed in Chapter 7. Appendix A reviews the important advantages of the chirp z-transform, as compared to the standard fast Fourier transform, for frequency-response identification from flight data. Appendix B discusses the limitations in identifying open-loop vehicle dynamics from closed-loop flight tests. An appreciation for these limitations is important in applying the present identification method to future flight tests. The text of this dissertation draws heavily on the author's publications concerning the tilt-rotor study (Refs. 18, 22, 24) and related research efforts (Refs. 6, 20).

Chapter 2

XV-15 RESEARCH AIRCRAFT AND FLIGHT TEST CONDITIONS

An understanding of XV-15 aircraft dynamics requires an appreciation of this unique vehicle's configuration and key subsystems. This Chapter first reviews the vehicle layout, operational flight envelope, cockpit controls, automatic flight-control system, and research instrumentation, and then outlines the flight-test conditions and test inputs for this study.

2.1 Aircraft Description

2.1.1 General Layout

The XV-15 aircraft is a lateral-tandem rotor vehicle. The rotors are 25 ft in diameter and the spinner-to-spinner span is 32 ft (Fig. 2.1). The aircraft is powered by two Lycoming T-53 turboshaft engines (1250 SHP each), one mounted in each wing-tip nacelle. These nacelles rotate from $i_N = 0$ deg (cruise configuration) to $i_N = 90$ deg (hover configuration). Rearward flight acceleration is enhanced by rotating the nacelles to $i_N = 95$ deg.

The rotor system is a three-bladed prop-rotor with a stiff in-plane gimbal mounting to the hub. Rotor tip-path-plane orientation is controlled through standard cyclic and collective feathering of the individual blades. The resultant hub moments cause the entire rotor system to rotate (flap) as a unit, rather than each blade independently as in articulated helicopters. Cross-shafting between the nacelles synchronizes the rotors and provides a one-engine-out capability. An engine

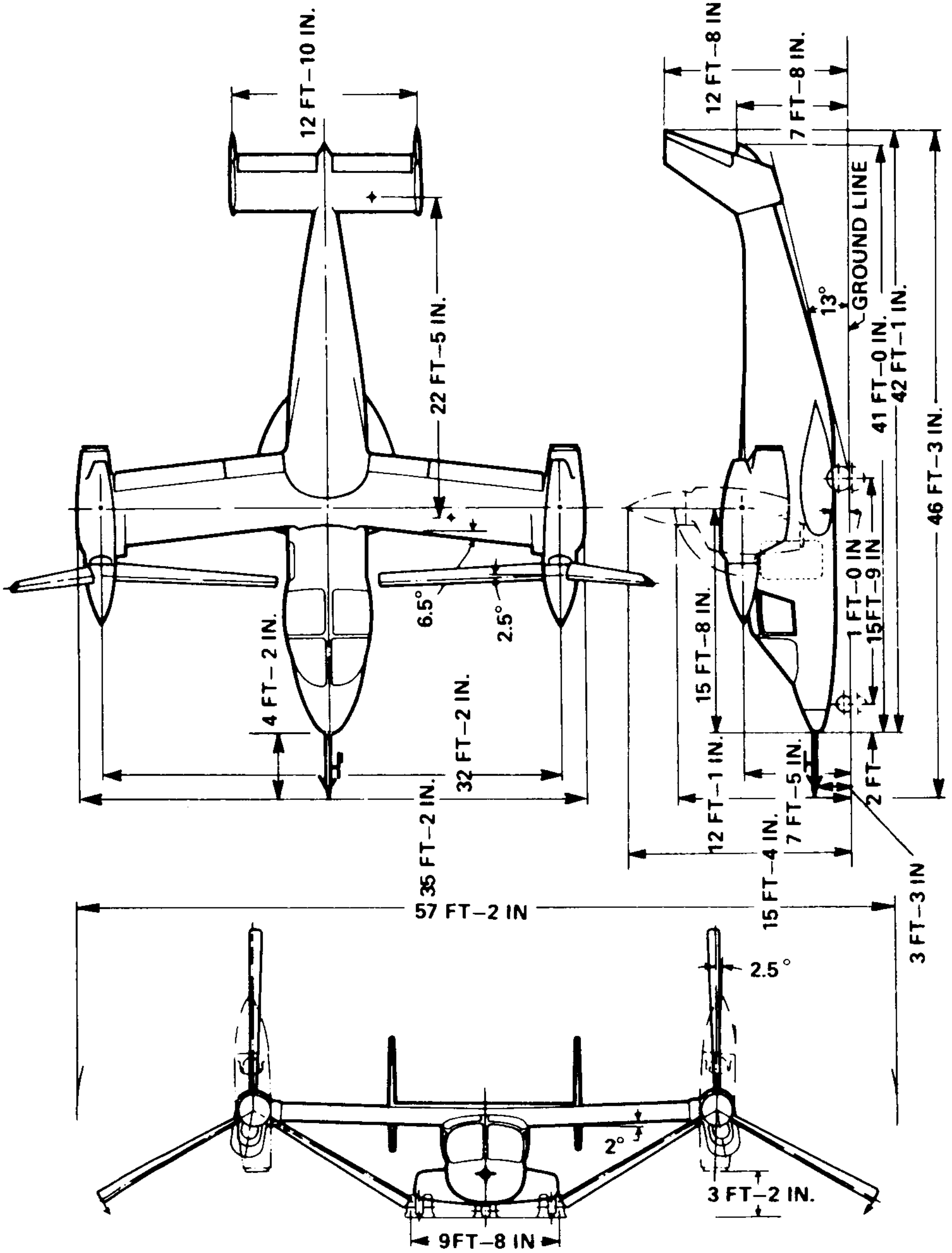
12 FT–10 IN.
22 FT–5 IN.
6.5°
2.5°
4 FT– 2 IN.
32 FT–2 IN.
35 FT–2 IN.
57 FT–2 IN
12 FT–8 IN.
7 FT–8 IN.
GROUND LINE
13°
41 FT–0 IN.
42 FT–1 IN.
46 FT–3 IN.
1 FT–0 IN.
15FT–9 IN
15 FT–8 IN.
12 FT–1 IN.
7 FT–5 IN.
2 FT
7 FT–4 IN.
15 FT–4 IN.
3 FT–3 IN
2.5°
2°
3 FT–2 IN.
9FT–8 IN

Fig. 2.1. Three-View Layout of XV-15 Tilt-Rotor Research Aircraft.

governor system adjusts the pilot's power lever commands to the collective pitch of the blades to maintain constant rotor rpm.

2.1.2 Operating Flight Envelope

The operational envelope shown in Fig. 2.2 is from slow rearward flight to a maximum true airspeed of V_t = 300 knots (with the nacelles locked at i_N = 0 deg). When the nacelles are not in their locked position, the maximum airspeed is restricted to V_t = 170 knots because of aeroelastic stability limitations. The "conversion corridor" of Fig. 2.3 defines the allowable range of nacelle-angle/airspeed

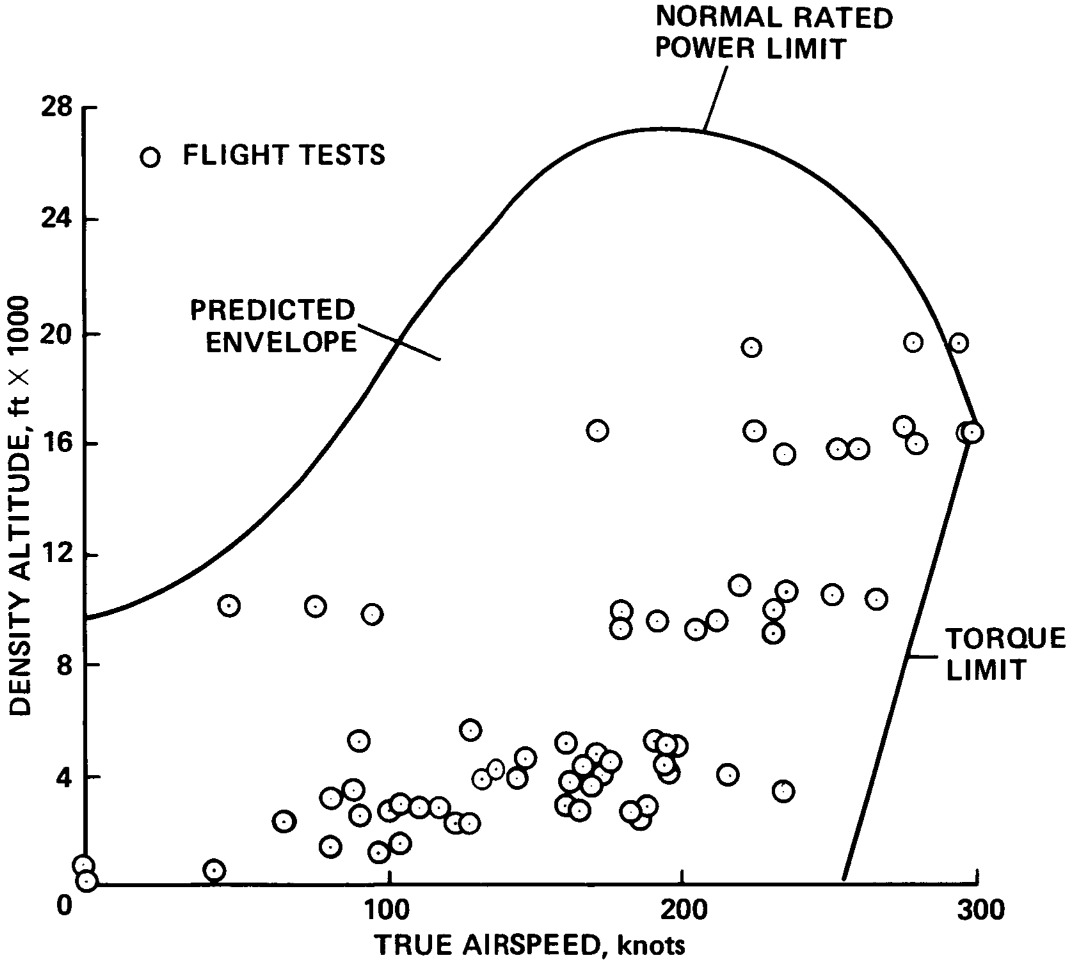

Fig. 2.2. Airspeed-Altitude Envelope.

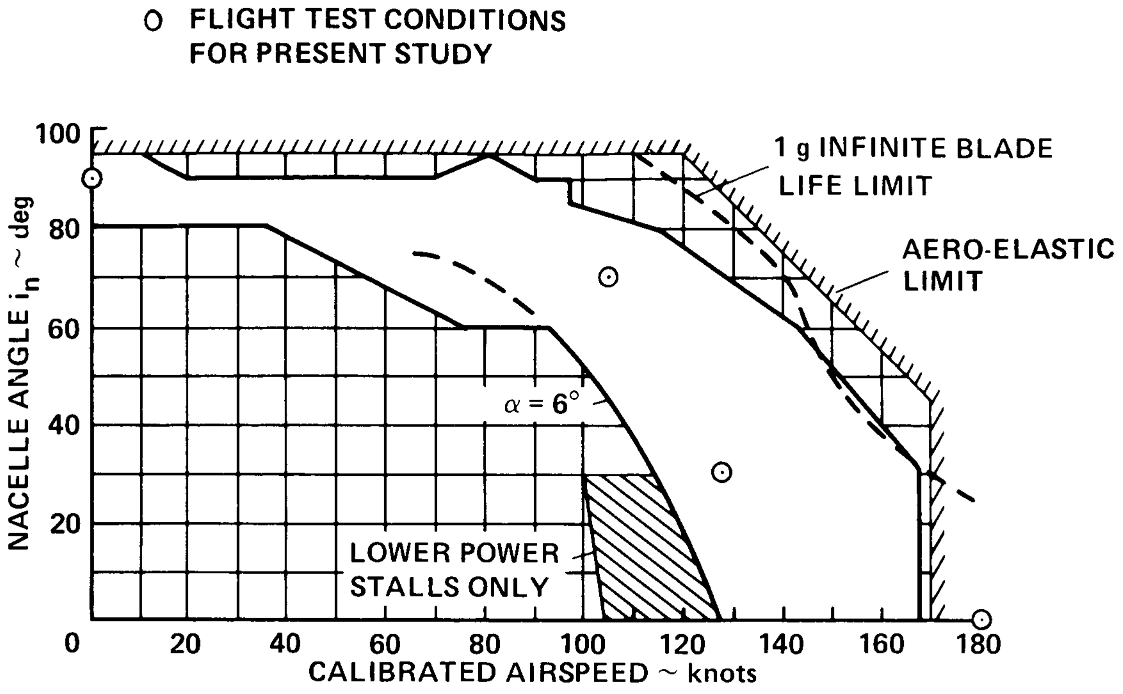

Fig. 2.3. Conversion Corridor.

combinations in the transition flight regime between hover and cruise. The lower boundary on nacelle angle is determined by wing-loading limits, and the upper boundary is determined by blade loading limits. The nominal weight of the XV-15 is 13,000 lb and the flight endurance is approximately 1 hr.

2.1.3 Vehicle Control

The pilot's cockpit controls in the XV-15 are the same as those found in conventional helicopters. A center stick is used to control the pitch and roll motions. Pedals are used to control yaw motions, and a power lever is used to control vertical motion in hover and airspeed in forward flight. The means with which these cockpit controls generate the required forces and moments depends on the aircraft configuration.

The control method for helicopter-mode flight is shown in Fig. 2.4. Rolling moments are generated with differential collective, pitching moments with uniform longitudinal cyclic (fore-aft tip-path-plane rotation), yawing moments with differential longitudinal cyclic, and heave forces with uniform collective. In cruising flight, the rotor controls are phased out and control moments are generated with standard aircraft aerodynamic surfaces; the ailerons produce rolling moments, the elevator produces pitching moments, and the rudder produces yawing moments.

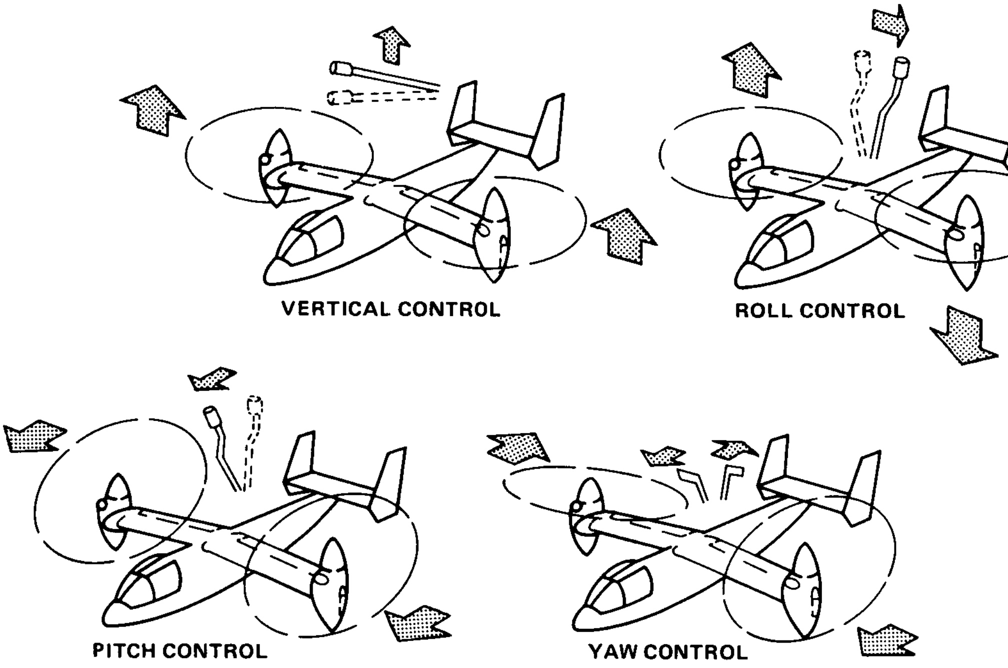

Fig. 2.4. Control Method for Helicopter-Mode Flight.

Speed control is achieved through the throttle/governor system. The rotor control (swashplate) and aerodynamic surfaces receive commands from the cockpit via mechanical linkages and hydraulic actuators. These commands are augmented by signals from the automatic flight-control system through series actuators.

The phase-out of the rotor controls from hover to cruise is automatically scheduled as a function of nacelle angle i_N. The aerodynamic surfaces are actuated throughout the entire flight envelope, although they have no effect at very low airspeeds. It is most expedient to refer all of the open-loop vehicle response characteristics (e.g., frequency responses, transfer functions, etc.) to these surface deflections since, neglecting the small servo lags, these are related to the sum of the pilot and SCAS inputs (total input to the aircraft) through a mixing ratio which is constant across the entire flight envelope.

In the helicopter configuration, the XV-15 open-loop dynamics are typical of hovering vehicles, although the number of cross-coupling paths is much lower than in single-rotor helicopters. The planar symmetric, lateral-tandem configuration yields vehicle dynamics which are essentially decoupled between the longitudinal and lateral/directional degrees-of-freedom. One-way coupling from roll input to yaw response is significant. This is due to the differential rotor torque which accompanies the differential collective inputs for roll control. The open-loop pitch and roll dynamics in hover are characterized by highly unstable low-frequency attitude-speed divergences. The heave and yaw dynamics are decoupled from the attitude motions and are essentially first-order. The time-constants of these dynamics are very long ($\doteq$ 10 sec) because the tilt-rotor configuration has a relatively high disk-loading (low heave damping) and no tail-rotor (low yaw damping).

Limited evaluations of the SCAS-off handling-qualities in hover have been conducted (Ref. 25). These evaluations indicate that the severe attitude instability and small translational damping result in very poor handling-qualities. Precision hover tasks (out of ground-effect) were rated with Level II handling-qualities ("adequate performance achieved with high level of pilot workload"). Precision translation tasks were rated with Level III handling-qualities ("unsatisfactory performance"). Quantitative documentation of the open-loop XV-15 dynamics in hover is critical to "convert" these pilot-opinion ratings into engineering requirements for future tilt-rotor configurations.

2.1.4 Automatic Flight Control System

A nominal stability and control augmentation system (SCAS) was incorporated in the XV-15 to enhance the poor bare-airframe dynamic characteristics. Improved closed-loop handling qualities were achieved with an advanced SCAS developed by Churchill and Gerdes (Ref. 25) between 1982 and 1984. This advanced system combines feed-forward shaping, model-following, and disturbance rejection to achieve crisp first-order responses in the attitude rates and improved inherent stability. The closed-loop response time constants are about 0.4 sec in pitch and roll and about 0.6 sec in yaw. An attitude-retention system based on attitude-angle feedback provides hands-off stability when the controls are in their neutral position. In forward flight, the control system provides constant load factor responses to longitudinal stick inputs and coordinated turn responses to lateral stick inputs. These improved characteristics give the aircraft Level I handling qualities ("performance satisfactory without improvement") for the precision piloting tasks (Ref. 25).

The SCAS is a two-channel (summed) fail/operate system. Thus, failure of either channel results in reversion to a single (lower-gain) channel. Failure of the second channel reverts the aircraft back to the SCAS-off configuration. The SCAS authority is limited to 20% of maximum stick deflection in the pitch axis, and 30% of the maximum control in roll and yaw.

2.1.5 Research Instrumentation

The XV-15 is heavily instrumented to provide real-time and post-flight engineering data. Measurements of over 150 variables including angular rates, attitudes, accelerations, surface deflections, cockpit controls, and structural loads are recorded on board at 250 Hz on pulse-code-modulation (PCM) tapes. Besides this on-board recorder, a telemetry (TM) link provides safety-related data which are monitored by a six-member flight-test ground crew. This extensive instrumentation system is carefully maintained and regularly calibrated. After the flight tests, the PCM tapes are digitized, and the data are converted to engineering units.

The three-axis gyroscope package has a bandwidth of about 20 Hz, which is well beyond the frequency range of interest for rigid-body dynamics identification. Analog measurements of controls and responses are conditioned with 50 Hz analog pre-filters to reduce digital aliasing, while maintaining a broad band of accurate dynamic measurements. Matching the filters on the input and output signals minimizes the phase distortions in the identified frequency responses.

2.2 Flight Test Conditions

The following four flight test conditions were selected to span the full operating range of the XV-15 aircraft:

1. Hover: Ambient wind less than 5 knots, $i_N = 90$ deg, gear down, out-of-ground effect (altitude = 100 ft)

2. Low-speed transition: Indicated airspeed $V_i = 100$ knots (calibrated airspeed, $V_c = 105$ knots), $i_N = 70$ deg

3. High-speed transition: Indicated airspeed $V_i = 120$ knots (calibrated airspeed, $V_c = 128$ knots), $i_N = 30$ deg

4. Cruise: Indicated airspeed $V_i = 170$ knots (calibrated airspeed, $V_c = 180$ knots), $i_N = 0$ deg

These flight conditions are noted on the conversion corridor of Fig. 2.3.

Dynamics identification tests were conducted from February through December 1983, in about 12 flight hours. During the same period, frequency-sweep tests were conducted in the Vertical Motion Simulator (VMS) to document the real-time XV-15 mathematical model. Subsequent analyses of aircraft and simulation flight dynamics concentrated on the hover and $V_i = 170$ knots cruise conditions.

Frequency-sweep (Sec. 3.1.2) and step inputs were executed in each axis for all four flight conditions. In hover, three frequency-sweeps were conducted to ensure that sufficient dynamic data were obtained for good identification of this most important and (difficult to analyze) condition. In the remaining flight conditions, where the vehicle is much more stable, only two frequency-sweeps were required.

The high degree of open-loop pitch and roll instability in the hover flight condition dictated that longitudinal and lateral stick frequency-sweeps in this flight condition be conducted with all SCAS channels ENGAGED. Pedal-sweeps were conducted with the yaw-SCAS disengaged, because yaw-SCAS failures occurred in mid-run resulting from the relatively large angular rates which were generated. The decoupled and stable nature of the yaw (and heave) dynamics allowed SCAS-off sweeps to be conducted in these axes without difficulty. Step inputs were executed in the SCAS-on and SCAS-off configurations. SCAS-off step responses were completed to verify that the extracted transfer-functions reflect the open-loop response characteristics and not those of the inverse feedback dynamics (Chap. 3). These inputs were completed with the off-axis channels engaged (e.g., open-loop pitch-axis inputs were conducted with roll and yaw channels engaged), to reduce the level of coupled, unstable dynamic response. SCAS-on step responses were also completed because the SCAS helps to steady the initial conditions, which is helpful in exposing small differences between the model and aircraft dynamics.

In the transition and cruise flight conditions, the longitudinal frequency-sweeps were conducted with pitch SCAS engaged. Frequency-sweeps in the lateral and directional axes were completed with the roll and yaw SCAS channels disengaged because initial SCAS-on results exhibited unacceptable levels of aileron/rudder correlation (Chap. 3). Step inputs in all axes were completed for both SCAS-on and SCAS-off configurations as in hover.

The next chapter discusses the dynamics-identification method in detail.

Chapter 3

FREQUENCY-DOMAIN IDENTIFICATION METHOD

The frequency-domain method of Fig. 1.3 was briefly outlined in Chapter 1. In this Chapter, the individual analysis steps of the approach are discussed in detail.

3.1 Flight Test Technique

3.1.1 General Requirements

The principal ingredient for success in any identification scheme is the selection of an input signal that excites the vehicle in all of its dominant modes of motion in the frequency range of interest. In piloted handling-qualities studies, the important frequency range is approximately 0.2-6.0 rad/sec (Refs. 17, 19). To achieve good frequency-domain identification in this range, the magnitude of the input autospectrum should be nearly constant. From a piloting standpoint, the selected inputs should be easily repeatable and not involve drastic maneuvers or significant changes in the equilibrium flight condition. One input which fulfills the preceding requirements and which has been used successfully in a number of rotorcraft flight tests (Refs. 6, 18, 20, 21, 26) and non-rotorcraft flight tests (Refs. 12, 13, 27) is the "frequency-sweep."

3.1.2 Frequency Sweep

A typical lateral-stick (δ_{LAT}) frequency-sweep completed during the XV-15 hover tests and developed by the author is shown in Fig. 3.1. Pilot-generated inputs were used instead of computer-generated inputs. The sweep is initiated with two low-frequency sinusoid-shaped cycles,

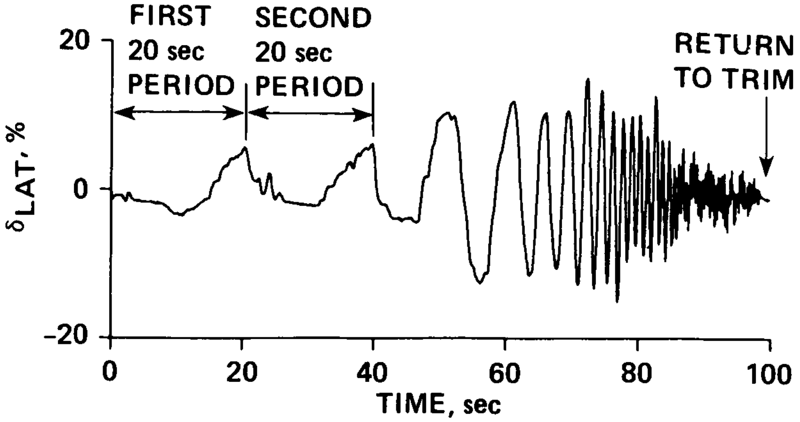

Fig. 3.1. Typical Lateral-Stick Frequency Sweep (δ_{LAT}).

with periods corresponding to the lower bound of the desired identification frequency range. These cycles ensure good excitation of the low-frequency dynamics. The desired lower bound of ω_{min} = 0.2 rad/sec gives a low-frequency period of about T_{max} = 30 sec. However, attempts to execute this low-frequency input in flight resulted in undesirably large vehicle motions. Therefore, it was necessary to reduce the period of the low-frequency cycle to T_{max} = 20 sec (Fig. 3.1). The magnitude of the control input is adjusted to keep roll and pitch attitudes, as well as resulting translations, comfortable and reasonably close to their trim values. The lower pitch and roll damping in hovering flight demands smaller pilot inputs than those which are used in transition and forward flight.

After the initial two low-frequency cycles, the control is moved at gradually increasing frequency for another 50 sec. This increasing-frequency (as opposed to a decreasing-frequency) input allows the transients of the low-frequency modes to persist for a few more cycles during the remainder of the run, thus improving the low-frequency identification; the high-frequency modes need less excitation time to persist the same number of cycles, so they are excited toward the end of the input. By the end of the run, the control is being driven quite rapidly (about 4 Hz in Fig. 3.1) with generally smaller displacements. The control is then returned to trim, ending the approximately 90-sec test period. The selection of the (rather long) overall 90-sec test period was found (empirically) to

1. Allow a good identification of the low-frequency modes
2. Result in an even pilot-excitation of the vehicle dynamics over the identification frequency range
3. Yield a large quantity of data, thereby reducing the variance of the spectral estimate (see Sec. 3.2.3)

At least two sweeps are performed consecutively for each control to ensure a sufficient amount of good quality dynamic data for the spectral analysis. Frequency-sweeps are conducted individually on each of the four primary aircraft controls (lateral and longitudinal stick, pedals, and power lever) for one flight condition, before other conditions are investigated.

3.2 Frequency-Response Identification

The most important step in the frequency-domain identification method is the accurate estimation of input-to-output spectral responses, since all succeeding calculations are based on these results. Considerable effort was invested at the beginning of this study in evaluating and implementing various spectral-analysis methods. Numerical studies based on reconstructing frequency responses from simulated time-histories of known transfer functions were useful in evaluating the various computational methods. However, methods which proved successful with simulated data did not always give satisfactory results when applied to flight data. Good quality results at low frequency initially proved very difficult to obtain. This was due to the poor spectral content which generally occurs at low frequency because of the lower pilot input amplitudes (see Fig. 3.1). Considerable improvements were achieved with more advanced analysis methods developed as a result of identification efforts on the XV-15, CH-47, and Bell 214-ST aircraft (Refs. 6, 18, 20-24). These methods draw heavily on the signal processing literature (Refs. 28-32).

Figure 3.2 shows the computational procedures which are performed by the FRESPID program to generate the spectral responses of selected input and output time-histories. This program was jointly developed by the author and J. G. M. Leung.[†] The FRESPID program operates in a batch processing mode, under the control of a command file. As illustrated in Fig. 3.3, this file contains command directives and flight-data record identifiers which specify the desired input/output records and data processing options. The next two sections describe in more detail the computations which are performed by the FRESPID program.

3.2.1 Data Preparation

As indicated in the flowchart of Fig. 3.2, a large part of the analysis involves data preparation before applying the Fourier transform algorithm. These preparation steps are crucial to obtaining an accurate frequency-response estimate.

[†] Electronics Engineer; Flight Experiments Support Branch, NASA Ames Research Center, Moffett Field, Calif.

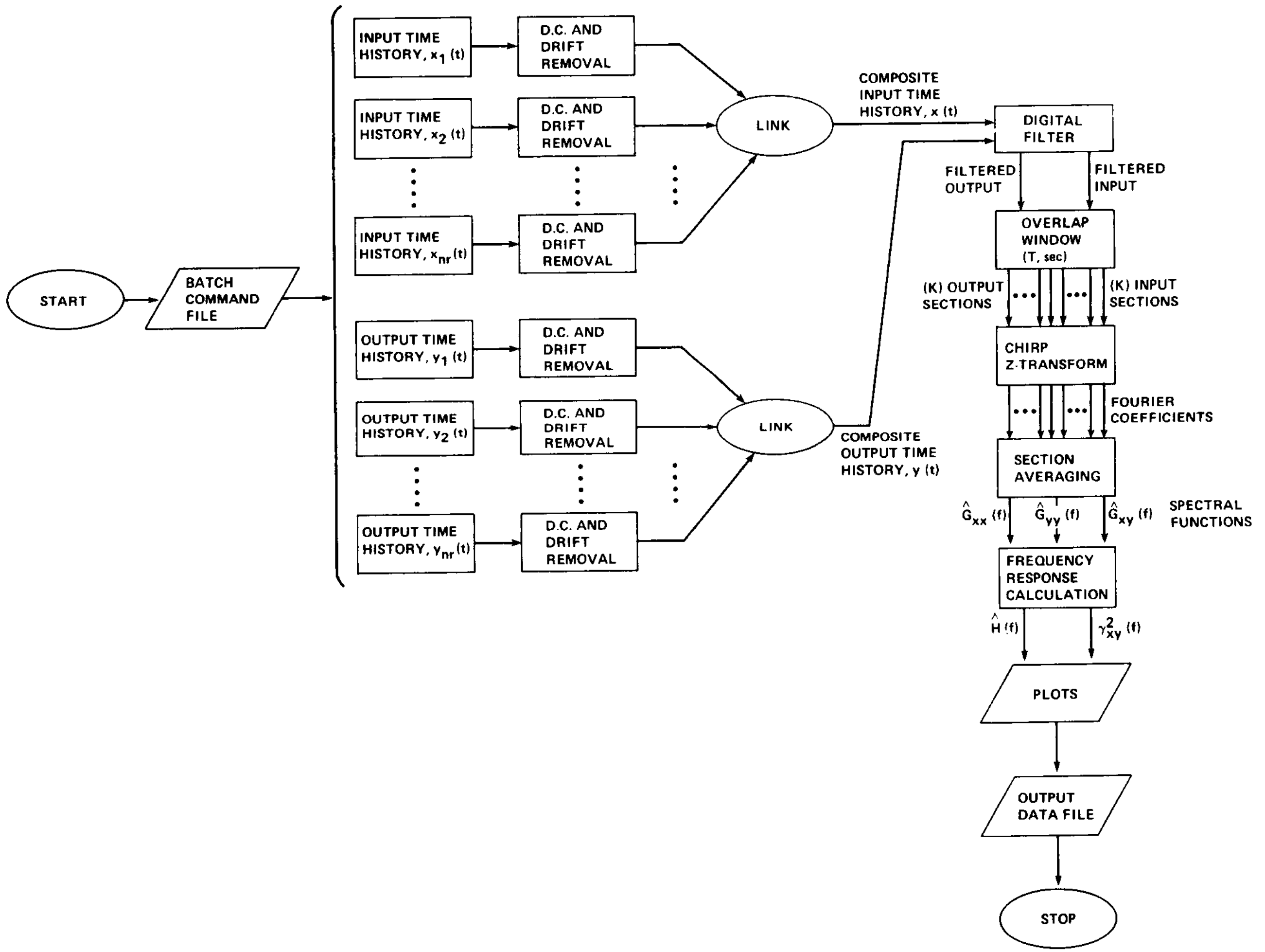
START
BATCH COMMAND FILE
INPUT TIME HISTORY, x_1 (t)
INPUT TIME HISTORY, x_2 (t)
INPUT TIME HISTORY, x_{nr} (t)
OUTPUT TIME HISTORY, y_1 (t)
OUTPUT TIME HISTORY, y_2 (t)
OUTPUT TIME HISTORY, y_{nr} (t)
D.C. AND DRIFT REMOVAL
LINK
COMPOSITE INPUT TIME HISTORY, x (t)
COMPOSITE OUTPUT TIME HISTORY, y (t)
DIGITAL FILTER
FILTERED OUTPUT
FILTERED INPUT
OVERLAP WINDOW (T, sec)
(K) OUTPUT SECTIONS
(K) INPUT SECTIONS
CHIRP Z-TRANSFORM
FOURIER COEFFICIENTS
SECTION AVERAGING
$\hat{G}_{xx}$ (f)
$\hat{G}_{yy}$ (f)
$\hat{G}_{xy}$ (f)
SPECTRAL FUNCTIONS
FREQUENCY RESPONSE CALCULATION
$\hat{H}$ (f)
γ^2_{xy} (f)
PLOTS
OUTPUT DATA FILE
STOP

Fig. 3.2. Flowchart of Computational Procedures Performed by the FRESPID Program.

Command file directives	Remarks
V=0. P/DAIL 883,884 60S WINDOW [OC128]	command file identifier
WINDOW	key word: window specification
MYDISK:[TISCHLER.TILTBFILE]XV15W60S	window specification file
LINK	key word: file concatenation
D645R883.150 V012R883.150	input file-1 output file-1
D645R884.150 V012R884.150	input file-2 output file-2
FILTER	key word: digital filtering
MYDISK:[TISCHLER.BFILE]AALIAS.62H	impulse response file
0.1, 10.0	Chirp z-transform freq. range
OC128	output file name
STOP	program terminator

Fig. 3.3. Sample Command File for FRESPID.

The dc (offset) components and linear drifts (trends) of the selected input and output time-histories are first removed to prevent oscillation in the spectral calculations. Since the frequency-sweep begins and ends in trim and is a roughly symmetric excitation (Fig. 3.1), the dc and drift are simply determined from the mean offset and slope of the time-history trace (Ref. 28). When (nr) multiple runs of good spectral quality are available, they are concatenated to form composite input and output time-histories. The concatenated time-histories are then digitally filtered to eliminate the jitter (digital noise) which arises from asynchronous sampling of the instruments ("sample-skewing"), and can cause distortion in the spectral estimate. The filter cutoff frequency is 62.5 Hz, which is 50% of the Nyquist frequency. Finite-impulse-response (FIR) filters are used [instead of recursive infinite-impulse-response (IIR) filters] because they have magnitude characteristics that can be easily tailored, and they exhibit a linear phase shift with frequency (independent of the magnitude response) (Ref. 28). The additional computational time for the FIR filters compared to that of IIR filters is not a concern for off-line analyses.

The filtered concatenated records are partitioned into (K) tapered and overlapping subrecords of (L) discrete data points. These subrecords, or time-history sections, are often referred to as "windows," because the data contained therein are the only part of the time-history that the fast Fourier transform (FFT, Sec. 3.2.2) can "see" at one time. Applying a cosine-squared tapering (weighting) function (also referred to as "Hanning window") prevents side lobes and leakage which would otherwise occur with a rectangular (nontapered) window. Overlapping the windows makes more efficient use of the data at the edges of the tapered window, thereby reducing the spectral bias and variance compared with the non-overlapped tapered estimate (Ref. 28).

The width of the window ($L\Delta t$, sec; Δt is the time increment) is an important parameter in determining the quality of the spectral identification. The windows are optimized for each run (and flight condition) to achieve maximum spectral accuracy over the desired frequency range. As discussed in Sec. 3.2.3, the random error is inversely proportional to the square root of the number of (independent) time-history sections--which is the effect of averaging. So for a given total run time, smaller windows yield more averaging and lower spectral variance. However, this reduction in window length also reduces the low-frequency content in each window and, accordingly, in the overall identification. Thus, the selection of window length involves a compromise between a high number of averages and adequate low-frequency signal content. By concatenating good repeat runs into a single time-history, longer windows can be selected without compromising the number of averages. This yields wide-band identification and low spectral variance. When only one suitable run is available, shorter windows are necessary to maintain a sufficient number of averages, and the low-frequency identification is compromised. A window length which contains roughly two periods of the lowest-frequency wave of interest ($L\Delta t = 2T_{max} = 40$ sec) is generally a good compromise.

3.2.2 Spectral Functions[†]

The finite Fourier transform $X(f,T)$ of a (finite length, T) continuous time-history subrecord $x(t)$ (e.g., one window of time-history data) is:

$$X(f,T) = \int_0^T x(t)e^{-j2\pi ft}\,dt \tag{3.1}$$

When the time-history data are from a discrete sequence x_n, the Fourier transform integral relation is approximated by the discrete Fourier transform (DFT):

$$X(f_k) = X(k\Delta f) = \Delta t \sum_{n=0}^{N-1} x_n \exp[-j2\pi(kn)/N] \ ; \quad k = 0,\ 1,\ 2, \ldots,\ N-1 \tag{3.2}$$

where

$X(f_k)$ = Fourier coefficients

$x_n = x(n\Delta t)$

Δt = time increment

N = number of discrete frequency points

[†] Background information on spectral analyses and the chirp z-transform is given in Appendix A.

For the DFT,

$$N = L = \text{number of time-history points in the sequence, } x_n \qquad (3.3)$$

so,

$$T = L\Delta t = \text{time duration of sequence (i.e., "width of window")}$$

$$(3.4)$$

$$\Delta f = \frac{1}{T} = \frac{1}{L\Delta t} = \text{frequency resolution, Hz}$$

The evaluation of Eq. (3.2) requires approximately N^2 multiply-add operations for each window of data.

The fast Fourier transform (FFT) refers to efficient algorithms (there are many, Ref. 28) for determining the DFT of Eq. (3.2). The FFT procedures require approximately $4N \log_2 N$ computations, which gives a speed ratio of (Ref. 28):

$$\text{speed ratio} = \frac{N^2}{4N \log_2 N} \doteq 160 \text{ for the present analysis}$$

indicating a considerable computational savings. One particularly flexible FFT algorithm is the chirp z-transform (also referred to as the "zoom transform" or CZT). This algorithm (Refs. 30, 32) allows the rather severe restriction of Eqs. (3.3) and (3.4) to be relaxed, which yields much finer frequency resolution (Δf) for a given window size ($L\Delta t$). Another key advantage of the chirp z-transform is that the number of time-history points L can be arbitrary, whereas L must be a composite integer (an integer power of 2) in standard FFT procedures. These capabilities of the chirp z-transform allow the extraction of high-resolution spectra in a narrow frequency band, and an increase in the identified dynamic range, especially at the low-frequency end (Ref. 32). The chirp z-transform has been found in this and in a number of other studies by the author to be well suited for frequency-response identification from flight data (Refs. 6, 20, 21, 23).

The one-sided input autospectral-density estimate for the subrecord x_n is determined from the chirp z-transform (Fourier) coefficients:

$$\tilde{G}_{xx}(f_k) = \frac{2}{TU} |X(f_k)|^2 , \qquad k = 0, 1, \ldots, N/2 \tag{3.5}$$

where U is the scale factor for window tapering [$U = (8/3)^{1/2}$ for Hanning window, Ref. 28].

The one-sided output autospectral-density estimate is similarly obtained from the output subrecord by replacing y (output record) for x in Eqs. (3.1)-(3.5):

$$\tilde{G}_{yy}(f_k) = \frac{2}{TU} |Y(f_k)|^2 , \qquad k = 0, 1, \ldots, N/2 \tag{3.6}$$

The one-sided cross-spectral density estimate is determined by[†]:

$$\tilde{G}_{xy}(f_k) = \frac{2}{TU} [X^*(f_k)Y(f_k)] , \qquad k = 0, 1, \ldots, N/2 \tag{3.7}$$

[†] Asterisk (*) denotes complex-conjugate.

Finally, the total spectral-function estimates for the entire (concatenated) time-history is obtained from a linear average of the spectra for the (K) overlapped subrecords:

$\hat{G}_{xx}(f_k)$ = averaged input autospectral-density estimate

$\hat{G}_{yy}(f_k)$ = averaged output autospectral-density estimate

$\hat{G}_{xy}(f_k)$ = averaged cross-spectral density estimate

These quantities are physically interpreted as giving the distribution of the mean-squared response of the respective signals (i.e., xx, yy, xy) as a function of frequency. For illustrative purposes, the spectral-density magnitudes are presented in power-dB ($= 10 \log_{10}|G_{xx}(f_k)|$, etc.) which gives the distribution of the root-mean-squared (rms) response. These results are the bases for the frequency-response calculations in the next section.

3.2.3 Single-Input/Single-Output Frequency-Response Calculations in the Open-Loop

Once the input, output, and cross-spectral density estimates [($\hat{G}_{xx}(f_k)$, $\hat{G}_{yy}(f_k)$, $\hat{G}_{xy}(f_k)$, respectively] have been determined for a selected time-history pair (x, y in Fig. 3.4) the single-input/single-output frequency response is estimated by

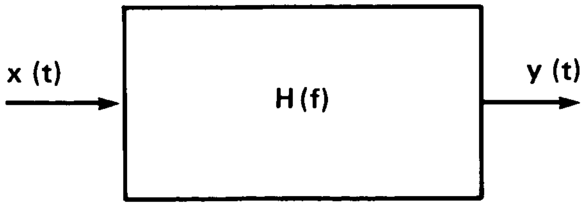

Fig. 3.4. Single-Input/Single-Output Open-Loop Response Identification.

$$\hat{H}(f_k) = \frac{\hat{G}_{xy}(f_k)}{\hat{G}_{xx}(f_k)}, \qquad k = 0, 1, \ldots, N/2 \tag{3.8}$$

For the remainder of this dissertation, the estimate symbol (ˆ) and the discrete frequency dependency (f_k) are omitted, but they are implied throughout. The transfer-function results are presented in standard Bode form; that is, a plot of log-magnitude ($\text{dB} = 20 \log_{10}|H|$) and phase (deg) of H versus log-frequency ($\omega = 2\pi f_k$, rad/sec).

In the context of nonlinear systems analysis, the result presented in Eq. (3.8) is a describing function since it relates that part of the output which can be linearly related to the input (Ref. 33). In other words, this calculation results in an equivalent linear model, which minimizes the mean square difference between the actual output signal and its approximation by the fundamental harmonic (first sinusoidal component of the Fourier series). The remaining output harmonics are called remnants. Most of these are largely filtered out by the low-pass nature of the aircraft dynamics.

The piloting technique and time-history concatenation methods described above result in input amplitudes that are not constant over the frequency range. Therefore, the resulting describing function is representative of the average input amplitude over the ensemble time-history. Since the pilot inputs are typical of those experienced during normal flight operations, this approximation produces a satisfactory description of the vehicle dynamics in its normal operating environment.

A good indication of the quality of the first harmonic as a model of the input-to-output dynamics is obtainable from the coherence function (γ_{xy}^2) defined by

$$\gamma_{xy}^2 = \frac{|G_{xy}|^2}{|G_{xx}|\,|G_{yy}|} \tag{3.9}$$

which may be interpreted as that fraction of the output spectrum that can be accounted for by linear relation with the input spectrum (Ref. 29). When the process under investigation is perfectly linear and the spectral estimates are noise free, the coherence function will be unity within the excitation frequency-range. (The meaningless result of $\gamma_{xy}^2 \equiv 1$ also occurs when only one window section is used--that is, no averaging).

A coherence function of less than unity results from three basic causes (Refs. 28, 34). First, nonlinearities in the system may produce remnants which are not accounted for by the first harmonic approximation. When the input and output excursions are small, the system nonlinearities are less important. This is generally true for the cruise flight conditions. However, in hover, where low-frequency inputs induce large motions relative to the trim condition, nonlinear effects become more important; a significant reduction in the coherence function will result when first harmonic approximations are inadequate for representing these nonlinearities. In the higher-frequency range, where the excursions are smaller, the coherence function again approaches unity.

A second and very common cause of reduced coherence is input and output noise. The effect of noise sources differs chiefly depending on whether they are correlated with the input and output signals, and whether they act on the "process" or on the "measurement." Process noise (e.g., turbulence) contributes to the aircraft response, and so acts the same as a secondary (but unmeasurable!) input; the problem of secondary inputs is discussed below. Measurement noise does not contribute to the aircraft response, but it does contaminate the recorded input and output signals. Process and measurement noise are important because they cause errors in the estimate of the frequency response. These errors are categorized as "bias" (systematic) or "random" (nonsystematic). Bias error exists when the expected value of the ensemble-averaged frequency-response estimate $E[\hat{H}(f)]$ is different from the actual frequency response $H(f)$ or

$$b[\hat{H}(f)] \equiv E[\hat{H}(f)] - H(f)$$

Random error exists when there is a dispersion of the frequency-response estimates about the expected value for a collection of repeated runs:

$$\sigma[\hat{H}(f)] = +\sqrt{E[(\hat{H}(f) - E[\hat{H}])^2]}$$

Measurement noise is generally considered to be uncorrelated with the measured signal. Uncorrelated measurement noise at the output [v(t) in Fig. 3.5] does not bias the spectral estimate of Eq. (3.8). However, uncorrelated measurement noise at the input [u(t) in Fig. 3.5] does bias the estimate as a function of the noise-to-signal ratio (Ref. 28); so,

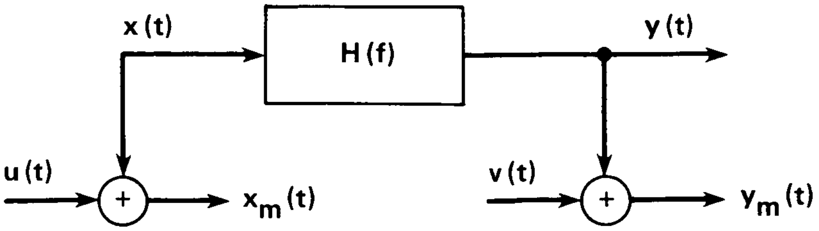

Fig. 3.5. Uncorrelated Measurement Noise at the Input and Output.

input sensors must be of the highest possible quality (ideally noise-free). Correlated measurement noise at the input or output or both will also bias the estimate. Uncorrelated measurement noise also causes random error, which is reflected by the drop in the coherence function. This coherence drop is often noticeable in the hover flight condition, where the pilot's low-frequency inputs are generally small. This also often occurs at higher frequency (above about 1 Hz), where the aircraft response is generally small. For a given level of coherence, a significant improvement in the spectral accuracy is obtained when multiple runs are concatenated, since the random (normalized) error ($\varepsilon_r = \sigma[\hat{H}]/H$) is inversely proportional to the number of independent time-history averages (Ref. 34):

$$\varepsilon_r = (\sqrt{0.55})\,\frac{[1-\gamma_{xy}^2]^{1/2}}{|\gamma_{xy}|\sqrt{2n_d}} \quad (\dagger) \qquad (3.10)$$

and

$$n_d = \frac{T_F}{L\Delta t} = \text{number of independent time-history averages}$$

where

T_F = Total concatenated run length, sec

L = Number of time-history points in the window

Δt = Time increment

---

† The factor of $\sqrt{0.55}$ accounts for the 45% reduction in spectral variance due to the 50% window overlapping used in this study (Ref. 31).

Based on the average window length $2T_{max} = 40$ sec, and two concatenated 90-sec runs, a random error of $\epsilon_r < 0.1$ (less than 10%) is achieved for a coherence function of $\gamma^2_{xy} \geq 0.85$.

The third source of reduced coherence results from secondary inputs; these are defined as inputs (other than the control which is undergoing a frequency-sweep, x in Fig. 3.6) which excite the system.

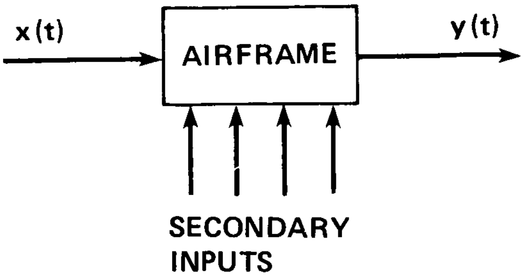

Fig. 3.6 Effect of Secondary Inputs on Single-Input/Single-Output Identification.

Secondary inputs occur from gusts and turbulence (process noise), and from off-axis control activity of the pilot or SCAS. The gust and turbulence inputs cannot be measured, they contribute to the measured response of the system, and they generally evoke correlated regulatory inputs from the pilot and the SCAS; therefore, the extracted frequency-responses are biased (see Sec. 3.2.4). Furthermore, the random error increases. Therefore, frequency-sweeps must be conducted in conditions of minimum wind and turbulence. The author's experience indicates that hover tests must be conducted with steady winds that are no greater than 5 knots and that cruise tests must be conducted with turbulence that is no greater than ±1 knot. The residual effects of small levels of gusts and turbulence are minimized by the concatenation of multiple frequency-sweep records. Pilot or SCAS inputs or both for regulation against excursions which occur in the coupled degrees-of-freedom also contribute to the system response; however, these inputs are measurable. If the secondary and primary inputs are not fully correlated, their effects can be separated by using the multi-input/multi-output identification method described in Sec. 3.2.5.

3.2.4 Identification of the Open-Loop Single-Input/Single-Output Frequency Response From Closed-Loop Tests

When the bare-airframe characteristics of the vehicle under study are highly unstable, as are those of the XV-15 in hover, execution of a 90-sec frequency-sweep on the open-loop configuration is not practical. The single-input/single-output bare-airframe frequency-response can be extracted from the closed-loop flight data using Eq. (3.8) subject to an important qualification. Referring to Fig. 3.7, the closed-loop system responds to commanded inputs (δ_{LAT}) and process noise (n). Identification of the open-loop frequency response (p/δ_a) requires the measurement of the output (p) and the surface deflection (δ_a)

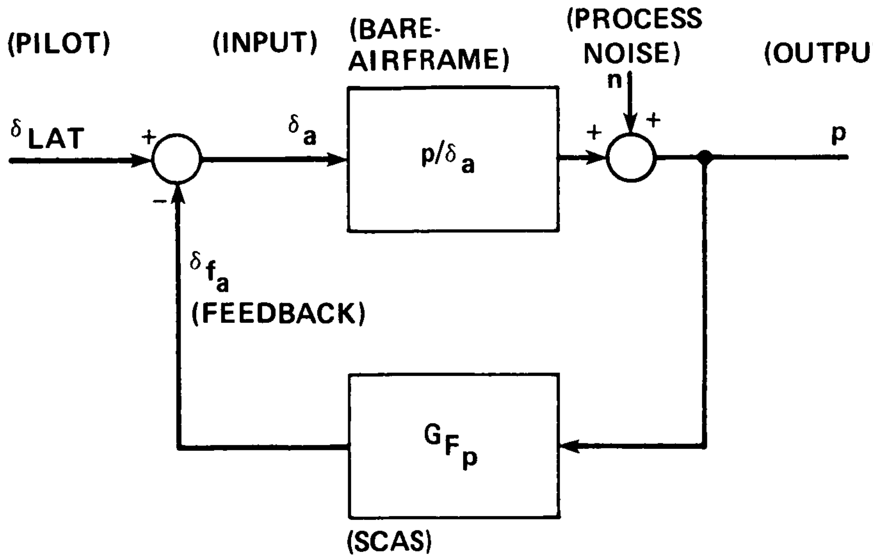

Fig. 3.7. Single Degree-of-Freedom Closed-Loop Roll-Response Model.

signals. This total surface deflection is made up of components from the pilot (δ_{LAT}) and the SCAS feedback (δ_{f_a}). Thus the identified frequency response of p/δ_a is also expressible as

$$\frac{p}{\delta_a}(s) = \frac{p}{\delta_{LAT} - pG_{F_p}} \tag{3.11}$$

When,

$$pG_{F_p} >> \delta_{LAT},$$

$$\frac{p}{\delta_a}(s) \longrightarrow \frac{-1}{G_{F_p}} \tag{3.12}$$

which is the troublesome result of identifying the inverse feedback frequency-response $-1/G_{F_p}$ in closed-loop pilot tracking tasks without a significant known external input (Ref. 35). The limiting condition of Eq. (3.12) is reachable only in the case of system excitation by process noise (n) (e.g., turbulence) with no pilot inputs ($\delta_{LAT} = 0$). However, biases in the open-loop frequency-response estimate obtained from Eq. (3.8) will occur even with non-zero pilot input ($\delta_{LAT} \neq 0$) whenever process noise is present; this occurs since the feedback loop causes the surface deflection to be partially correlated with the process noise (Appendix B). The amount of bias error depends on the noise-to-signal rms ratio $\hat{\sigma}(\omega)$ at each frequency; the numerical study presented in Appendix B shows that the (normalized) bias errors become significant ($\varepsilon_b = b[\hat{H}]/H > 0.10$; greater than 10%) when the system rms excitation that is due to process noise is greater than 33% of that that is due to pilot's inputs [$\hat{\sigma}(\omega) > 0.33$]. Total error (composed of normalized random and bias error) becomes significant (greater than 10%) at lower noise-to-signal rms ratios [$\hat{\sigma}(\omega) > 0.12$] depending on the level of feedback gain.

Therefore, the key requirement for identifying the open-loop frequency response from closed-loop flight data is that the total surface deflection (δ_a) must contain a significant component from the pilot (δ_{LAT}) which is uncorrelated with the output in the frequency range of interest. The "programmed" frequency-sweep input has good input power across the entire frequency range of concern, and persists throughout the duration of the time-history; as a result, it is especially good for closed-loop testing. Multi-step inputs are not particularly well suited for open-loop identification in closed-loop tests because the excitation occurs principally at the beginning of the run. Most of the long-term response is excited by fully-correlated inputs from the SCAS. The use of the frequency-sweep input and conducting the flight tests in low-turbulence conditions ensures that an accurate open-loop identification is achieved. SCAS-off step responses of the vehicle are compared with the extracted transfer-function model responses to verify that the true (unbiased) bare airframe frequency response is identified.

Identification of the unstable bare-airframe dynamics is thus greatly simplified since the pilot is flying the closed-loop (stable) aircraft. When turbulence is present, the remaining (secondary) degrees-of-freedom will be excited. For example, pitch and yaw motions will generally be present during lateral stick frequency-sweeps. However, if the roll response is completely decoupled from the pitch and yaw responses, the identified roll frequency-response and coherence functions will not be affected. For such aircraft, the pilot or stability-augmentation systems should be used to regulate against introducing disturbances into the secondary degrees-of-freedom. A problem arises, though, when coupled aircraft dynamics are considered.

3.2.5 Multi-Input/Multi-Output Frequency Response Identification in the Closed-Loop

Consider the case of coupled roll-yaw dynamics with SCAS feedbacks in both channels, as illustrated in Fig. 3.8. Following the preceding discussion, we assume that the total surface deflections (δ_a and δ_r) contain substantial components from the pilot inputs (δ_{LAT} and δ_{PED}) which are uncorrelated with the output responses.

Now suppose that a lateral-stick sweep is being executed to obtain the open-loop transfer function for yaw response to aileron (r/δ_a). Unlike the previous decoupled case, aileron inputs induce coupled responses in the yaw degree-of-freedom. If SCAS and pilot yaw feedbacks (G_{F_r}) act to restrain these coupled yaw excursions, the identified transfer function r/δ_a will be a greatly distorted indication of the actual bare-airframe transfer function.

In a general sense, yaw-rate feedback decouples the yaw and roll dynamics†; this may be desirable for assessing the open-loop roll response (p/δ_a) using the simplified one degree-of-freedom model (Fig. 3.4). However, when the interaxis-coupling characteristics are sought (p/δ_r, r/δ_a), artificial decoupling is not satisfactory. In hovering rotorcraft, rotor flapping dynamics induce interaxis coupling effects which may degrade piloted handling-qualities (Ref. 36); therefore, the identification of interaxis coupling responses is a specific concern.

---

† This assumes that L_{δ_r} is small, as it is in the present XV-15 case.

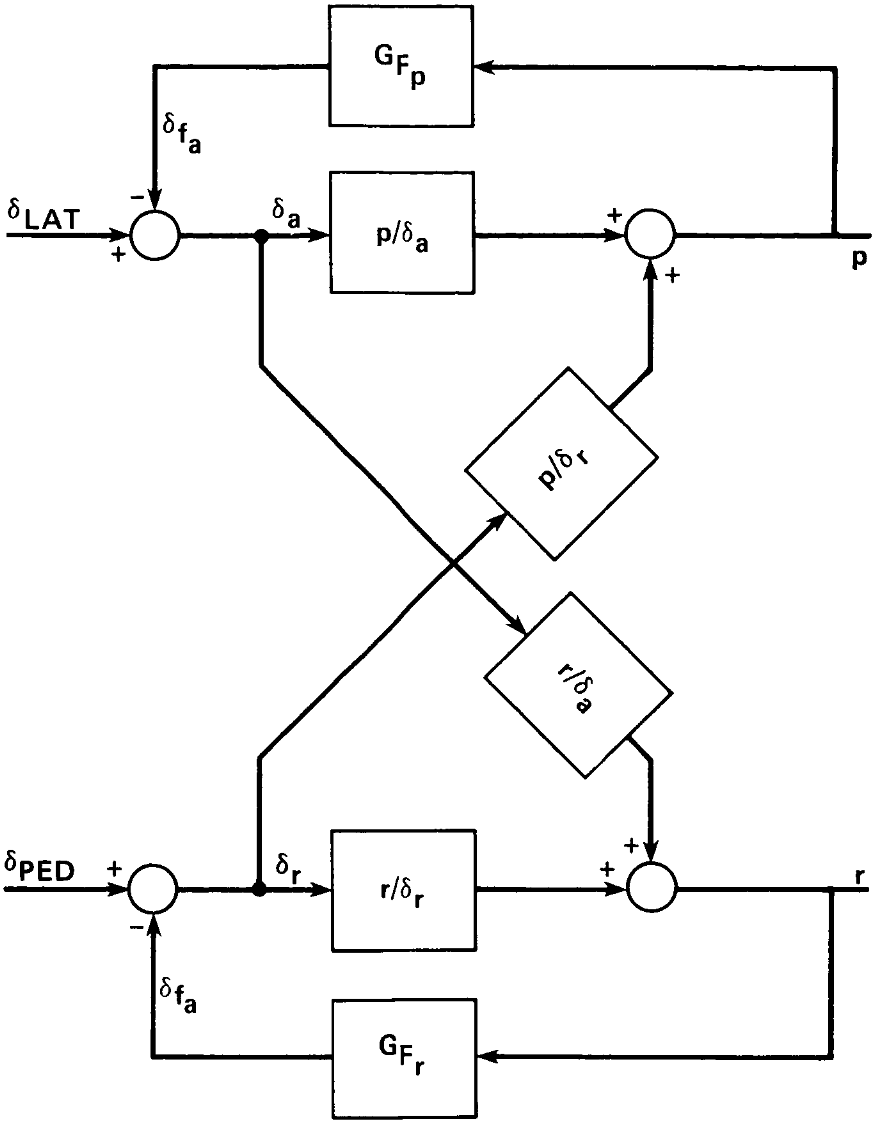
G_{F_p}
δ_{f_a}
δ_{LAT}
δ_a
p/δ_a
p
p/δ_r
r/δ_a
δ_{PED}
δ_r
r/δ_r
r
δ_{f_a}
G_{F_r}
+
−

Fig. 3.8. Coupled Roll/Yaw Response Model.

The two-input/single-output identification problem illustrated in Fig. 3.8 is a special case of the more general multi-input/single-output analyses discussed in Refs. 10, 28, and 29. The present analysis is limited to the two-input problem since the side-by-side rotor configuration of the XV-15 aircraft induces coupling between the roll and yaw degrees-of-freedom only (Chap. 2). (Identification of open-loop dynamics for single-rotor helicopters may require consideration of more than two-control inputs.)

The components of the yaw-rate spectrum resulting from the aileron and rudder inputs are determined from

$$G_{\delta_a r} = \left(\frac{r}{\delta_a}\right) G_{\delta_a \delta_a} + \left(\frac{r}{\delta_r}\right) G_{\delta_a \delta_r} \tag{3.13}$$

$$G_{\delta_r r} = \left(\frac{r}{\delta_a}\right) G_{\delta_r \delta_a} + \left(\frac{r}{\delta_r}\right) G_{\delta_r \delta_r} \tag{3.14}$$

The desired frequency responses are yaw-rate response to aileron (r/δ_a) and yaw-rate response to rudder (r/δ_r). These are given by the simultaneous solution of Eqs.(3.13) and (3.14):

$$\frac{r}{\delta_a} = \frac{G_{\delta_a r}[1 - (G_{\delta_a \delta_r} G_{\delta_r r}/G_{\delta_r \delta_r} G_{\delta_a r})]}{G_{\delta_a \delta_a}(1 - \gamma^2_{\delta_a \delta_r})} \tag{3.15}$$

$$\frac{r}{\delta_r} = \frac{G_{\delta_r r}[1 - (G_{\delta_r \delta_a} G_{\delta_a r}/G_{\delta_a \delta_a} G_{\delta_r r})]}{G_{\delta_r \delta_r}(1 - \gamma^2_{\delta_a \delta_r})} \tag{3.16}$$

It is clear from the above equations that the aileron and rudder inputs must not be fully correlated since this would result in an input cross-coherence $(\gamma^2_{\delta_a \delta_r})$ of unity, thereby rendering the desired frequency responses undefined (the "multipath propagation problem", Ref. 34). Then, only the (assumed) decoupled roll-rate response to aileron can be identified. Note also that if the inputs are fully uncorrelated, Eqs. (3.15) and (3.16) reduce to the single-input/single-output relations from Eq. (3.8).

Equations (3.15) and (3.16) can be written more compactly by defining

$$G_{\delta_a r\cdot\delta_r} \equiv G_{\delta_a r}[1 - (G_{\delta_a\delta_r} G_{\delta_r r}/G_{\delta_r\delta_r} G_{\delta_a r})] \qquad (3.17)$$

$$G_{\delta_a\delta_a\cdot\delta_r} \equiv G_{\delta_a\delta_a}(1 - \gamma^2_{\delta_a\delta_r}) \qquad (3.18)$$

$$G_{\delta_r r\cdot\delta_a} \equiv G_{\delta_r r}[1 - (G_{\delta_r\delta_a} G_{\delta_a r}/G_{\delta_a\delta_a} G_{\delta_r r})] \qquad (3.19)$$

$$G_{\delta_r\delta_r\cdot\delta_a} \equiv G_{\delta_r\delta_r}(1 - \gamma^2_{\delta_a\delta_r}) \qquad (3.20)$$

Each quantity defined in Eqs. (3.17)-(3.20) has important physical significance. For example, $G_{\delta_a r\cdot\delta_r}$ is the cross-spectrum from aileron input to yaw-rate response (δ_a to r) with the linear effect of yaw-rate due to rudder excitation removed. This quantity is termed the "conditioned (or residual) cross-spectrum" because the "ordinary" cross-spectrum ($G_{\delta_a r}$) has been conditioned to remove the biasing effects of partially-correlated rudder excitation. Similarly, the quantity $G_{\delta_a\delta_a\cdot\delta_r}$ is termed "conditioned input autospectrum," because the ordinary input autospectrum ($G_{\delta_a\delta_a}$) has been conditioned to remove the partially-correlated contribution of δ_r inputs. The remaining quantities of Eqs. (3.19) and (3.20) have analogous interpretations.

The desired frequency responses of Eqs. (3.15) and (3.16) are then expressed as:

$$\frac{r}{\delta_a} = \frac{G_{\delta_a r\cdot\delta_r}}{G_{\delta_a\delta_a\cdot\delta_r}} \equiv r/\delta_a\cdot\delta_r \tag{3.21}$$

$$\frac{r}{\delta_r} = \frac{G_{\delta_r r\cdot\delta_a}}{G_{\delta_r\delta_r\cdot\delta_a}} \equiv r/\delta_r\cdot\delta_a \tag{3.22}$$

which are in the form of the single-input/single-output relation of Eq. (3.8) with cross-spectrum replaced by conditioned cross-spectrum, input-autospectrum replaced by conditioned input-autospectrum, and frequency response replaced by conditioned frequency-response.

A generalization of the ordinary coherence function concept presented above allows the quality of the conditioned frequency-response estimates to be assessed. The partial coherence function is defined as that fraction of the output that can be linearly related to a single input with the linear effects of all remaining inputs removed. It is interpreted in exactly the same way as the ordinary coherence functions for single-input/single-output systems described earlier Eq. (3.9), and has the same form. For the coupled system of Fig. 3.6, the partial coherence of yaw response to aileron with the linear effects of the rudder inputs removed ($\gamma^2_{\delta_a r\cdot\delta_r}$) is calculated by

$$\gamma^2_{\delta_a r\cdot\delta_r} = \frac{|G_{\delta_a r\cdot\delta_r}|^2}{|G_{\delta_a\delta_a\cdot\delta_r}|\,|G_{rr\cdot\delta_r}|} \tag{3.23}$$

where $G_{\delta_a r\cdot\delta_r}$ and $G_{\delta_a\delta_a\cdot\delta_r}$ are defined in Eqs. (3.17) and (3.18), respectively; and where

$$G_{rr\cdot\delta_r} \equiv G_{rr}(1 - \gamma^2_{\delta_r r}) \tag{3.24}$$

is termed the "conditioned output autospectrum" because it is the ordinary output autospectrum (G_{rr}) with the linear effect of partially correlated rudder excitation removed. The corresponding partial coherence of yaw-rate response to rudder with the linear effects of aileron inputs removed ($\gamma^2_{\delta_r r \cdot \delta_a}$) can be obtained by interchanging δ_r and δ_a in Eq. (3.23).

Another useful metric is the multiple coherence function. This is the fraction of the output that may be linearly correlated to all of the inputs being considered. For the two-input case, the multiple coherence ($\gamma^2_{\delta_a \delta_r : r}$) is given by[†]

$$\gamma^2_{\delta_a \delta_r : r} = \frac{(r/\delta_a) G^*_{\delta_a r} + (r/\delta_r) G^*_{\delta_r r}}{G_{rr}} \qquad (3.25)$$

The multiple coherence will be less than unity when input and output noise or nonlinearities are present, or when additional secondary control inputs contribute to the aircraft response but are not included in the multi-input analysis. As before, the identified transfer functions will incorrectly appear decoupled when these additional secondary inputs are not taken into account.

The two-input/single-output spectral analysis calculations of Eqs. (3.15)-(3.25) may be performed using a computer program (TISOSA) developed by the author. The inputs to the program are the single-input/single-output spectral-response results of FRESPID, and a command file which contains the execution directives. The program outputs are the conditioned spectral-response plots and a data file.

[†] Asterisk (*) denotes complex-conjugate.

3.3 Transfer-Function Modeling

With the flight-test frequency responses in hand, the next step in the identification method of Fig. 1.3 is the derivation of transfer-function models. This step involves three important considerations which are treated in the next sections:

1. Order and form of transfer-function model
2. Fitting range and relative weighting of the magnitude and phase curves
3. Multi-degree-of-freedom models

3.3.1 Selection of Model Order and Form

Analytical transfer-function forms are selected for each input-output pair. These are based on configuration and flight condition considerations and must have a sufficient number of free parameters to adequately fit the identified frequency response over the frequency range of concern. In the hover flight condition, vehicle (rigid body) dynamics are dominated by the hovering cubic and decoupled heave and yaw modes. In wing-borne flight, the conventional longitudinal and lateral quartic equations dominate. Thus, transfer-function models which are appropriate for the hover flight condition are not necessarily applicable to forward-flight conditions. Obviously, if a model of high enough order is selected, the parameters can be adjusted to accommodate each flight condition. However, such transfer-function models no longer retain the physical significance of the classical lower-order parameters and are often not unique (Ref. 6). Also, higher-order transfer-functions models tend to be strongly tuned to the specific inputs which are used in the identification procedures (e.g., a frequency-sweep) and can be very poor predictors of responses to other test inputs (e.g., step and pulse inputs) and responses at nearby flight conditions. Therefore, higher-order models are not desirable. The appropriate transfer-function order is the minimum order which can satisfactorily fit the frequency responses, with the upper limit taken as the physical order of the system.

3.3.2 Transfer-Function Fitting Range and Relative Weighting

The maximum frequency range usable for transfer-function fitting corresponds to the region of acceptable coherence. Often, however, the frequency range of suitable coherence extends beyond the range of applicability of the selected transfer-function models. For example, in the XV-15 cruise identification (Chap. 5), a simple short-period model is assumed, since it adequately characterizes the rigid-body pitch dynamics in the broad frequency range of 0.3-10 rad/sec. At the lowest input frequencies (0.1-0.3 rad/sec), the vehicle response is dominated by the lightly damped phugoid dynamics; these dynamics are not very important for piloted handling-qualities related to attitude control tasks and so can be ignored for the present study. By restricting the fitting range to 0.3-10 rad/sec, where the short-period model is appropriate, the physical significance of the parameters is maintained. In other cases, structural resonances may be present at the high-frequency end of the range of good coherence. If a rigid body transfer-function model is assumed, the fitting range must be restricted to exclude the effects of such resonances (Ref. 6).

The interactive computer program NAVFIT, originally developed at McDonnell Aircraft Company by Hodgkinson and Buckley (Ref. 37) and enhanced by the author to access the output file from the FRESPID program, fits the frequency-response data with a selected transfer-function model. The numerator and denominator orders are arbitrary, and a time delay can be included to approximate the effects of unmodeled high-frequency dynamics. Least-squares fitting is completed using up to 50 points spaced linearly across the logarithmic frequency scale in the desired frequency range. The relative weighting of the magnitude and phase errors is arbitrary, but a commonly selected value for handling-qualities applications is 1 dB magnitude error to 7 deg phase error† (Ref. 17). The outputs from the NAVFIT program are closed-form transfer-function models and plotted frequency-response comparisons of the flight data and model.

3.3.3 Fitting Multi-Degree of Freedom Frequency Responses

A good review of the practical considerations involved in transfer-function fitting is given by Bischoff and Palmer (Ref. 15). They found that satisfactory identification of the transfer-function parameters generally requires the simultaneous consideration of at least two degrees-of-freedom. By constraining the transfer-function models to contain mutual denominator factors (as they do physically), the location of numerator factors becomes much better defined. In the cruise condition, for example, the denominators of the longitudinal transfer functions relating elevator inputs to normal-acceleration and pitch-rate outputs (a_z/δ_e and q/δ_e) are the same. Simultaneously fitting these degrees-of-freedom maintains the commonality of the denominator factors (the short-period mode), and avoids the "galloping L_α" problem (this refers to the problem of a poorly defined pitch-rate numerator location in single-input/single-output q/δ_e identification, Ref. 17). Two computer programs (LONFIT and LATFIT) were developed at McDonnell Douglas Aircraft Company by Givan, LaManna, and Hodgkinson (Refs. 38, 39) and modified by the author to allow multiple-degree-of-freedom fitting of the frequency-response output files from FRESPID. A new option incorporated by the author into LONFIT allows the identification of the instantaneous center-of-pitch rotation, χ_{cg} (Sec. 5.2.2).

---

†Professor Stephen P. Boyd notes that this is the natural weighting that is obtained when the fit is performed on a real-imaginary plot of the 20 $\log_{10}$ values of the complex transfer-function.

3.4 Time-Domain Verification of Transfer-Function Models

Time-domain verification involves driving the extracted transfer-function models with the flight data for inputs not used in the identification procedure and comparing predicted and actual time histories. This analysis is necessary to check a number of important assumptions and steps in the frequency-domain method:

Linearity assumption: The adequacy of linearized lower-order models in describing the time-domain dynamics of nonlinear systems is always a key question--especially for helicopters in hovering flight. Since the reference condition is zero velocity, even small translational-velocity perturbations can produce significant changes in the dynamic response characteristics. Lateral and longitudinal frequency sweeps can involve translational velocities of up to 40 ft/sec at low frequencies, so a unique lower-order linear model may not be achievable for the entire frequency range (Ref. 22). As discussed earlier, the extracted transfer-function model is actually a describing function that is strictly valid only for the input amplitudes which are used in the flight test experiment. However, since the motions encountered during frequency-sweep testing are typical of those in near-hover maneuvering flight, the extracted describing functions are generally quite suitable. Time-domain verification checks this assumption.

Transfer-function fitting mismatch: Sometimes, apparently small mismatches in the frequency-domain fit can produce surprisingly large discrepancies in time-domain correlations, especially when these mismatches occur in the frequency range near the dominant vehicle modes. If the identified model poorly predicts the time-domain verification response, the transfer-function model order and structure is adjusted to improve the correlation.

Overtuned models: Identification procedures tend to be tuned to the type of test inputs used (e.g., a frequency-sweep), and their accuracy in predicting responses to other classes of inputs (e.g., steps and doublets) is often uncertain. The possibility of overly-tuned models increases as the order of the transfer function is increased (Ref. 40). By testing the transfer-function model with other input forms, overtuning is avoided.

Identification of the open-loop frequency response from closed-loop flight data: Although a complete 90-sec frequency-sweep cannot be generated on the open-loop unstable XV-15 aircraft in hover, shorter duration open-loop step and pulse inputs are possible. Comparisons of these SCAS-off responses with the extracted transfer-function models verifies that the true (unbiased) open-loop vehicle response, instead of the inverse feedback transfer-function (at worst), has been identified.

3.4.1 Time-Domain Verification Method

Time-domain verification may be done by converting the transfer functions to canonical form:

$$\left.\begin{aligned} \dot{\underline{x}}(t) &= F\underline{x}(t) + G\underline{u}_F(t) \\ \underline{y}(t) &= C\underline{x}(t) \end{aligned}\right\} \tag{3.26}$$

where

$$F = \begin{bmatrix} 0 & 1 & 0 & \cdots & 0 \\ 0 & 0 & 1 & \cdots & 0 \\ \cdot & & & & \\ \cdot & & & & \\ \cdot & & & & \\ -a_0 & -a_1 & -a_2 & & -a_{n-1} \end{bmatrix} \qquad G = \begin{bmatrix} 0 \\ 0 \\ \cdot \\ \cdot \\ \cdot \\ 1 \end{bmatrix}$$

$$C = \begin{bmatrix} b_0 & b_1 & \cdots & b_m & 0 & \cdots & 0 \end{bmatrix}$$

and $a_0, a_1, \ldots, a_{n-1}$ are the denominator (ascending coefficients) and $b_0, b_1, \ldots, b_m$ are the numerator (ascending) coefficients of the transfer-function model being evaluated.

The control input to the system u_F is the low-pass filtered time-history of the surface deflection signal (e.g., δ_a in Fig. 3.7). The filter cutoff frequency is selected to eliminate spectral components of the test inputs (steps and pulses) which are above the frequency range of applicability of the derived transfer-function models (e.g., the upper bound of the least-squares fitting range, Sec. 3.3.2) (Ref. 6).

State derivative biases and output reference values are included as unknown constants in the perturbation model of Eq. (3.19), representing drifts and zero shifts, to allow a comparison with the flight responses:

$$\dot{\underline{x}}(t) = F\underline{x}(t) + Gu_F(t) + \underline{bx}$$

$$y(t) = C\underline{x}(t) + y_{ref} \tag{3.27}$$

These bias and reference values are determined from a least-squares fit of the model response $y(t)$ and the low-pass filtered flight data $y_F(t)$ [with $\underline{x}(0) \equiv 0$ to avoid overparameterizing the model]. The more common practice of simply subtracting the initial values of control and output from the time-histories can be used when the vehicle dynamics are stable, since drifts and reference errors decay with the time-constant of the transfer-function poles. However, when the identified transfer function is highly unstable, as it is in the pitch and roll dynamics of the XV-15 in hover, small errors in the biases and reference values quickly propagate and the responses diverge even for a highly accurate model. A computer program (TFTHISTORY) was developed by the author to estimate state-derivative biases and output reference values using a least-squares procedure (a simpler but still satisfactory alternative to a Kalman filter or smoother estimate), generate the model time-history, and compare the result with the filtered flight time-history data.

This completes the discussion of the frequency-domain identification method. Identification results for the hover and cruise flight conditions are presented in Chapters 4 and 5.

Chapter 4

HOVER DYNAMICS

This Chapter discusses the identification and analysis of the XV-15 open-loop dynamics in hovering flight. The transfer functions of primary interest for handling-qualities are associated with "inner-loop" regulation of the on-axis responses: pitch-rate response to elevator (q/δ_e), vertical-acceleration response to power lever (a_z/δ_c), yaw-rate response to rudder (r/δ_r), and roll-rate response to aileron (p/δ_a). The important coupling transfer function is yaw-rate response to aileron (r/δ_a). To illustrate the identification method described in Chapter 3, the lateral/directional on-axis and coupled dynamics are discussed in detail. Flight-extracted frequency-responses are compared with piloted-simulation responses. The simulator responses are from the model states, so the drive dynamics of the vertical motion simulator (VMS) motion-base system are not included. Comparisons of the flight responses and the current nonreal-time simulation model (Ref. 3) are also included to show the substantial modeling improvements that have been made in the 3 years since the VMS simulation tests were conducted. Closed-form transfer-function models of the flight responses are obtained using least-squares fits. Finally step-response time-history matching is used to verify the predictive capability of the identified transfer functions.

The results presented in this Chapter are considerably improved over the original hover flight condition results presented in Ref. 18. Subsequent experience on the XV-15 and related identification efforts

(Refs. 6, 21-24) led to refinements in the analysis methods and insight into techniques for extracting higher-quality results.

4.1 Lateral/Directional Dynamics

The frequency-sweeps in roll were the most difficult to execute because of significant interaxis coupling between lateral stick inputs and yaw response. Since the yaw SCAS employs a washed-out yaw-rate feedback, low-frequency yaw-attitude excursions required continuous pilot regulation during the lateral stick frequency-sweeps. However, a two-input analysis of the roll-axis response showed very little effect of the pedal inputs on the single-input aileron transfer function. This suggests that rudder inputs produce largely decoupled yawing motions; this is a typical assumption for hovering aircraft (Ref. 41). Therefore, the following analysis of the roll dynamics considers only the single-input/single-output transfer function p/δ_a.

4.1.1 On-Axis Responses

The lateral-stick inputs for two good frequency-sweeps were concatenated to form the composite input time-history of Fig. 4.1. The 20-sec

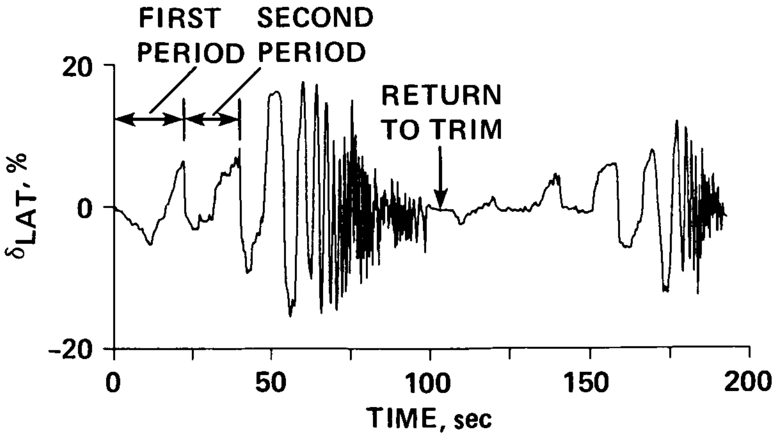

Fig. 4.1. Two Lateral-Stick Frequency-Sweeps (δ_{LAT}) in Hover.

low-frequency cycles result in large lateral-velocity variations (10-20 knots). At the higher frequencies, stick deflections are larger, roll rates are smaller, and velocity perturbations are less than 5 knots. Both runs are roughly 90 sec in duration, but the distribution of frequency content in each is seen to be quite different. The first frequency-sweep contains more mid-frequency power, whereas the second contains more low-frequency power. The input autospectrum for the concatenated time-history is shown in Fig. 4.2. Maximum input power is

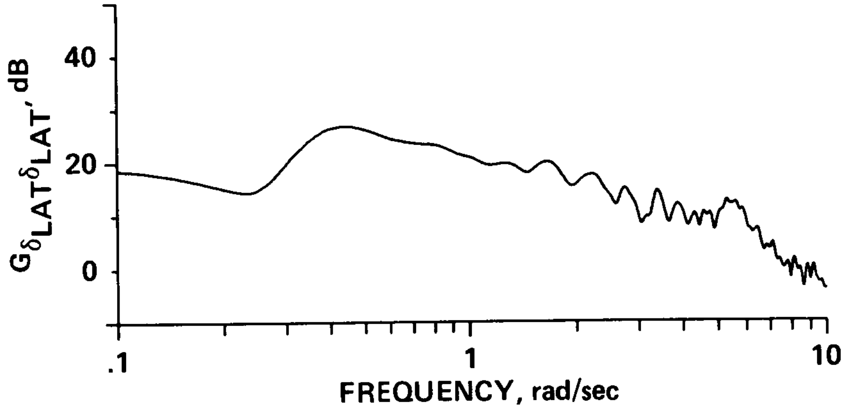

Fig. 4.2. Lateral-Stick Input Autospectrum ($G_{\delta_{LAT}\delta_{LAT}}$).

generated at a frequency of $\omega = 0.4$ rad/sec, which is slightly higher than that corresponding to the maximum period of $T_{max} = 20$ sec. The input power remains strong out to $\omega = 6$ rad/sec, and then falls off rapidly at the higher frequencies. The frequency content which exists below the minimum even-input frequency (1/20 Hz) and above the maximum even-input frequency (4 Hz) (not shown in Fig. 4.2) is due to the various nonsinusoidal components which are apparent in the pilot input (Fig. 4.1).

The corresponding aileron surface deflection time-history is shown in Fig. 4.3. This signal reflects inputs from the pilot (and shaped by

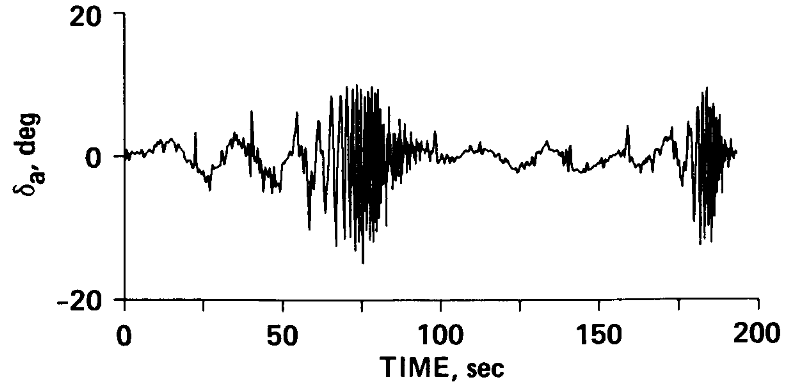

Fig. 4.3. Aileron Surface Deflections (δ_a) during the Lateral-Stick Frequency Sweeps, Reflecting Contributions From Pilot and SCAS Inputs.

SCAS feed-forward elements) and from the SCAS feedbacks. Once again, the first frequency-sweep has more mid- and high-frequency power, and the second frequency-sweep has more low-frequency power. The input autospectrum for the concatenated surface deflection signal is shown in Fig. 4.4. The autospectrum peaks at $\omega = 0.3$ rad/sec (= low-frequency

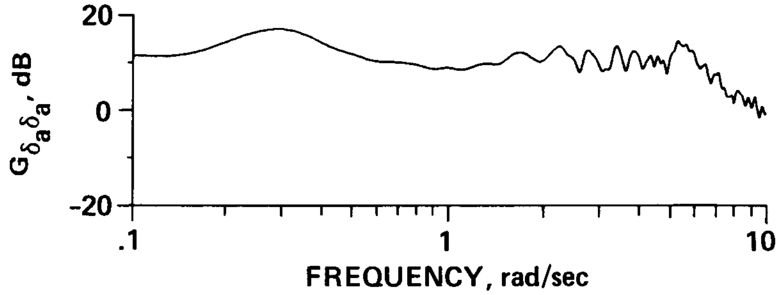

Fig. 4.4. Aileron Surface Input Autospectrum ($G_{\delta_a\delta_a}$).

input) and is roughly constant up to 6 rad/sec. The fact that both the lateral-stick input autospectrum and surface-deflection input autospectrum are strong indicates that the surface deflection contains a significant component from the pilot's stick inputs (thus avoiding the $-1/G_f$ problem discussed in Chap. 3).

The roll-rate responses for the two lateral frequency-sweeps are shown in Fig. 4.5. The roll-rate amplitudes vary from 5-10 deg/sec, depending on input frequency. The output autospectrum (Fig. 4.6) peaks between 0.3 and 0.5 rad/sec, because of the low-frequency input cycles and the presence of the dominant roll modes in this frequency range. Although the input surface autospectrum remains roughly constant for $\omega > 1$ rad/sec, the output spectrum falls off rapidly because of the

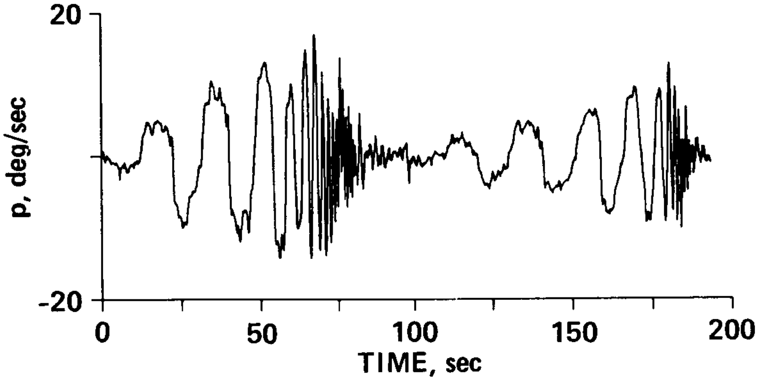

Fig. 4.5. Roll-Rate Response (p) during Lateral-Stick Frequency-Sweeps.

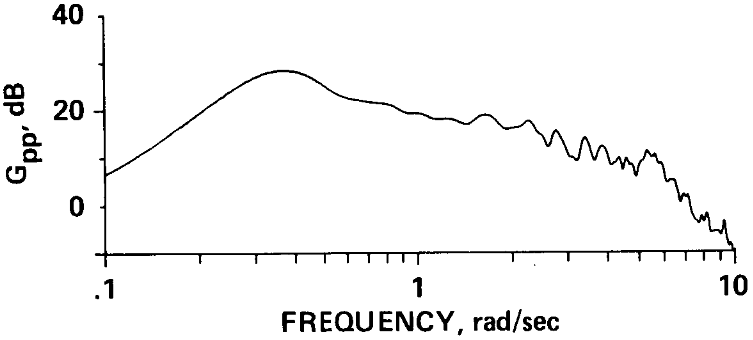

Fig. 4.6. Roll-Rate Output Autospectrum (G_{pp}).

rigid-body (inertial) response of the aircraft. The cross-spectrum between aileron and roll rate (Fig. 4.7) is quite similar in form to the roll-rate output autospectrum (Fig. 4.6) because the aileron input autospectrum (Fig. 4.4) is roughly constant with frequency.

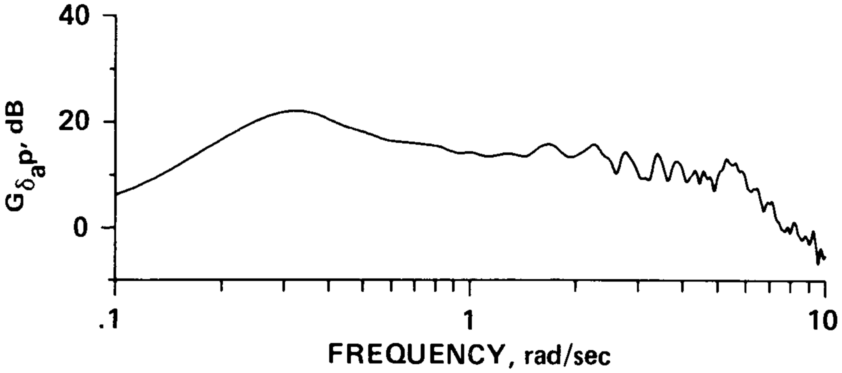

Fig. 4.7. Magnitude of Cross-Spectrum between Aileron Surface Inputs and Roll-Rate Response ($G_{\delta_a p}$).

The frequency response of p/δ_a is shown in Fig. 4.8. Once again, the magnitude response peaks between 0.5 and 1 rad/sec, a result of the dominant roll modes which are in this frequency range. For frequencies greater than 1 rad/sec, the Bode plot shows the classic -20 dB/decade roll-off caused by the K/s (inertial) roll-rate response of the aircraft. The phase increase in the vicinity of the magnitude peak (ω = 0.3-0.6 rad/sec) indicates that the dominant roll dynamics are unstable. At higher frequencies, the phase is roughly -90 deg because of the inertial response and the small high-frequency lags.

The coherence function for the roll-rate response identification is shown in Fig. 4.9. Excellent coherence is achieved in the frequency ranges of 0.2-0.3 rad/sec and 0.6-9 rad/sec. The coherence function drops sharply in the frequency range in which the input and output

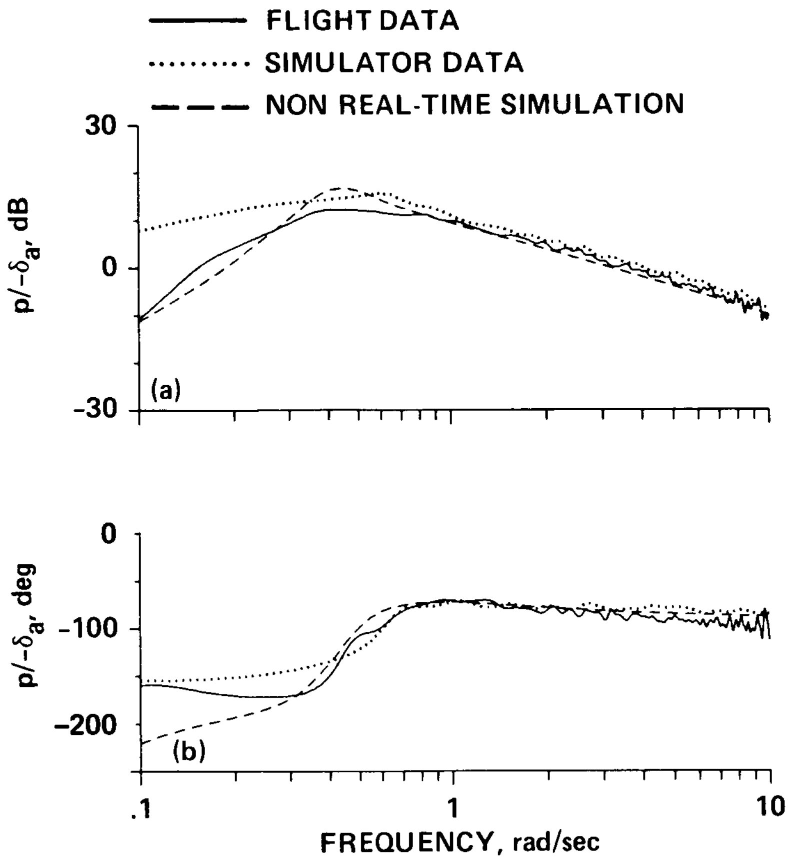

Fig. 4.8. Roll-Rate Response to Aileron ($p/-\delta_a$). (a) Magnitude; (b) Phase.

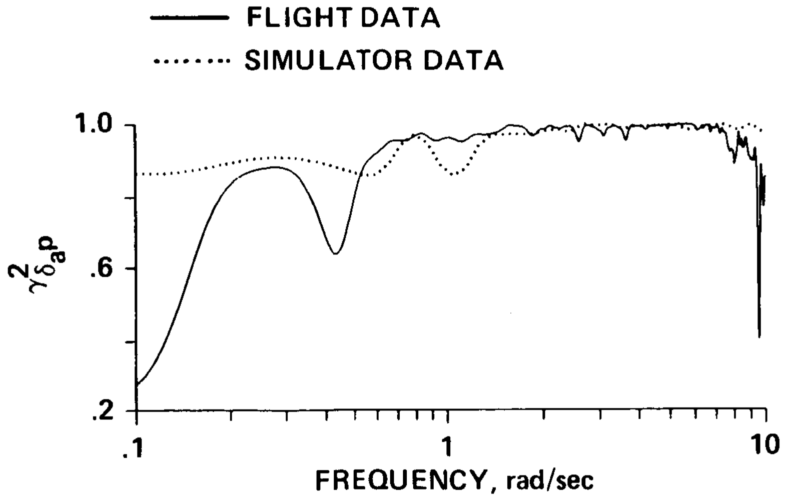

Fig. 4.9. Coherence Function for Roll-Rate Response Identification ($\gamma^2_{\delta_a p}$).

autospectrum are both very strong and the transfer function peaks (0.3-0.6 rad/sec). This indicates that nonlinear behavior is present in the low-frequency unstable dynamics. Current research by the author and Kaletka (Ref. 22) shows that a major source of this nonlinearity is rolling-moment dependency on higher powers of lateral velocity [$L(v^2)$, $L(v^3)$]. For frequencies below 0.2 rad/sec and above 9.0 rad/sec, the coherence function drops rapidly because of the lack of excitation outside of the frequency range of dominant pilot inputs.

The spectral results presented thus far are impressive in terms of their smoothness, resolution, and coherence. The chirp z-transform, described earlier, is a significant improvement over the standard (Cooley-Tukey) FFT methods, which were found to produce much poorer frequency-response resolution and associated erratic coherence-function behavior at low frequency. This is because resolution of the standard FFT is limited by the length of the window, whereas the chirp z-transform has arbitrary resolution (Sec. 3.2.2). In addition, the concatenation of good repeat runs is seen to produce a reasonably constant input (surface) autospectrum over the frequency range of interest, and provides a large number of sections for the averaging process. This ensures minimal random error and satisfactory accuracy of the transfer-function estimates, even when the magnitude of the coherence function is low (for example near $\omega = 0.4$ rad/sec in Fig. 4.9).

The hover frequency-sweep tests and analysis described above for the flight vehicle were repeated in the VMS. The extracted aileron-to-roll-rate open-loop transfer function is shown in Fig. 4.8 for comparison with the flight results. The associated coherence function shown in

Fig. 4.9 reflects excellent simulator identification for the entire range of 0.1-10 rad/sec.

The correlation of the VMS simulation and the flight data is very good for the frequency range 1.0-10.0 rad/sec, indicating that the roll-control-response sensitivity is accurately modeled. The low-frequency phase comparison suggests that the damping ratio of the unstable roll mode is slightly overestimated by the simulation model (more unstable), and the natural frequency is accurate.

An interesting demonstration of the effects of nonlinearities in the low-frequency roll dynamics (p/δ_a) is presented in Fig. 4.10. This figure compares the simulator frequency-sweep result with the small-perturbation transfer function (obtained by numerically linearizing the VMS simulation model). The perturbation transfer-function matches the sweep results well in the high-frequency range ($\omega > 3.0$ rad/sec) where motions are small; however, considerable deviation occurs in the low-frequency end, clearly a result of the large-perturbation nonlinear effects. (The large phase shift at low frequency is due to low-frequency, right-half plane poles and zeroes in the simulator perturbation transfer-function.) For forward-flight conditions, the differences were found to be much less significant since rotor nonlinearities are overshadowed by the linear aerodynamics of the wing and tail, and flight-path excursions about the steady-state trim condition are smaller.

The fact that the simulation (and flight data) coherence function remains strong at low frequencies (Fig. 4.9) leads to the important conclusion that the dominant nonlinear effects can be well approximated by linear (but not small-perturbation) describing functions. By fitting

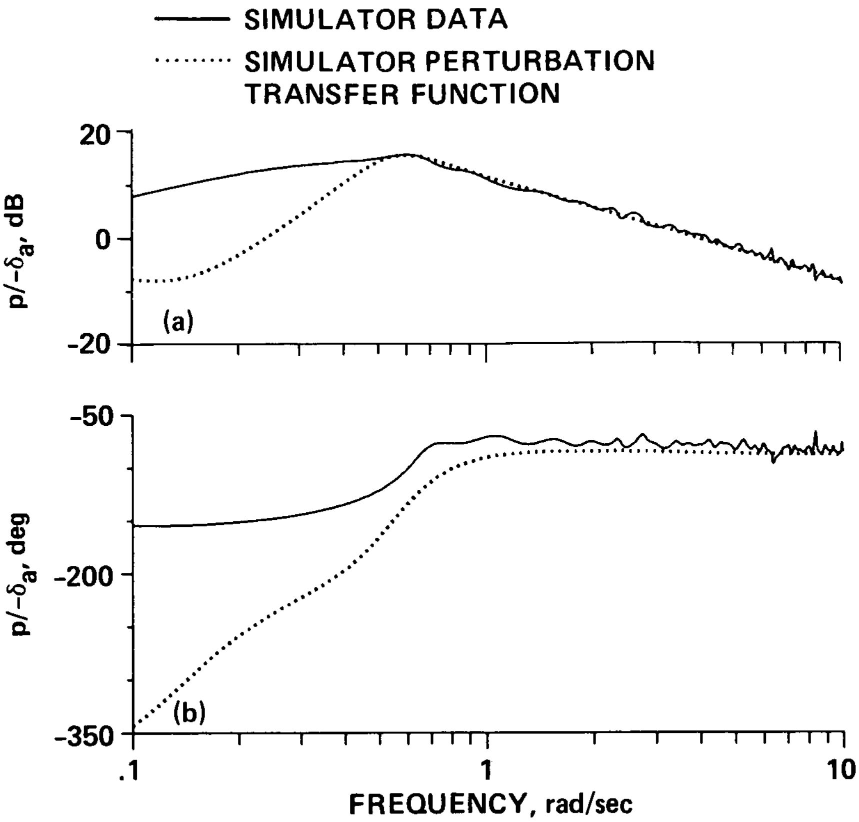

Fig. 4.10. Comparison of Small-Perturbation Transfer-Function and Frequency-Sweep Responses Obtained from the Simulation; Data Presented are for the Roll-Rate Response to Ailerons, $p/-\delta_a$. (a) Magnitude; (b) Phase.

these describing functions with standard transfer-function forms, the physical significance of the small-perturbation model parameters is retained, and the numerical values of these parameters reflect the gross nonlinear effects. This "equivalent low-order modeling" approach has been useful in analyzing and predicting the handling qualities of many aircraft (Refs. 15, 17).

The low-frequency errors in the simulation, which are shown in Fig. 4.8, were also reported during the pilot's qualitative evaluation. Subsequent analysis of the real-time mathematical model indicated problems in the representation of rotor flapping for large lateral-velocity changes (such as occurs in the low-frequency range of the frequency-sweep). There is strong sensitivity of the numerically linearized perturbation transfer-functions to the size of the perturbation increments. Corrections to the mathematical modeling in these two areas were included later in the nonreal-time XV-15 simulation. The comparison between the current nonreal-time mathematical model, the VMS original model, and the flight data is shown in Fig. 4.8; it indicates the significant improvements that have been achieved during the last 3 years of development.

The identified yaw-rate response to rudder inputs r/δ_r is presented in Fig. 4.11. The associated coherence function (Fig. 4.12) shows that the identification is accurate from 0.1-3.0 rad/sec; above this range, the erratic coherence behavior suggests a less accurate estimate.

The yaw-rate response follows the K/s characteristic in magnitude and phase for frequencies greater than 0.5 rad/sec, which means that rudder inputs generate constant yaw-rate accelerations. The fact that the phase does not rise above the -90 deg value except at very low frequencies suggests an associated low value of yaw damping (N_r) as compared to conventional helicopters. This is due to the lack of a tail rotor for the tilt-rotor configuration.

A comparison of the simulator yaw-rate response with the flight-test data is presented in Figs. 4.11 and 4.12. As in the roll axis, the magnitude response generally matches very well for higher frequencies $\omega > 1.0$ rad/sec. The parallel (vertical) shift in the magnitude curve

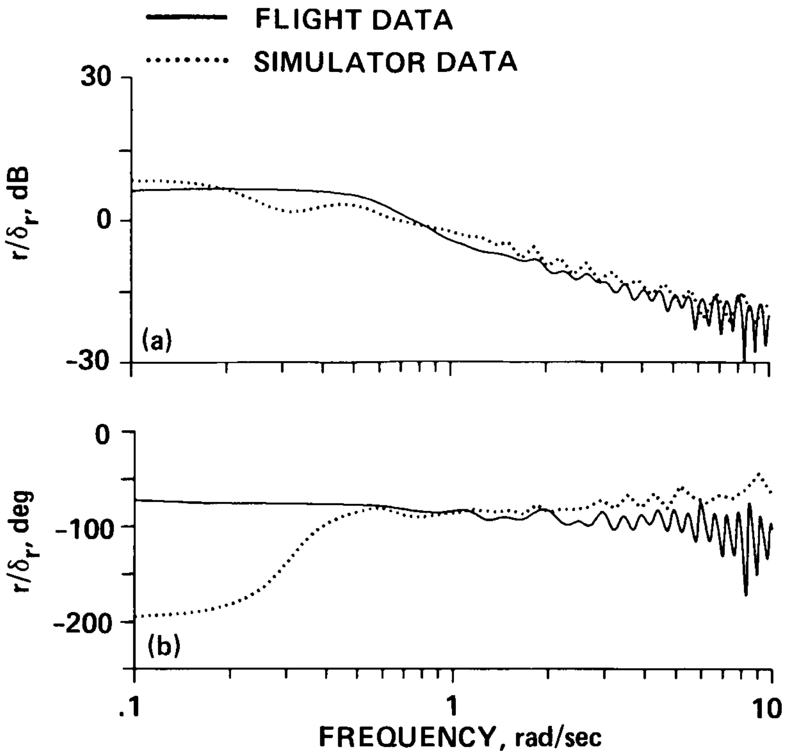

Fig. 4.11. Yaw-Rate Response to Rudder (r/δ_r). (a) Magnitude; (b) Phase.

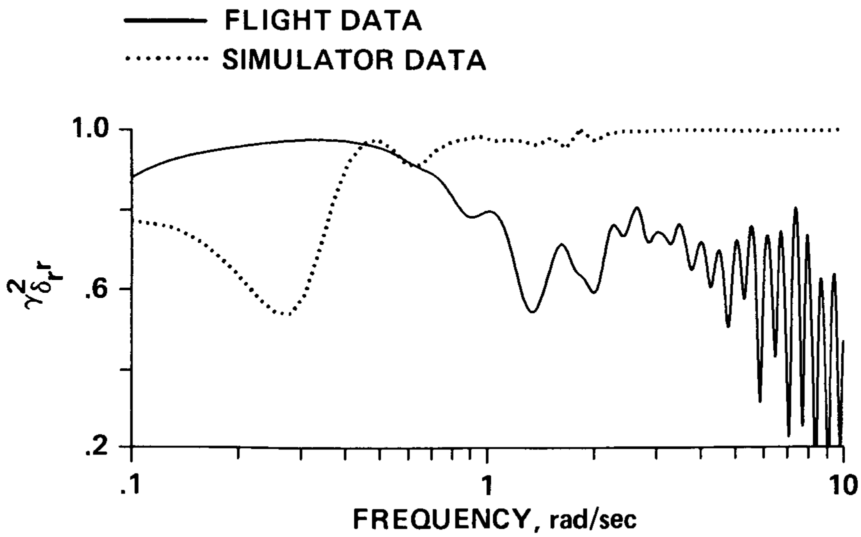

Fig. 4.12. Coherence Function for Yaw-Rate Response Identification ($\gamma^2_{\delta_r r}$).

indicates that the control sensitivity is overestimated by about 30%. Subsequent analyses as a result of this finding indicate that ballast, which was added in the tail (for c.g. control), was not accounted for in the simulation model. This added inertia reduces the control sensitivity and, therefore, could contribute to the observed high-frequency discrepancy.

The yaw-mode damping is significantly underestimated in the simulator, as can be seen from the low-frequency phase drop (which actually indicates an unstable response!) compared with the (stable) flight response (Fig. 4.11b). This discrepancy was verified in step-response comparisons between the aircraft and the simulator. A likely cause of error in the yaw damping is the assumption of uniform lateral distribution of the rotor inflow. Wing-on-rotor interference on the inboard half of the rotor disks probably causes a significant distortion in the shed wake and consequently in the lateral inflow distribution in hovering flight. The assumption of uniform inflow causes an underestimation in the longitudinal flapping response to longitudinal velocity changes (Ref. 42), which is the primary source of yaw damping for the hover flight condition. Even minor coupling to the (unstable) roll dynamics could then result in the observed unstable yaw simulation response.

With the flight and simulation frequency-responses now identified and compared, the next step in the method of Chapter 3 is to derive lower-order equivalent transfer functions. Examination of the roll and yaw frequency-responses of Figs. 4.8 and 4.11 shows that they exhibit classic characteristics of hovering vehicles. The yaw response is decoupled and first-order in nature; the roll response is dominated at low-frequency by the unstable complex mode and has one excess pole at high frequency. Thus, the yaw-rate response to rudder inputs is modeled by

$$\frac{r(s)}{\delta_r(s)} = \frac{N_{\delta_r} e^{-\tau_\psi s}}{(s + 1/T_y)} \tag{4.1}$$

where $r(s)/\delta_r(s)$ is the Laplace-transformed yaw-rate response to rudder, in degrees per second per degree, and s is the Laplace-transform variable. The transfer-function high-frequency gain (N_{δ_r}) is the yaw-control response sensitivity, that is, the initial yaw-acceleration response (deg/sec^2) to a 1-deg step input in rudder. The inverse yaw-mode time-constant ($1/T_y$) is the negative value of damping stability derivative (N_r). The effective time-delay (τ_ψ) accounts for phase distortion caused by unmodeled high-frequency dynamics. The numerical values for these parameters are obtained from the NAVFIT program (Sec. 3.3.2) using a fitting range of 0.1-3.0 rad/sec:

$$\begin{aligned} N_{\delta_r} &= 0.619 \text{ deg/sec}^2\text{/deg-rudder} \\ &= 5.45 \text{ deg/sec}^2\text{/in.-ped} \\ 1/T_y &= 0.102 \text{ rad/sec} \\ \tau_\psi &= 0.0210 \text{ sec} \end{aligned} \tag{4.2}$$

As shown in Fig. 4.13, this model fits the flight data well at mid- and high-frequencies, but exhibits noticeable discrepancies at low frequencies, where the simple first-order time-constant approximation is

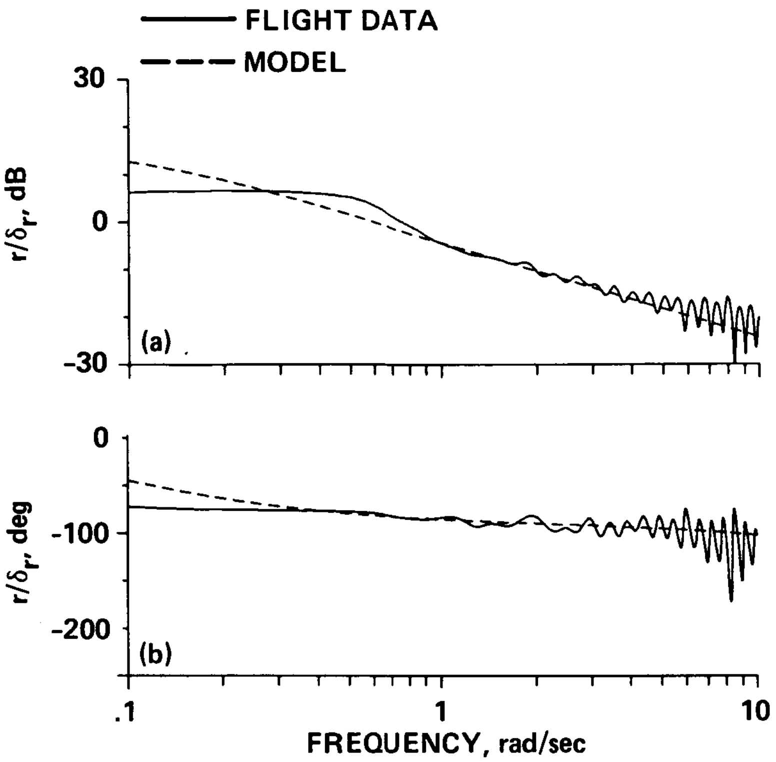

Fig. 4.13. Transfer-Function Model Identification for Yaw-Rate Response to Rudder (r/δ_r). (a) Magnitude; (b) Phase.

inadequate. The low-frequency mismatch is not very important, as is demonstrated in the model verification study (Sec. 4.3.1). The small effective time-delay (τ_ψ = 21 msec) indicates that the unmodeled high-frequency dynamics (e.g., rotor and actuators) are not very important in the identification range (0.1-3.0 rad/sec).

The standard roll-response transfer-function model for hovering vehicles is given in Ref. 41 as[†]

$$\frac{p(s)}{\delta_a(s)} = \frac{L_{\delta_a} s(1/T_{\phi_1})(1/T_{\phi_2})e^{-\tau_\phi s}}{(1/T_y)(1/T_r)[\zeta_r,\omega_r]} \tag{4.3}$$

where $p(s)/\delta_a(s)$ is the Laplace-transformed roll-rate response to aileron surface deflection, deg/sec/deg-aileron; L_{δ_a} is the aileron roll sensitivity; $1/T_{\phi_1}$, $1/T_{\phi_2}$ are first-order, numerator inverse time-constants; $1/T_r$, is the first-order roll mode inverse time-constant; ζ_r, ω_r are the second-order roll-mode damping and natural frequency, respectively; and τ_ϕ is the effective time-delay. The decoupled yaw mode $1/T_y$ is fixed at its previously identified [Eq. (4.2)] value ($1/T_y = 0.102$ rad/sec). The remaining numerator and denominator parameters are varied to obtain a good fit in the range of 0.2-9.0 rad/sec. The resulting roll transfer-function parameters are

---

[†] Shorthand notation: $[\zeta, \omega]$ implies $s^2 + 2\zeta\omega s + \omega^2$, ζ = damping ratio; ω = undamped natural frequency (rad/sec); and $(1/T)$ implies $s + (1/T)$, rad/sec.

$$
\begin{aligned}
L_{\delta_a} &= -3.71 \text{ deg/sec}^2\text{/deg-aileron} \\
&= 15.1 \text{ deg/sec}^2\text{/in.-}\delta_{Lat} \\
1/T_{\phi_1} &= -0.107 \text{ rad/sec} \\
1/T_{\phi_2} &= 0.412 \text{ rad/sec} \\
1/T_y &= 0.102 \text{ rad/sec} \\
1/T_r &= 1.23 \text{ rad/sec} \\
\zeta_r &= -0.418 \\
\omega_r &= 0.447 \text{ rad/sec} \\
\tau_\phi &= 0.0313 \text{ sec}
\end{aligned}
\tag{4.4}
$$

As shown in Fig. 4.14, the transfer-function model is generally a very good representation of the aircraft roll response. However, a close examination of the model-fit and flight data in the frequency-range near the dominant mode ($\omega \doteq 0.5$ rad/sec) shows the inability of the linear model to simultaneously match both the magnitude and phase responses. Based on the magnitude response alone, a somewhat more unstable (higher negative damping ratio) mode is indicated; but, based on the phase response alone, a slightly less unstable (smaller negative damping ratio) model is indicated. This inconsistency reflects the significant

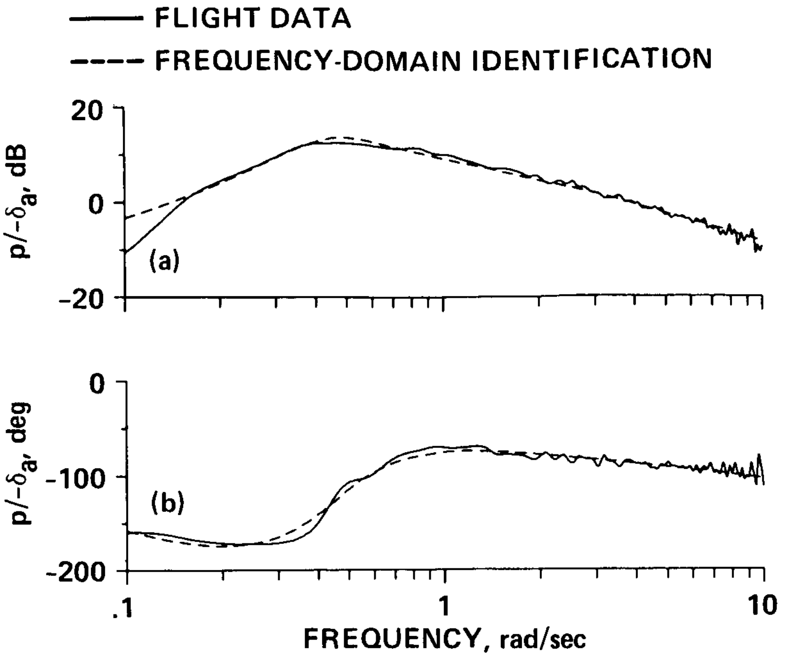

Fig. 4.14. Transfer-Function Model Identification for Roll-Rate Response to Ailerons ($p/-\delta_a$). (a) Magnitude; (b) Phase.

nonlinearities which are in this frequency range. The linear model of Eq. (4.4) is thus a compromise, and reflects the current relative weighting: 1 dB magnitude error: 7 deg phase error. Increasing the weighting of the phase errors resulted in a less unstable damping ratio (ζ_r), better phase matching, and poorer magnitude matching as expected. The current weighting was retained since it is consistent with practice in the handling-qualities community (Ref. 37), and as shown in Sec. 4.3 it leads to transfer-function models with good predictive capability. The capability to specify relative magnitude and phase error weighting is an advantage of the frequency-domain approach. Time-domain identification methods inherently weight the phase errors much greater than the magnitude errors, since small shifts in phase between the flight-data and the model-response generate large changes in the time-domain cost function (Ref. 22).

Some important conclusions can be drawn from the transfer-function model parameters of Eq. (4.4), and the location of the poles and zeros in the complex plane (Fig. 4.15). First, the open-loop roll response dynamics are dominated by a very unstable oscillation in hover, with an associated time-to-double amplitude of 3.7 sec. Reference 43 specifies an unstable damping ratio limit of $\zeta = -0.22$, for Level I handling qualities, which is shown on Fig. 4.15. The fact that the XV-15 roll mode [-0.418, 0.447] lies beyond this boundary suggests that the SCAS-off vehicle has Level II handling qualities (at best). This is corroborated by the SCAS-off handling-qualities evaluation discussed in Sec. 2.1.3. The maximum roll acceleration capability of 1.27 rad/sec^2 (based on the lateral-stick sensitivity and maximum deflection) provides a sufficient margin for SCAS-off roll-attitude control (AGARD specification, Ref. 43).

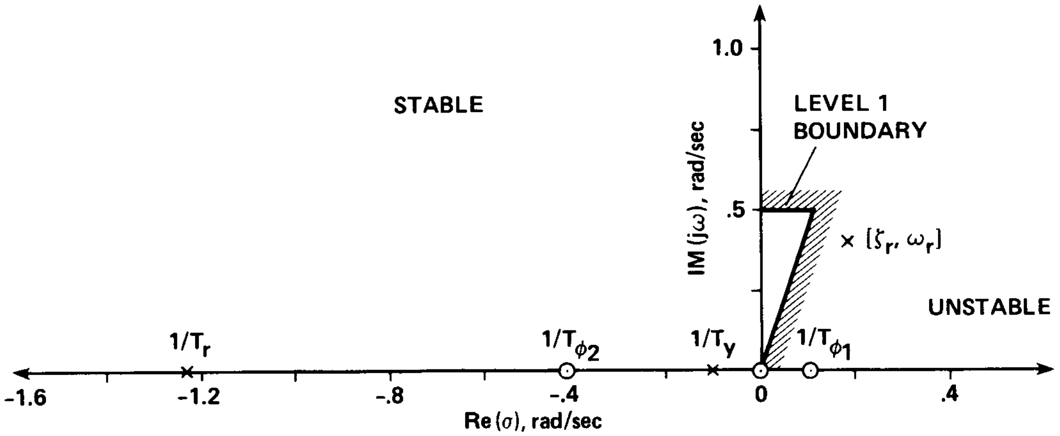

Fig. 4.15. Locations of Roll-Response Transfer-Function Parameters in the s-Plane.

The second important conclusion is that the pole-zero combination $(1/T_{\phi_1})/(1/T_y)$ is at very low frequency and nearly cancels out (Fig. 4.15). This reveals that yaw coupling does not noticeably affect the roll-response characteristics, again a common assumption for hovering aircraft (Ref. 41). Third, the low-frequency numerator factor $(1/T_{\phi_1})$ associated with coupled lateral translation/yaw damping is also the limiting location of the dominant lateral translation mode when the inner attitude is tightly pilot-regulated (Ref. 44). The fact that this parameter is marginally unstable (time-to-double amplitude = 6.8 sec) suggests that lateral station-keeping will be difficult. This is typical of unaugmented helicopters (Ref. 45) and is corroborated by the handling-qualities evaluation (Sec. 2.1.3). Fourth, the effective time-delay (τ_ϕ) is small, again suggesting that unmodeled high-frequency dynamics are not significant in the frequency range of identification (0.2-9.0 rad/sec).

4.1.2 Lateral/Directional Coupling

As discussed previously, the dominant source of interaxis coupling for the hovering flight condition is yaw-rate response to aileron inputs. Identification of this coupling characteristic is important for assessing the pilot's work load in open-loop lateral station-keeping tasks.

Clearly the pilot and SCAS feedbacks to the pedals will have a first-order effect on the identification of the open-loop yaw-rate response to aileron. Therefore, the application of the two-input/single-output analysis method is essential. This case will be presented in detail, since it is an excellent example of how coupled bare-airframe characteristics can be extracted from a multi-loop system.

The yaw-rate response to the lateral-stick sweeps of Fig. 4.1 is shown in Fig. 4.16. Excursions generally do not exceed ±5 deg/sec. This is due to the combined effect of the pilot and stability-augmentation stabilization of the yaw degree-of-freedom during the lateral-stick sweep. In essence, the pilot is attempting to eliminate the yaw-rate response to aileron--that which is now being identified.

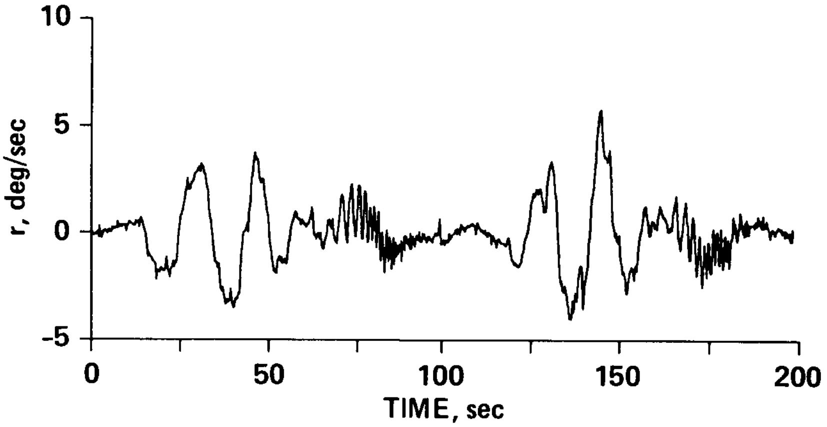

Fig. 4.16. Yaw-Rate Response (r) during Lateral-Stick Frequency Sweeps.

The autospectrum for aileron surface inputs (Fig. 4.17) is very flat across the entire frequency spectrum, as desired. The aileron

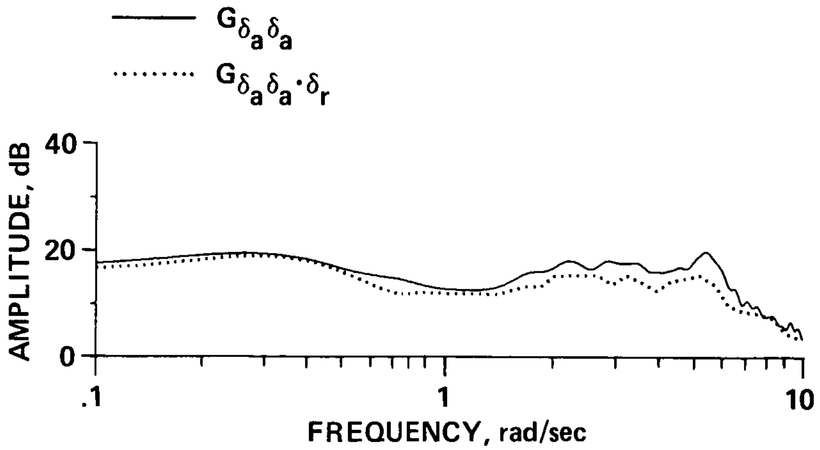

Fig. 4.17. Aileron Surface Input Autospectrum.

autospectrum $G_{\delta_a \delta_a}$ (Fig. 4.17) is not the same as that in Fig. 4.4 (although the time-history data are identical) because the optimum window length (Sec. 3.2.1) was found to be longer for the single-axis identification of p/δ_a than for the coupled-system identification. In this case, the output is the yaw-rate signal, which has an autospectrum that is not very flat (Fig. 4.18). The cross-spectrum between aileron input and the yaw-rate response (Fig. 4.19) is relatively constant in the high-frequency range, and peaks at low frequency ($\omega \doteq 0.3$ rad/sec), as does the output autospectrum (Fig. 4.18).

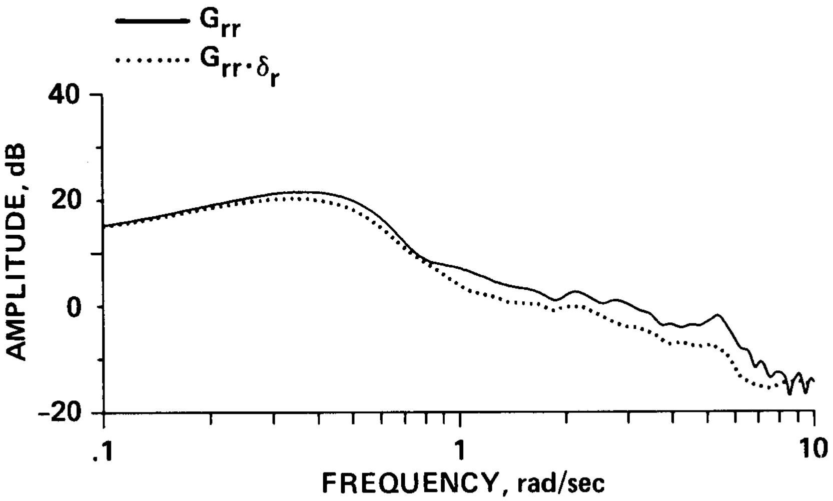

Fig. 4.18. Yaw-Rate Output Autospectrum.

The frequency response of aileron to yaw-rate, with rudder inputs present ($r/\delta_a{:}\delta_r$) is shown in Fig. 4.20. The frequency response is relatively flat in the mid-frequency range, indicating a fixed relation between yaw-rate and aileron when the (pilot and SCAS) yaw-axis stabilization is active. The ordinary coherence between yaw-rate and aileron, shown in Fig. 4.21, has a very low value over most of the frequency range. This indicates the presence of other inputs which significantly

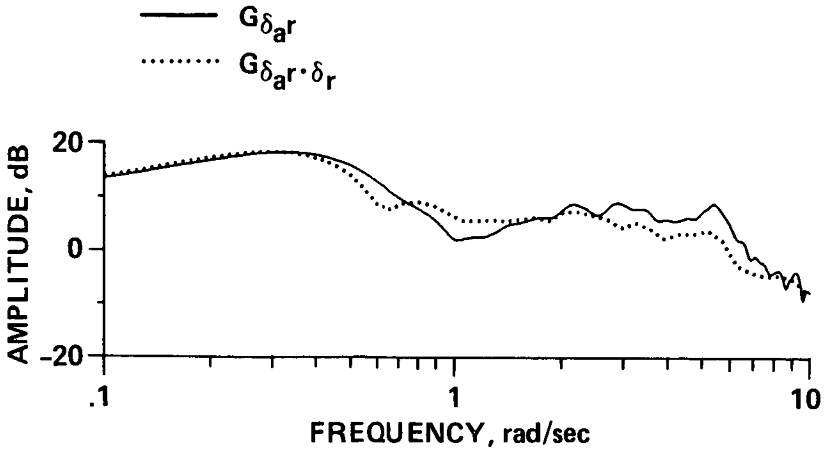

Fig. 4.19. Magnitude of Cross-Spectrum between Aileron Surface Inputs and Yaw-Rate Response.

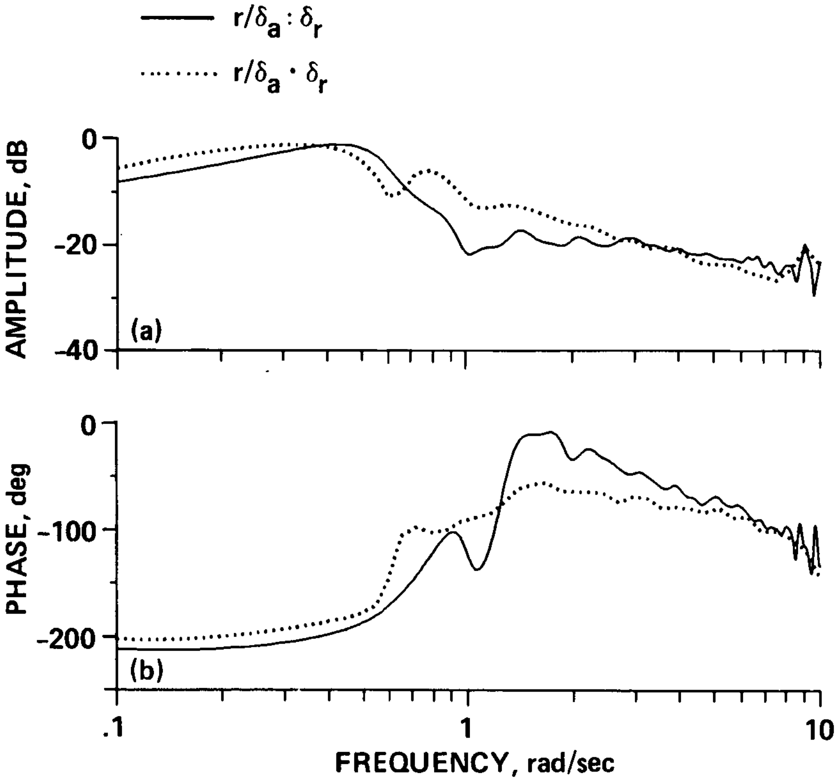

Fig. 4.20. Yaw-Rate Response to Ailerons. (a) Magnitude; (b) Phase.

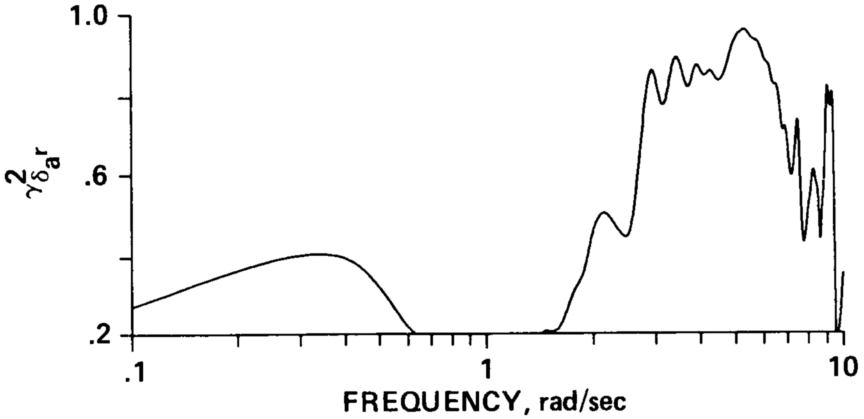

Fig. 4.21. Coherence Function for Yaw-Rate Response to Aileron Inputs ($\gamma^2_{\delta_a r}$).

contribute to the observed yaw-rate output signal; clearly, these are the rudder inputs, which are being supplied by the pilot and the yaw-stabilization system.

Rudder surface inputs during the lateral frequency-sweep are shown in Fig. 4.22. The deflections are generally within ±5 deg, with most of the low-frequency activity coming from pilot inputs. The coherence

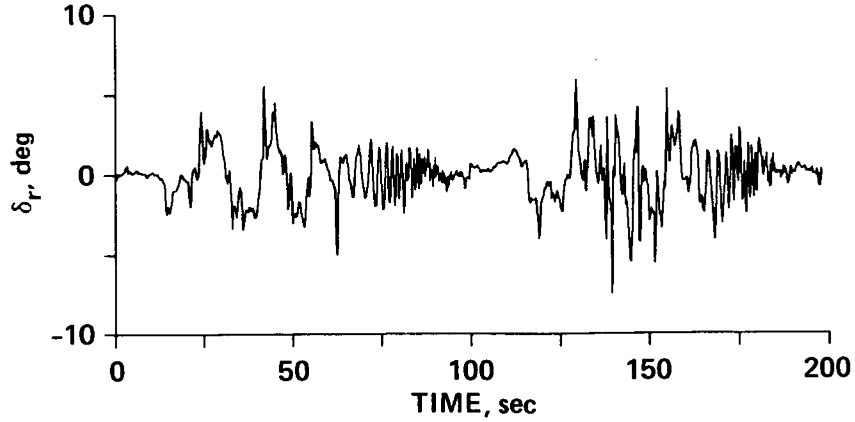

Fig. 4.22. Rudder Surface Deflections (δ_r) during the Lateral-Stick Frequency Sweeps.

function for the cross-correlation between rudder and aileron surface inputs presented in Fig. 4.23 is very low over most of the frequency

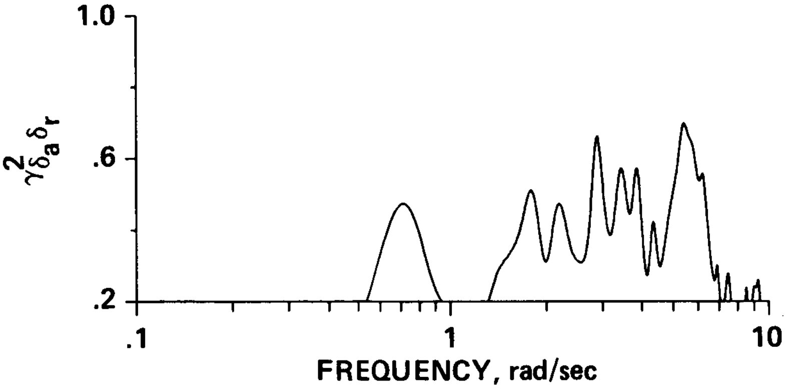

Fig. 4.23. Coherence Function for Cross-Correlation between Aileron and Rudder Surface Inputs ($\gamma^2_{\delta_a \delta_r}$).

range. This shows that the inputs are not fully correlated, the key requirement for two-input/single-output identification (Sec. 3.2.5). For other flight conditions in which similar analyses were conducted, the cross-coherence between rudder and aileron inputs was generally much greater because pilot-stabilization requirements in the secondary axis were less severe. This increased cross-coherence caused an overall degradation in the cross-coupling identification for the forward-flight cases. Therefore, when possible, the frequency-sweeps should be conducted without engaging the stability-augmentation systems in the secondary degrees-of-freedom.

The conditioned aileron input autospectrum ($G_{\delta_a \delta_a \cdot \delta_r}$), that is, with the effect of rudder inputs eliminated, is presented in Fig. 4.17. The comparison of results in this figure shows that the input autospectrum is not substantially changed. This is because the cross-coherence between inputs is small. A similar characteristic is apparent for the conditioned output autospectrum ($G_{rr\cdot\delta_r}$) shown in Fig. 4.18. The conditioned cross-spectrum between aileron and yaw-rate ($G_{\delta_a r\cdot\delta_r}$) presented in Fig. 4.19 is generally more flat than before, a result of the elimination of the yaw-rate feedback effect.

The conditioned frequency-response of aileron to yaw-rate ($r/\delta_a\cdot\delta_r$) is shown in Fig. 4.20. Notice that the shape of the magnitude and phase responses is significantly different than it was before the rudder inputs were taken into account. The response from 1.0-10.0 rad/sec now exhibits the familiar -20 dB/decade roll-off. This suggests that the interaxis coupling is dominated by the aileron-to-yawing moment control-coupling derivative (N_{δ_a}), as expected. The low-frequency dynamics are unstable, as seen earlier in the roll response.

The partial coherence function $\gamma^2_{\delta_a r\cdot\delta_r}$ of Fig. 4.24 shows that satisfactory identification of the coupling dynamics has been achieved

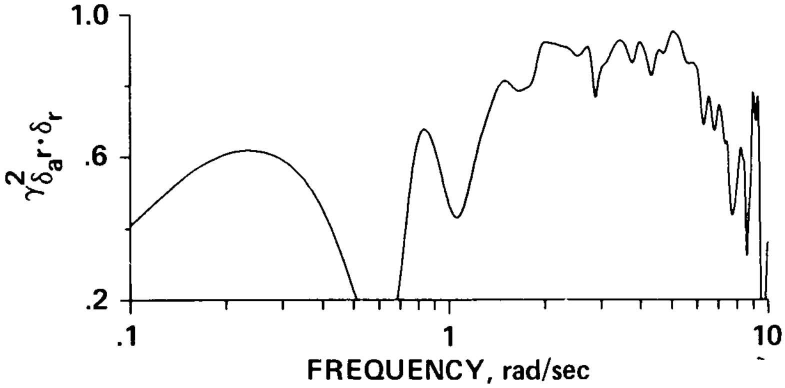

Fig. 4.24. Partial Coherence Function for Yaw-Rate Response to Aileron Inputs ($\gamma^2_{\delta_a r\cdot\delta_r}$).

in the frequency ranges of 0.1-0.4 rad/sec and 0.75-7.0 rad/sec. The multiple coherence plot $\gamma^2_{\delta_a\delta_r:r}$ of Fig. 4.25 indicates that the combined linear effects of aileron and rudder account for most of the

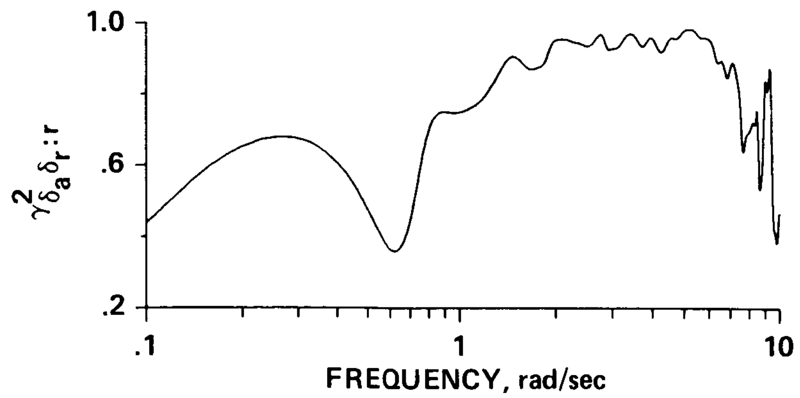

Fig. 4.25. Multiple Coherence Function for Yaw-Rate Response to Combined Aileron and Rudder Surface Inputs ($\gamma^2_{\delta_a\delta_r:r}$).

yaw-rate response at high frequencies with a drop-off at lower frequencies because of nonlinearities and turbulence, as was seen previously in the single-input, roll-response analysis.

The following transfer-function model adequately characterizes the aileron-to-yaw rate coupling:

$$\frac{r(s)}{\delta_a(s)} = \frac{N_{\delta_a}(1/T_\psi)[\zeta_\psi,\omega_\psi]e^{-\tau_{\psi_2}s}}{(1/T_y)(1/T_r)[\zeta_r,\omega_r]} \qquad (4.5)$$

where $r(s)/\delta_a(s)$ is the Laplace-transformed yaw-rate response to aileron surface deflection, deg/sec/deg-aileron; N_{δ_a} is the aileron yaw sensitivity; $1/T_\psi$ is the first-order numerator inverse time-constant; ζ_ψ and ω_ψ are the second-order numerator damping and natural frequency, respectively; and τ_{ψ_2} is the effective time-delay. The denominator factors are the previously identified lateral modes [Eq. (4.4)]. These denominator factors are held constant, and the remaining parameters are iteratively varied using NAVFIT to fit the data in the frequency range 0.1-7.0 rad/sec. The resulting transfer-function parameters are

$$
\begin{aligned}
N_{\delta_a} &= 0.344 \text{ deg/sec}^2\text{/deg-aileron} \\
&= -1.40 \text{ deg/s}^2\text{/in.-}\delta_{Lat} \\
1/T_{\psi} &= -0.345 \text{ rad/sec} \\
\zeta_{\psi} &= 0.868 \\
\omega_{\psi} &= 0.487 \text{ rad/sec} \\
1/T_y &= 0.102 \text{ rad/sec} \\
1/T_r &= 1.23 \text{ rad/sec} \\
\zeta_r &= -0.418 \\
\omega_r &= 0.447 \text{ rad/sec} \\
\tau_{\psi_2} &= 0.00900 \text{ sec}
\end{aligned}
\qquad (4.6)
$$

The yaw-rate responses to both aileron and rudder are dominated by the "K/s characteristic" in the pilot's operating (crossover) frequency region for attitude control [generally taken as 1.0-3.0 rad/sec (Ref. 41)]. Therefore, the pilot cross-feed (G_{CF}) that is needed to maintain a fixed heading during lateral manuevering is approximately a constant:

$$G_{CF} \doteq \frac{N_{\delta_a}}{N_{\delta_r}} = 0.556 \text{ deg-rud/deg-ail} = 0.489 \text{ \%-ped/\%-lat} \qquad (4.7)$$

This shows that pedal inputs must be about 50% of the lateral stick inputs to maintain a constant heading in the piloted crossover frequency region. This level of coupling is quite severe, and probably contributes to the poor SCAS-off handling-qualities in lateral translation tasks (Sec. 2.1.3).

The comparison between the transfer-function model fit and the flight-test results for this case is shown in Fig. 4.26. The magnitude response correlates well with somewhat poorer agreement for the phase response. However, the nature of the coupling characteristics is well represented.

In the simulated lateral-stick sweeps, pilot regulation of yaw excursions was not very aggressive. Therefore, the rudder inputs were dominated by the SCAS, causing a strong correlation between the rudder and aileron responses. This precluded the application of the two-input method. Instead, the flight-test results are compared in Fig. 4.26 with the real-time mathematical model (numerical) perturbation transfer-function. As expected, the high-frequency correlation is excellent, since it depends only on the cross-coupling moment derivative N_{δ_a}. The agreement at low frequency is much less satisfactory because nonlinear yaw and roll dynamics are not well represented by the small perturbation transfer-function (Sec. 4.1.1).

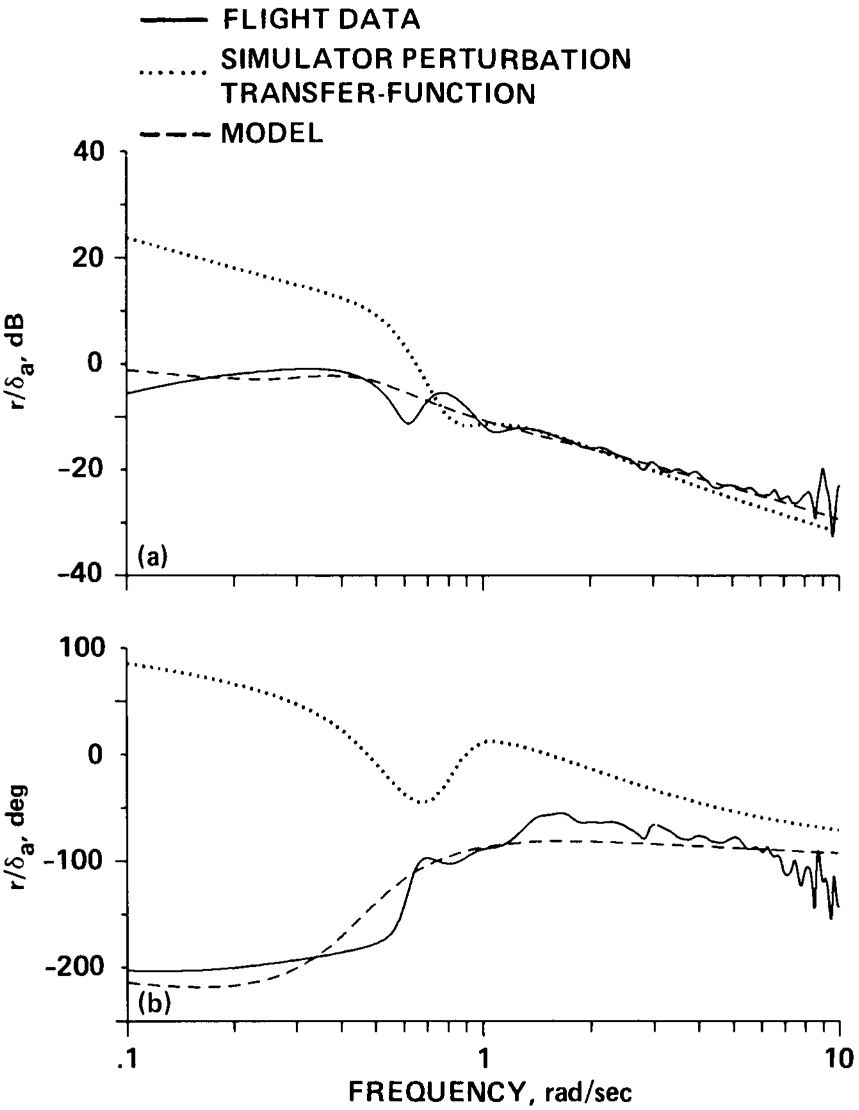

Fig. 4.26. Comparison of Flight-Test and Simulator Results for Yaw-Rate Response to Aileron (r/δ_a). (a) Magnitude; (b) Phase.

4.2 Longitudinal Dynamics

Power lever inputs produce essentially decoupled first-order vertical-acceleration (heave) responses. So, these can be considered independently from the pitch responses. The vertical acceleration response to power-lever inputs (a_z/δ_c) is shown in Fig. 4.27. For low-frequency inputs, the first-order heave mode dominates the response,

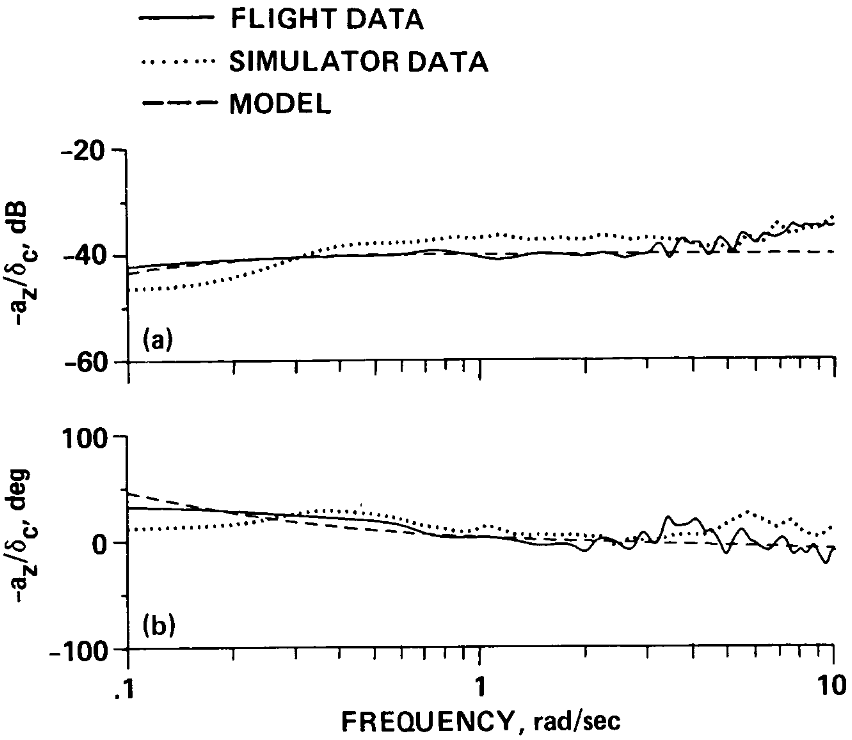

Fig. 4.27. Vertical-Acceleration Response to Power Lever ($-a_z/\delta_c$). (a) Magnitude; (b) Phase.

causing the phase rise seen in Fig. 4.27b. The relatively slight change in the magnitude response (Fig. 4.27a) suggests that this mode is at a very low frequency, as is verified later. In the frequency range of 1.0-10.0 rad/sec, the phase curve is nearly constant, so the aircraft vertical-acceleration response to power-lever inputs is instantaneous, and the high-frequency engine-governor dynamics are not significant. The coherence function is shown in Fig. 4.28, and indicates an excellent identification of the vertical response characteristics in the frequency range of 0.1-3.0 rad/sec.

The simulation-response characteristics are also shown in Figs. 4.27 and 4.28. In general, the agreement is good in the form

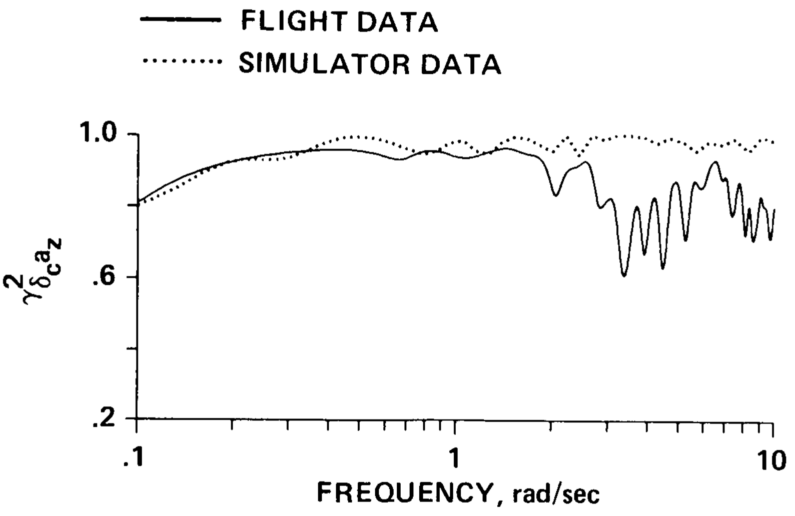

Fig. 4.28. Coherence Function for Vertical-Acceleration Response Identification ($\gamma^2_{\delta_c a_z}$).

of the amplitude and phase characteristics for frequencies $\omega > 0.3$ rad/sec, suggesting that the modeling of initial thrust response to collective inputs, and governor dynamics, is satisfactory. The constant amplitude error (vertical shift) may be due to a mismatch in the assumed vehicle mass or rotor lift curve slope. The low-frequency agreement is not as good, which appears to be due to an underestimate of the heave-mode time constant by the simulation.

The vertical-velocity response ($w = a_z/s$) to collective is identical in form to the yaw-rate response to rudder presented earlier. In fact, these two decoupled degrees-of-freedom are directly analogous. Typically, they both have very long time-constants for tilt-rotor-class VTOL vehicles, in contrast to single-rotor helicopters, so that their response is basically an acceleration; the control sensitivity is a function of the applied control force (or moment) normalized by the respective mass characteristic. A first-order model fit to the vertical-acceleration response in the frequency range 0.1-3.0 rad/sec yields

$$\frac{a_z(s)}{\delta_c(s)} = \frac{-0.00980s\ e^{-0.00740s}}{(s + 0.105)}\ g/\% \qquad (4.8)$$

where the heave-mode time-constant has about the same value as the yaw-mode time-constant presented earlier, and the time delay is again small. The control sensitivity (-0.0098 g/%) is equivalent to -0.1 g/in. of power lever; this is adequate, based on the data of Ref. 43. The very low value of the flight-extracted inverse time-constant ($1/T_h$ = 0.105 rad/sec) relative to typical hovering helicopters is due to the high disc-loading of the tilt-rotor configuration.

Although the frequency-sweeps in roll were more difficult to perform than those in pitch, the identification of the pitch results proved to be the most difficult. Stick inputs tended to be very small at low frequency, which resulted in poor uncorrelated input power. Of the three longitudinal frequency-sweeps which were conducted (and used in the original analysis of Ref. 18), only one run subsequently proved to be of satisfactory quality (based on input autospectrum and coherence) for the pitch-response identification in the mid- and low-frequency range. In the high frequency range (ω > 2 rad/sec), all sweeps are of good spectral quality, so concatenation of the time-histories is useful to obtain minimum variance results there. However, to achieve good identification over the entire frequency range only the single frequency-sweep is used. The possibility of combining spectral results which are optimized for particular frequency-ranges has not been fully investigated, but may enhance the overall quality of the identification results.

The elevator to pitch-rate frequency response is shown in Fig. 4.29. As before in the roll axis, the response peak is due to the dominant pitch modes which are at low frequency. For frequencies $\omega > 2$ rad/sec, the magnitude response rolls off with the K/s rigid-body characteristic, as expected. The phase rise near the low-frequency response peak reflects an unstable pitch-mode associated with the speed/attitude divergence, as in the roll case. At high-frequency, the pitch-rate and elevator traces are just over 90 deg out of phase because of the rigid-body response and the small high-frequency lags.

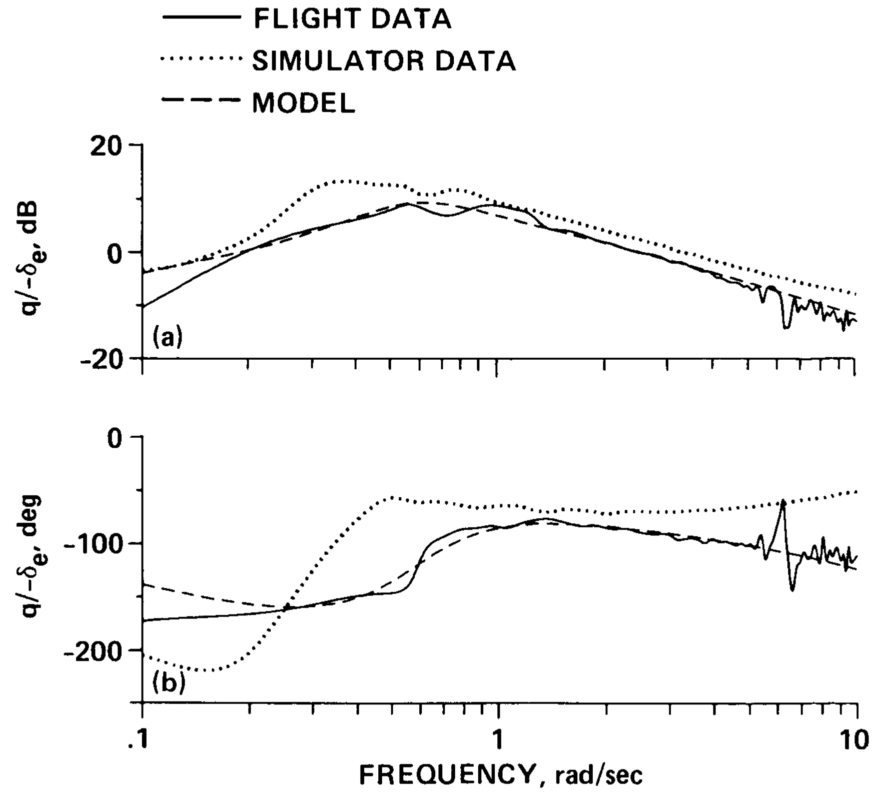

Fig. 4.29. Pitch-Rate Response to Elevator ($q/-\delta_e$).
(a) Magnitude; (b) Phase.

The coherence function shown in Fig. 4.30 indicates a strong identification in the frequency range 0.2-6.0 rad/sec. The drop in coherence between 0.5-1.0 rad/sec suggests that nonlinearities are important in low-frequency dynamics, as would be expected from the similar roll-response behavior.

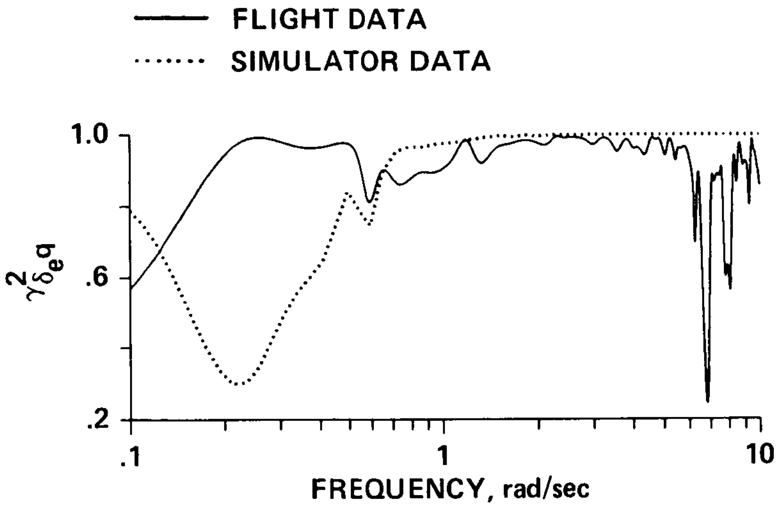

Fig. 4.30. Coherence Function for Pitch-Rate Response Identification ($\gamma^2_{\delta_e q}$).

The simulation pitch-response characteristics are also shown in Figs. 4.29 and 4.30. The parallel (vertical) shift in the magnitude plots at high frequency suggests differences in the high-frequency gain parameter, M_{δ_e}. As in the yaw-case, the discrepancy (about 25%) is probably a result of ballast in the tail of the aircraft, which was not included in the simulation model. Considerable differences between the simulation and flight-extracted responses are apparent in the frequency range of 0.3-0.8 rad/sec. The simulation model appears to underestimate both the frequency and the unstable damping ratio of this mode. Comparisons of time-domain identification results (Ref. 22) with the nonreal-time simulation indicates that "speed-stability derivative" M_u is underestimated in the simulator by about 70% [$(M_u)_{FLIGHT} = 0.00622$ versus $(M_u)_{SIMULATION} = 0.00200$ rad/sec^2/ft/sec] which would contribute to the observed frequency and damping discrepancies (Ref. 42). A probable source of this error in the M_u derivative is the rotor longitudinal flapping angle predictions based on the uniform lateral inflow approximation, as was also indicated in the yaw-rate response (Sec. 4.1.1).

The transfer-function model for pitch-rate response to elevator has the same form as the roll-response model of Eq. (4.3):

$$\frac{q(s)}{\delta_e(s)} = \frac{M_{\delta_e} s(1/T_{\theta_1})(1/T_{\theta_2})e^{-\tau_\theta s}}{(1/T_h)(1/T_p)[\zeta_p,\omega_p]} \tag{4.9}$$

where $q(s)/\delta_e(s)$ is the Laplace-transformed pitch-rate response to elevator surface deflection, deg/sec/deg-elevator; M_{δ_e} is the elevator pitch sensitivity; $1/T_{\theta_1}$, $1/T_{\theta_2}$ are first-order numerator inverse time-constants; $1/T_p$ is first-order pitch-mode inverse time-constant; ζ_p and ω_p are the second-order pitch-mode damping and natural frequency, respectively; and τ_θ is the effective time-delay. As before, the decoupled mode, (in this case $1/T_h$), is fixed at its previously identified value ($1/T_h = 0.105$ rad/sec). The remaining numerator and denominator parameters are varied to obtain a good fit in the frequency range 0.2-5.0 rad/sec:

$$M_{\delta_e} = -2.66 \text{ deg/sec}^2\text{/deg-elevator}$$

$$= -13.2 \text{ deg/sec}^2\text{/in.-}\delta_{Lon}$$

$$1/T_{\theta_1} = -0.271 \text{ rad/sec}$$

$$1/T_{\theta_2} = 0.508 \text{ rad/sec}$$

$$1/T_h = 0.105 \text{ rad/sec}$$

$$1/T_p = 1.32 \text{ rad/sec} \qquad (4.10)$$

$$\zeta_p = -0.463$$

$$\omega_p = 0.579 \text{ rad/sec}$$

$$\tau_\theta = 0.0656 \text{ sec}$$

A comparison of the lower-order model with the flight-test results is shown in Fig. 4.29. Overall, the model is a good approximation to the flight data in the fitting range. However, as in the roll case, the presence of nonlinearities in the low-frequency unstable dynamics precludes an entirely representative fit in both magnitude and phase near the response peak.

Once again, some important conclusions can be drawn from the lower-order transfer-function model. First, the open-loop (bare-airframe) configuration is very unstable in the pitch axis, with nearly the same damping ratio and natural frequency as in the roll axis. As before, poor SCAS-off handling-qualities are indicated and have been reported in piloted evaluations (Sec. 2.1.3). Second, the pole-zero pair associated with heave motions $(1/T_{\theta_2})/(1/T_h)$ is widely separated, implying that significant heave-pitch coupling results from pitch-control inputs. This separated pole-zero pair precludes the use of the standard third-order, pitch transfer-function model for hover. Third, the numerator factor $(1/T_{\theta_1})$ associated with the translational mode dynamics for constrained attitude control (Ref. 44), is very unstable (time-to-double amplitude = 2.6 sec), and probably contributes to the poor translational-flight handling-qualities (Sec. 2.1.3). Fourth, the effective time-delay (τ_θ) is very small, as it is in the roll axis, suggesting that unmodeled high-frequency dynamics are not significant in the frequency range of identification (0.2-5.0 rad/sec).

4.3 Verification of Open-Loop Transfer-Function Models for Hover

Verification of all identified open-loop transfer functions should be completed with open-loop flight-test data. However, the duration and size of the verification test-inputs is severely restricted by the inherent stability and response characteristics for each axis and flight condition. The decoupled stable first-order nature of the open-loop yaw and heave responses allows large and very long duration step-inputs (about 10 sec) to be executed. Then, the modes with frequencies of $\omega > 0.1$ rad/sec contribute at least one time-constant of their inherent response to the overall behavior, which checks the yaw and heave transfer-functions [Eq. (4.2) and (4.8), respectively] over the entire identified frequency range. However, as previously discussed, the open-loop pitch and roll dynamics are dominated by strong instabilities, with time-to-double amplitudes of about 3 sec. This severely restricts the allowable size and duration of the verification test inputs in these axes.

To reduce the level of coupled divergence, verification of the open-loop pitch response is completed with the roll and yaw SCAS axes engaged. Similarly, verification of the open-loop roll response is completed with the pitch and yaw SCAS axes engaged. Even so, maximum achieveable step-input durations are 1-2 sec, which allows the dominant modes with frequencies of about $\omega \doteq 0.5$ rad/sec to experience only one time constant. Therefore, the verification step-inputs do not give a complete test of model fidelity at very low frequencies. However, ensuring model accuracy at mid- and high-frequency is of principal importance for handling-qualities (and control) applications since the pilot is mostly concerned with the response in the first few seconds. SCAS-on step responses are often useful for verification when quiescent initial test conditions cannot be achieved in the open-loop configuration.

4.3.1 Roll Response to Aileron Inputs

The (filtered) roll-rate response of the aircraft to a step aileron input with the roll SCAS disengaged is shown in Fig. 4.31. The input is held for 2 sec and the peak response is 10 deg/sec, which is roughly the same as was achieved during the lateral frequency-sweeps (Fig. 4.5). When the transfer-function model of Eq. (4.4) is driven with the same (filtered) input flight data, the response co-plotted in the dashed curve of Fig. 4.31 is obtained. The model and flight data responses

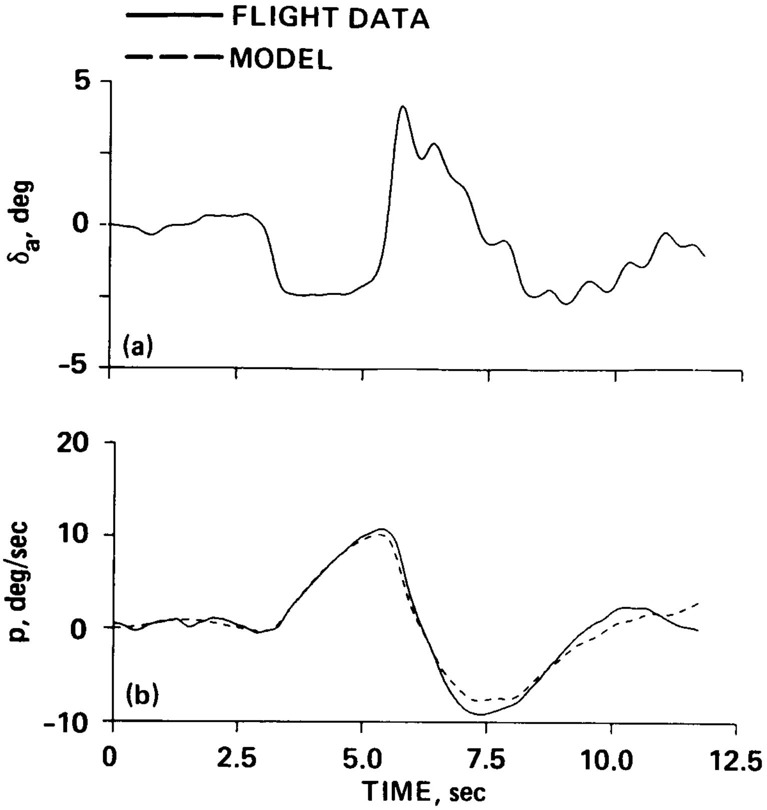

Fig. 4.31. Roll-Response Model Verification Using SCAS-off Flight Data. (a) Aileron Input; (b) Roll-Rate.

generally compare very well, although there is a slight underestimation of the peak roll rate, probably a result of nonlinear effects.

4.3.2 Yaw Response to Rudder Inputs

The yaw-rate responses of the aircraft and model Eq. (4.2) to an open-loop step-rudder input in hover are shown in Fig. 4.32. The control deflection represents about 40% of the maximum control power, a fairly large amplitude input. The maximum yaw-rate response is about 35 deg/sec, which is 40% greater than the peak values obtained in the frequency sweeps. The model and flight responses generally compare very well over the entire run--even for this fairly large input amplitude

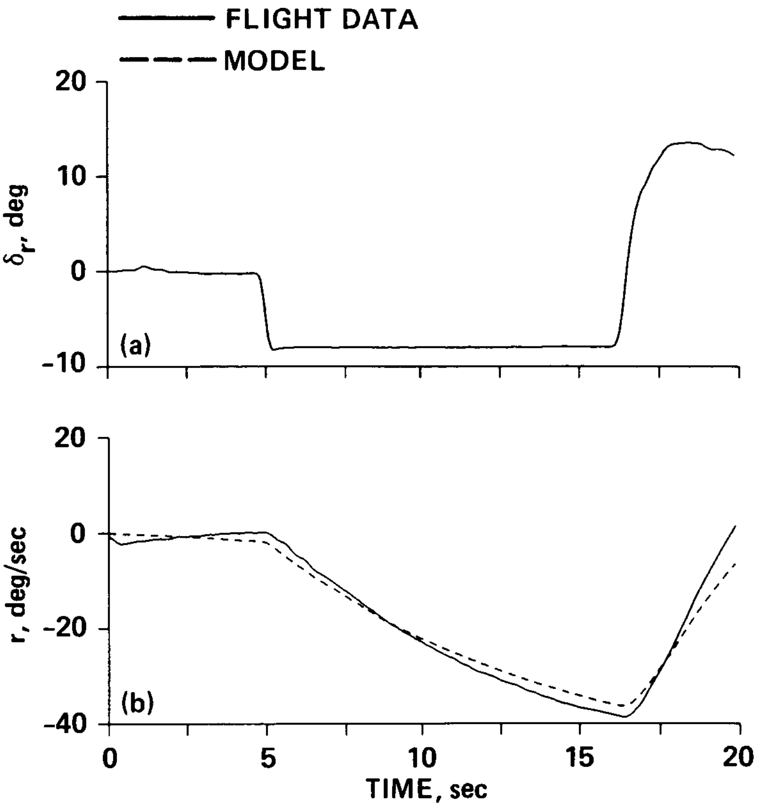

Fig. 4.32. Yaw-Response Model Verification Using SCAS-off Flight Data. (a) Rudder Input; (b) Yaw-Rate.

case. The small discrepancies are probably associated with the mid-frequency mismatch between the flight-extracted frequency response and transfer-function fit (Fig. 4.13), or large amplitude nonlinear effects.

4.3.3 Yaw Response to Aileron Inputs

The verification of the identified model for yaw-rate response to aileron [Eq. (4.6)] is shown in Fig. 4.32. The SCAS configuration is roll, SCAS-off; and yaw, SCAS-on. Therefore, some rudder activity is also present (Fig. 4.33b). The roll-rate match is very good (Fig. 4.33c) as was seen in the previous comparison (Fig. 4.31). The observed yaw-rate (Fig. 4.33d) is composed of responses to rudder and

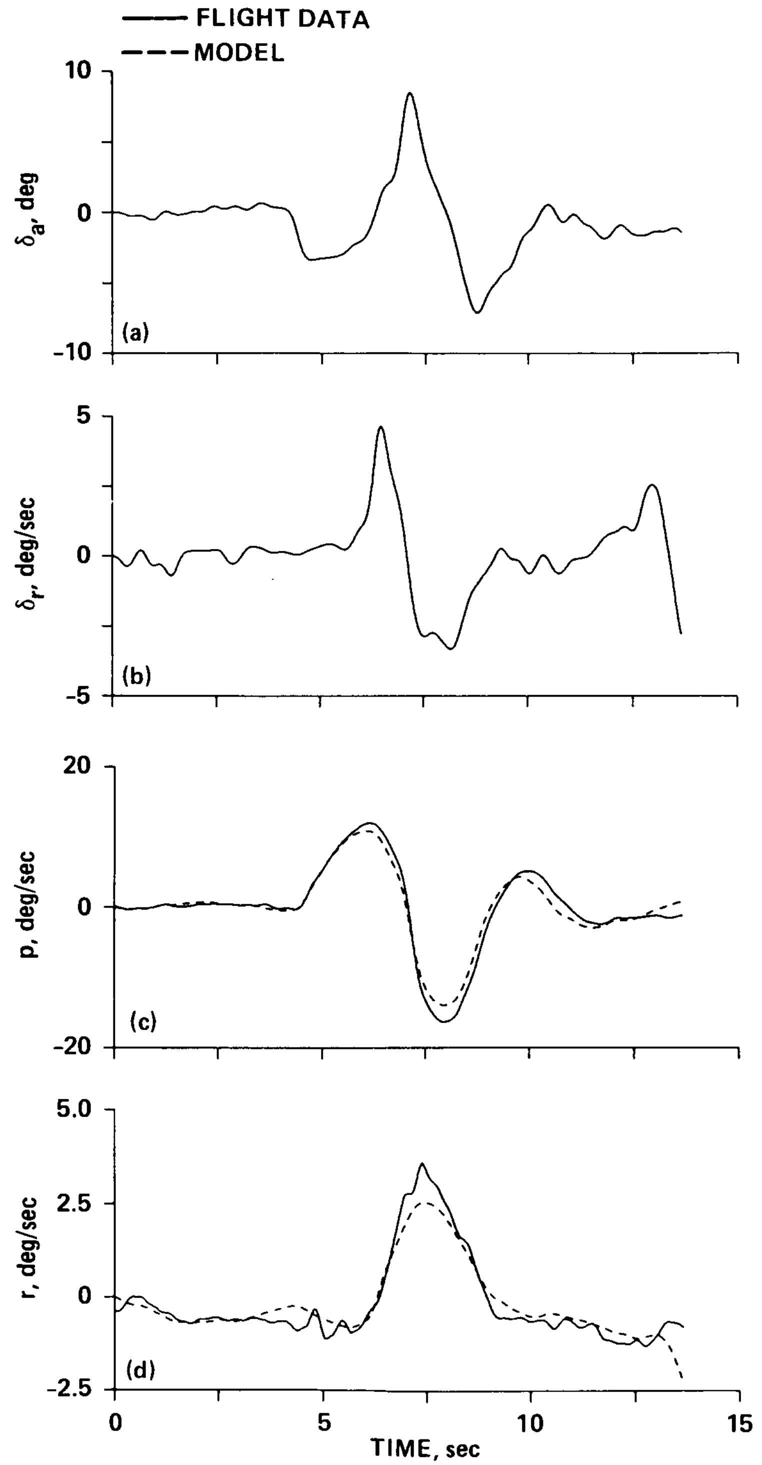

Fig. 4.33. Lateral-Directional Model Verification (Roll SCAS-off, Yaw SCAS-on). (a) Aileron Input; (b) Rudder Input; (c) Roll-Rate; (d) Yaw-Rate.

aileron inputs in about equal proportions. The total yaw-rate response has the proper form although the peak is underestimated; this is probably a result of nonlinearities in the coupled response characteristics (or a gust), as well as the slight underestimation in the yaw-rate response to rudder (Fig. 4.32).

4.3.4 Vertical Acceleration Response to Collective

The verification data for the step inputs in the collective axes are very noisy. Even so, the correlation of the model and flight data (Fig. 4.34) indicates that a proper identification has been achieved. The comparison is better at the beginning of the run where the inputs are smooth as compared to the end of the run where the inputs are more

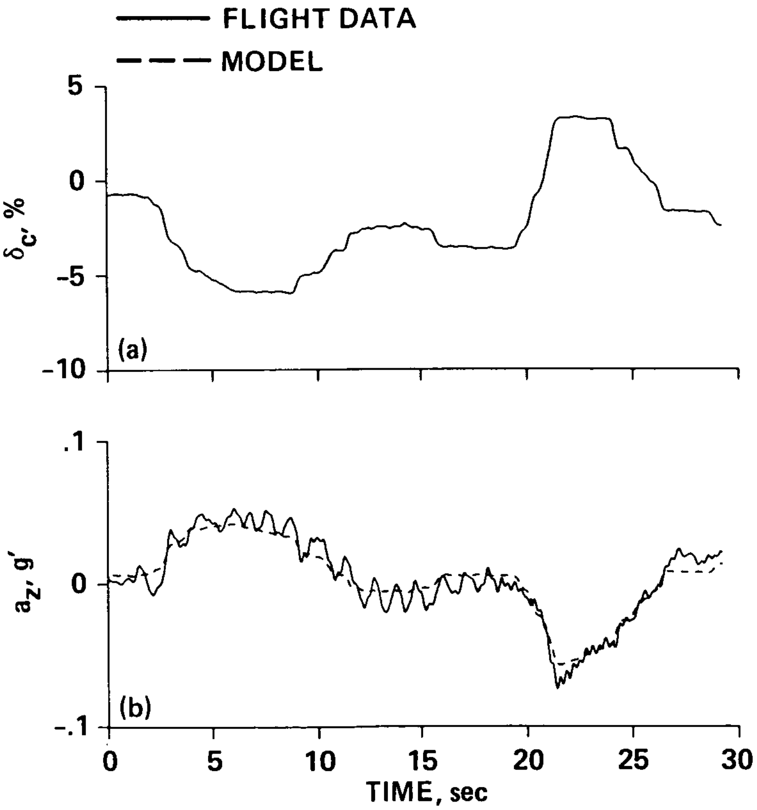

Fig. 4.34. Vertical-Acceleration Response Model Verification. (a) Power Lever Input; (b) Vertical Acceleration.

sharp. This is because the sharp change in collective (rotor thrust) excites the rotor inflow dynamics which are not included in the simple first-order model (Ref. 6).

4.3.5 Pitch-Rate Response to Elevator

The aircraft and model responses to a 2-sec step-input in elevator with the pitch SCAS disengaged are shown in Figs. 4.35. The relatively

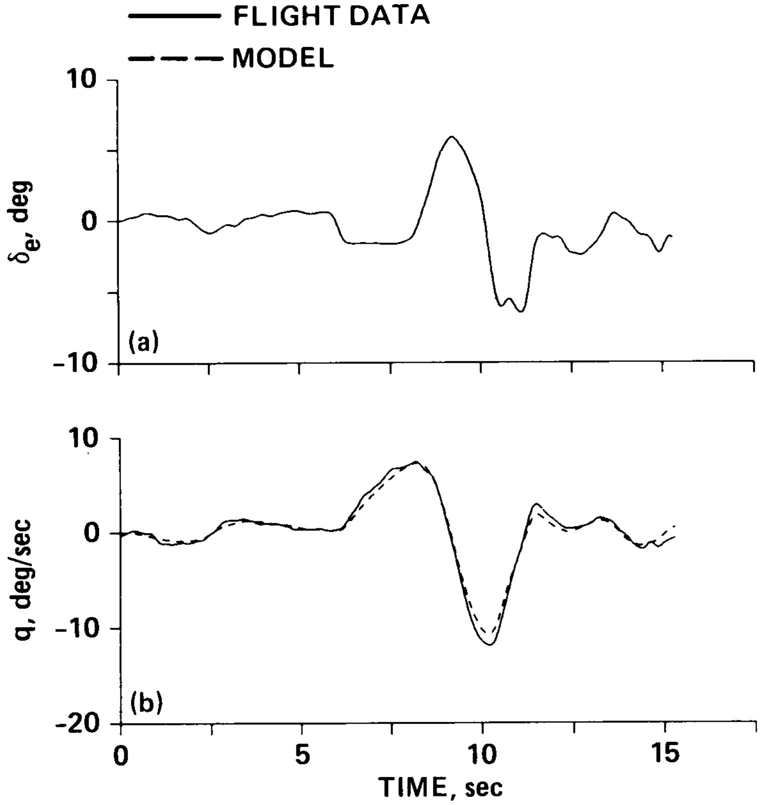

Fig. 4.35. Pitch-Response Model Verification Using SCAS-off Flight Data. (a) Elevator Input; (b) Pitch-Rate.

unsteady initial conditions cause the shift between the flight data and transfer-function models at the beginning of the run (t = 6-8 sec), but the comparison improves considerably during the large amplitude recovery phase (t = 8-15 sec). Somewhat better initial conditions are achieved with the pitch-SCAS engaged. The elevator surface-deflection response to a step input of longitudinal stick is a doublet, as seen in Fig. 4.36a. As expected from the control system configuration (Chap. 2), a steady pitch-rate is achieved within 0.5 sec of the longitudinal stick input. The model prediction is seen to be very good for the input and recovery (t = 9-13 sec).

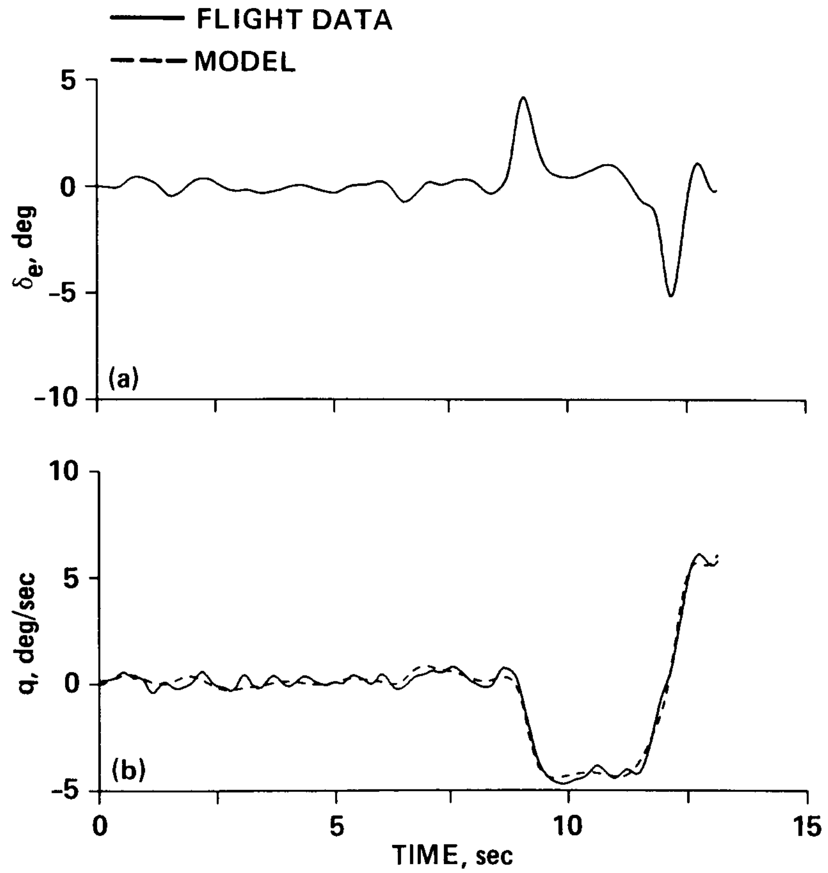

Fig. 4.36. Pitch-Response Model Verification Using SCAS-on Flight Data. (a) Elevator Input; (b) Pitch-Rate.

The verification results confirm the following:

1. The hover dynamics are essentially linear.

2. Mismatches between the extracted frequency-responses and transfer-function model fits are not significant, except perhaps in the yaw-rate response to rudder.

3. The derived transfer-function models are not overtuned or over-parameterized.

4. The unbiased open-loop vehicle response has been identified from the closed-loop flight data.

The derived transfer-function models for hover are summarized in Table 4.1. The verification results show the utility of these fairly simple models in representing the transient responses to relatively large and varied inputs. Therefore, the models presented in Table 4.1 should be used for future XV-15 control system and handling-qualities analyses for the hover flight condition.

The next chapter discusses the dynamics for the cruise flight condition.

TABLE 4.1 Identified Transfer-Function Models for Hover

$$\frac{r}{\delta_r}(s) = \frac{0.619\ e^{-0.0210s}}{(0.102)}$$

$$\frac{p}{\delta_a}(s) = \frac{-3.71s(-0.107)(0.412)e^{-0.0313s}}{(0.102)(1.23)[-0.418,\ 0.447]}$$

$$\frac{r}{\delta_a}(s) = \frac{0.344(-0.345)[0.868,\ 0.487]e^{-0.00900s}}{(0.102)(1.23)[-0.418,\ 0.447]}$$

$$\frac{a_z}{\delta_c}(s) = \frac{-0.00980s\ e^{-0.00740s}}{(0.105)}$$

$$\frac{q}{\delta_e}(s) = \frac{-2.66s(-0.271)(0.508)e^{-0.0656s}}{(0.105)(1.32)[-0.463,\ 0.579]}$$

units:

p,q,r : deg/sec

a_z : g

$\delta_a, \delta_e, \delta_r$: deg

δ_c : %

Chapter 5

CRUISE DYNAMICS

This chapter discusses the open-loop dynamics of the XV-15 for the cruise flight condition (flight condition 4, Sec. 2.2).

As in hovering flight, the longitudinal and lateral flight dynamics are essentially fully decoupled. The primary longitudinal bare-airframe transfer functions of interest for "inner-loop" regulation are pitch-rate and normal-acceleration (at the center-of-gravity) responses to elevator deflection (q/δ_e) and (a_z/δ_e) respectively. The important lateral-directional transfer functions are roll-rate response to aileron (p/δ_a) and sideslip (at the center-of-gravity) response to rudder (β_{cg}/δ_r).

Frequency-sweep tests were executed much more easily in the cruise flight condition than in the hover condition. Cruise dynamics are inherently very stable, and transient motion is small relative to the large steady airspeed (V_i = 170 knots). This allowed good flight data to be rapidly obtained without requiring a large number of repetitions. Also, high-quality spectral identification was achieved without considerable adjusting of the various processing options--as was necessary in hover. Only two frequency-sweeps were needed in each axis because the spectral quality of all of the individual runs was satisfactory, and none needed to be discarded (as was required in the hover case). The chirp z-transform algorithm yielded excellent frequency-response identification in both axes over a wide frequency range.

Frequency-sweep data from the (VMS) piloted simulation were not available for the (V_i = 170 knots) cruise flight condition, so a direct comparison was not possible. However, the nonreal-time mathematical model (Ref. 3) for this condition is essentially identical to the real-time piloted-simulation (Ref. 2). Since the relative amplitude of motion about the high equilibrium flight speed is generally small, and the dynamics in the fixed-wing configuration are basically linear, the perturbation transfer-functions obtained from the nonreal-time version are satisfactory for mathematical model validation in this flight condition.

5.1 Lateral/Directional Dynamics

5.1.1 Frequency-Response Identification

The lateral stick inputs for two concatenated frequency-sweeps in the hover flight condition are shown in Fig. 5.1a. The input form is seen to be much more regular than in hover (compare with Fig. 4.1). The two runs are quite similar, with maximum amplitudes of about 20% of the full control authority. Since these tests were conducted with the lateral/directional SCAS axes disengaged, the surface deflection (excitation input) is related to the cockpit signal by a constant (mechanical compliance and hydraulic actuators contribute less than 10 msec of effective time delay). The roll-rate response for these two frequency-sweeps is shown in Fig. 5.1b. The maximum response amplitude of 10 deg/sec is similar to that experienced in hover (Fig. 4.5).

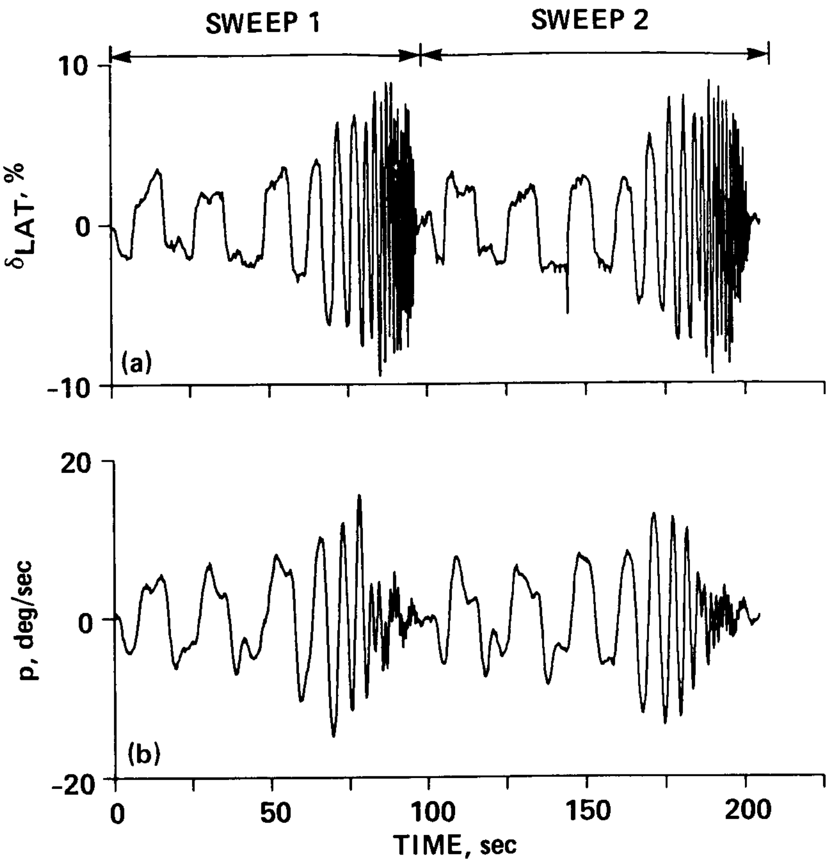

Fig. 5.1. Two Lateral Stick Frequency-Sweeps (δ_{LAT}) in Cruise. (a) Lateral Stick Inputs; (b) Roll-Rate.

The (open-loop) roll-rate response to ailerons, p/δ_a, is shown in Fig. 5.2. This is a classical first-order response in which aileron inputs produce a constant roll acceleration at high frequency and a constant roll rate at low frequency. The corner frequency is at about $\omega = 1$ rad/sec, with an associated phase lag of roughly $\Phi = -45$ deg, as expected. The dominant time-constant is thus about 1 sec, implying about 2-3 sec to reach a steady-state roll rate. Higher-order dynamics are not significant in this response since the phase lag is nearly constant for frequencies above 3 rad/sec. The coherence function shown

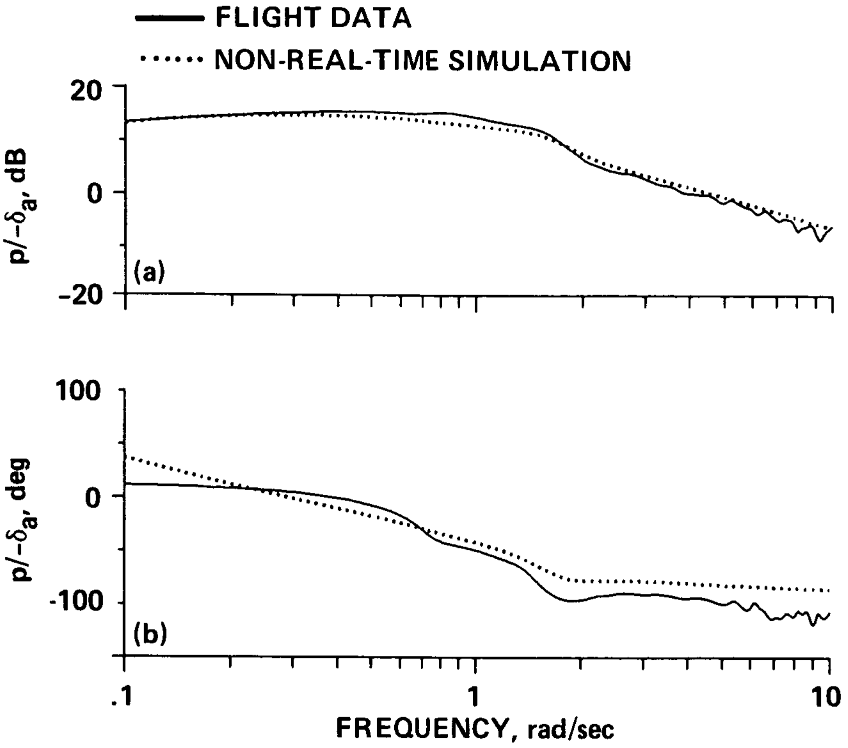

Fig. 5.2. Roll-Rate Response to Aileron ($p/-\delta_a$). (a) Magnitude; (b) Phase.

in Fig. 5.3 is very strong over the frequency range 0.1-8.5 rad/sec, indicating excellent identification of the roll-rate dynamics.

The perturbation transfer-function response from the nonreal-time simulation is shown with the flight data in Fig. 5.2. The magnitude response comparison is excellent at high and low frequencies, and shows only a slight error at mid-frequencies. The phase comparison (Fig. 5.2b) indicates that the simulation model overpredicts the damping ratio of the dominant roll-response mode (ω = 1 rad/sec). The phase error at high frequency is due to the omission of the high-frequency actuator dynamics in the simulation model. These various small discrepancies in Fig. 5.2 are insignificant because it is not possible to

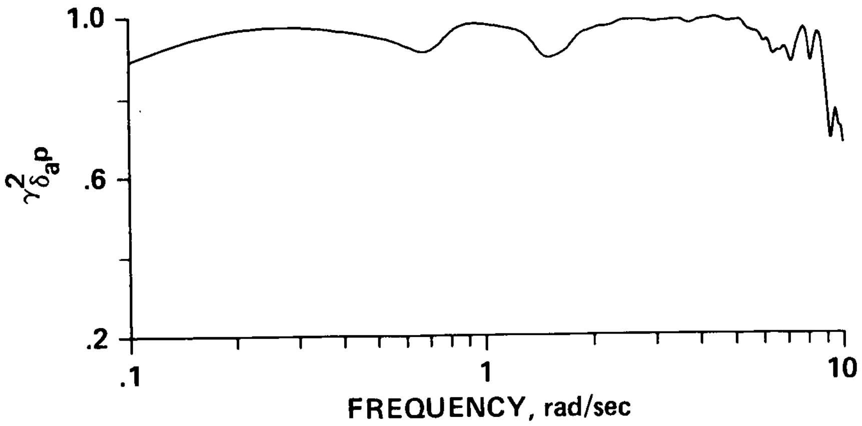

Fig. 5.3. Coherence Function ($\gamma^2_{\delta_a p}$) for Roll-Rate Response Identification.

perfectly match the test conditions of the aircraft with the simulation. Clearly, though, the simulation response characteristics are a very good representation of the actual vehicle response.

Aerodynamic sideslip measurements are obtained from a sideslip indicator located about 18 ft ahead of the aircraft center-of-gravity (c.g.). The sideslip at the c.g. (β_{cg}) is calculated by correcting the measured signal for position error based on yaw-rate and airspeed (no flow-distortion corrections were made). Also, no corrections are made for sensor dynamics, because these are not felt to be significant within the identification bandwidth.

The sideslip response (at the c.g.) to rudder inputs, β_{cg}/δ_r, is shown in Fig. 5.4. The response is characterized by a lightly damped second-order mode with a frequency of about 1.6 rad/sec. High-frequency rudder inputs yield a constant sideslip acceleration with no appreciable time-delay, and low-frequency rudder inputs yield a constant sideslip angle. The coherence function (Fig. 5.5) is strong over the frequency

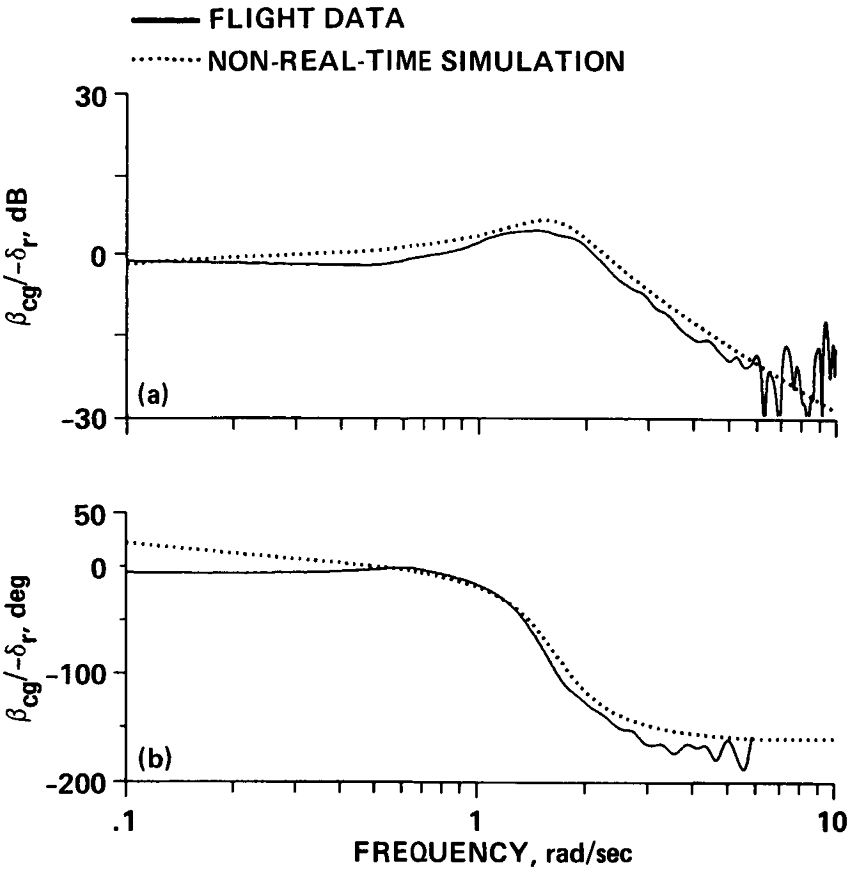

Fig. 5.4. Sideslip Response to Rudder ($\beta_{cg}/-\delta_r$). (a) Magnitude; (b) Phase.

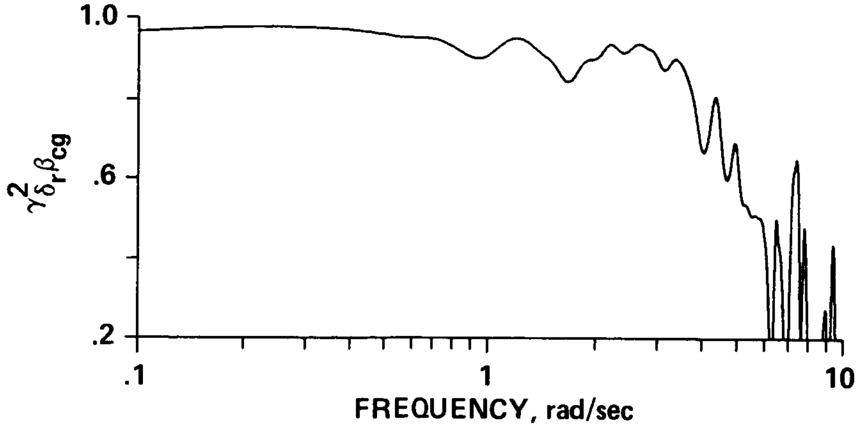

Fig. 5.5. Coherence Function ($\gamma^2_{\delta_r\beta_{cg}}$) for Sideslip Response Identification.

range 0.1-3.5 rad/sec, falling off sharply at higher frequencies. This rapid and relatively low-frequency decline of the coherence function results because the sideslip response falls off at a rate of -40 dB/decade, in contrast to the -20 dB/decade roll-off for the other response variables. However, since the yaw mode of interest has a natural frequency of about 1.6 rad/sec, the falling coherence for frequencies greater than 3.5 rad/sec is not a severe limitation.

The simulation frequency response of β_{cg}/δ_r is compared with the flight data in Fig. 5.4. As in the roll case, the comparison is generally excellent. The parallel (vertical) shift in the magnitude curves, suggests that the rudder yaw-response sensitivity is overestimated in the mathematical model by about 30%. This matches the rudder-response sensitivity discrepancy in hover and so further indicates a yaw inertia error. The slightly more shallow phase roll-off in the simulation response at high frequency is again due to the omission of actuator characteristics and perhaps a small overestimation in the damping ratio of the Dutch roll mode. Once again, however, these differences are not considered to be significant and could be attributed to differences in flight and loading conditions between the aircraft and the simulation model.

5.1.2 Transfer-Function Models

Equivalent system fitting for fixed-wing aircraft using decoupled lateral/directional models has been considered in detail by Bischoff and Palmer (Ref. 15). With the decoupled model, the responses are fit independently, using a first-order roll rate and a second-order sideslip transfer function. The coupled model approach is based on simultaneous fitting of the roll and sideslip responses to aileron and rudder, respectively, i.e., we obtain the following fourth-order transfer functions:

$$\frac{p(s)}{\delta_a(s)} = \frac{L_{\delta_a} s[\zeta_\phi, \omega_\phi]e^{-\tau_\phi s}}{(1/T_s)(1/T_r)[\zeta_d, \omega_d]} \tag{5.1}$$

where $p(s)/\delta_a(s)$ is the Laplace-transformed roll-rate response to aileron surface deflection (deg/sec/deg-aileron), L_{δ_a} is the aileron roll sensitivity, ζ_ϕ and ω_ϕ are the equivalent Dutch roll-mode damping and natural frequency, respectively, and τ_ϕ is the effective time delay, and

$$\frac{\beta_{cg}(s)}{\delta_r(s)} = \frac{Y_{\delta_r}(1/T_{\beta_1})(1/T_{\beta_2})(1/T_{\beta_3})e^{-\tau_\beta s}}{(1/T_s)(1/T_r)[\zeta_d, \omega_d]} \tag{5.2}$$

where $\beta_{cg}(s)/\delta_r(s)$ is the Laplace-transformed sideslip response to rudder surface deflection (deg/deg-rudder); Y_{δ_r} is the rudder sideslip sensitivity; $1/T_{\beta_1}$, $1/T_{\beta_2}$, and $1/T_{\beta_3}$ are the first-order numerator inverse time constants; and the denominator parameters are identical to those of Eq. (5.1). The effective time delay for the sideslip response is τ_β. The simultaneous fitting approach is consistent with that used in the longitudinal axis and allows the identification of the ω_ϕ/ω_d "coupling effect" in the roll response [Eq. (5.1)], which is important in handling-qualities assessments.

The coherence function results of Figs. 5.3 and 5.5 show a satisfactory identification of both roll and sideslip responses in the frequency range 0.1-3.5 rad/sec. Based on this fitting range, the computer program LATFIT is used to obtain the parameters of Eqs. (5.1) satisfactory over the wider range of 0.1-8.5 rad/sec, this degree of freedom is refitted alone, holding the denominator factors constant at the values obtained from the simultaneous solution. This procedure optimizes the values of the high-frequency gain and numerator parameters in the roll transfer function. The final results for the parameters of Eqs. (5.1) and (5.2) are

$$\frac{p}{\delta_a}(s) = \frac{-4.49s[0.313,\ 1.89]e^{-0.0450s}}{(0.0630)(1.09)[0.248,\ 1.58]} \tag{5.3}$$

$$\frac{\beta_{cg}}{\delta_r}(s) = \frac{-0.0510(0.0860)(0.818)(48.0)e^{-0.0260s}}{(0.0630)(1.09)[0.248,\ 1.58]} \tag{5.4}$$

The lateral/directional transfer function fits are plotted as dashed lines for comparison with the flight data of Figs. 5.6 and 5.7. The matching of the roll-response magnitude (Fig. 5.6a) is excellent over the entire frequency range. Only a slight anomaly in the phase matching (Fig. 5.6b) is apparent for low-frequency inputs. The agreement between the sideslip fit and the flight data is also excellent (Fig. 5.7).

As a result of the simultaneous fitting of the roll and yaw responses, the transfer-function parameters of Eqs. (5.3) and (5.4) have clearly retained their physical significance. The inverse roll mode time-constant $1/T_r = 1.09$ rad/sec is roughly equal to the frequency for -45 deg of phase lag as expected. The equivalent Dutch-roll mode is lightly damped, with a natural frequency roughly corresponding to the

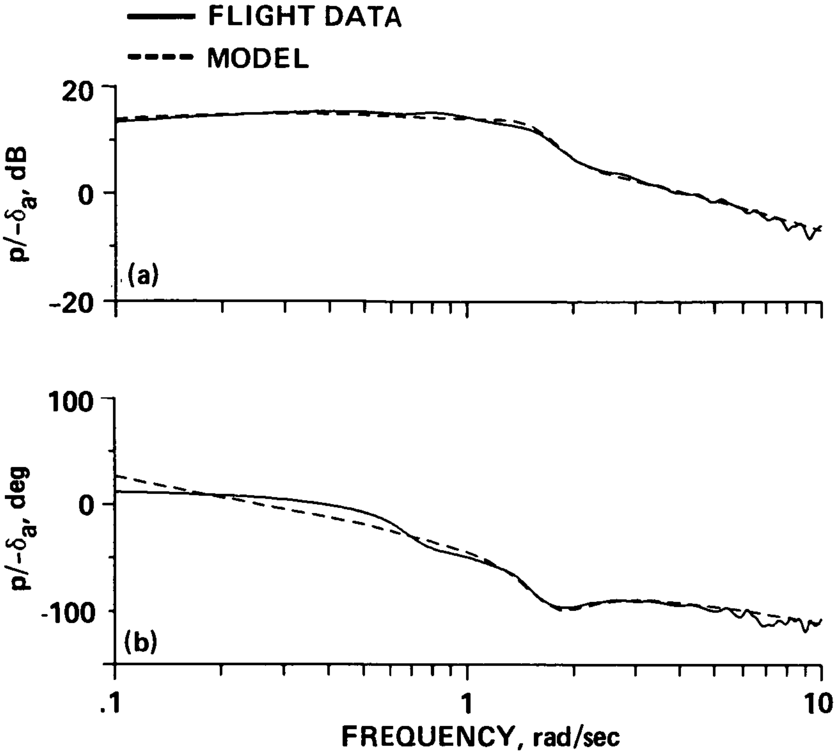

Fig. 5.6. Transfer-Function Model Identification for Roll-Rate Response to Aileron ($p/-\delta_a$). (a) Magnitude; (b) Phase.

peak in the sideslip Bode magnitude plot (Fig. 5.7a). The small effective time delays for the roll and sideslip responses reflect negligible high-frequency dynamics, and supports the omission of corrections for sideslip sensor dynamics.

The ratio of the natural frequency of the numerator complex zero, ω_ϕ, to that of the denominator complex pole, ω_d, is one measure of roll-yaw coupling in response to aileron inputs. When $\omega_\phi = \omega_d$, the numerator and denominator quadratic factors roughly cancel, and the resulting decoupled roll response is characterized entirely by the roll-mode time-constant. This case typically leads to the best handling qualities for a nominal value of the roll-mode time-constant. As the

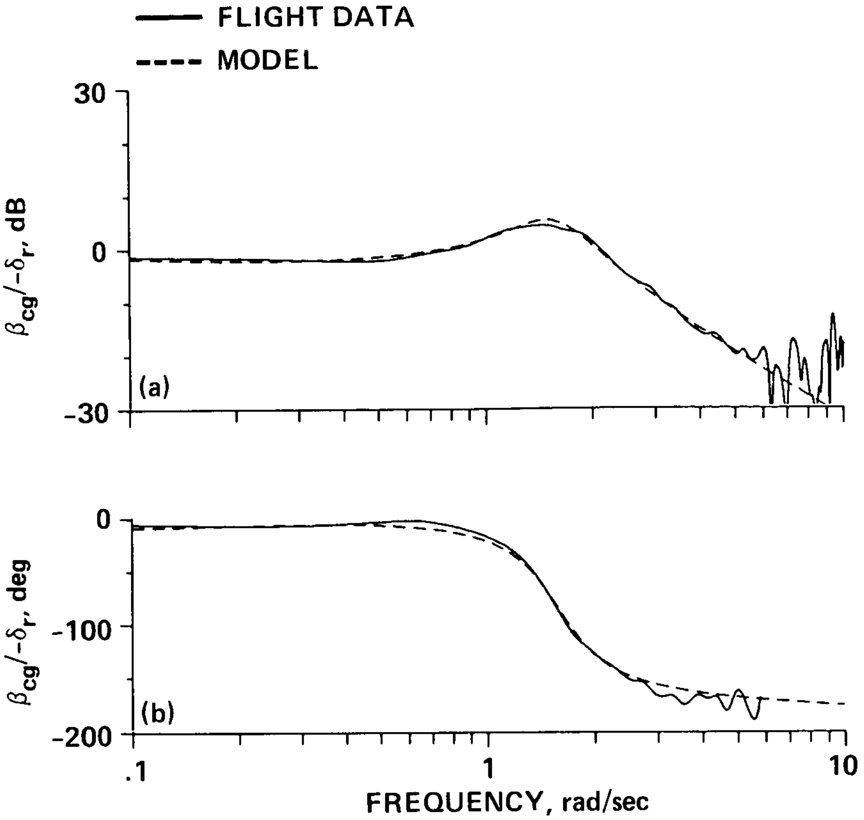

Fig. 5.7. Transfer-Function Model Identification for Sideslip Response to Rudder ($\beta_{cg}/-\delta_r$). (a) Magnitude; (b) Phase.

roll-yaw coupling increases, the numerator and denominator quadratic factors of Eq. (5.1) no longer cancel, and an undesirable oscillatory component of roll rate is generated. With reference to Eq. (5.3), the near-unity value of $\omega_\phi/\omega_d = 1.19$ suggests no such concern for roll-yaw coupling. Therefore, a simple, decoupled first-order roll-rate model could be adopted for future studies.

The poles and zeros of the identified roll-response transfer function are shown on the complex plane in Fig. 5.8. Roll-response handling qualities are specified in terms of the location of the dominant pole ($1/T_r$), with the Level I (desirable handling qualities) boundary

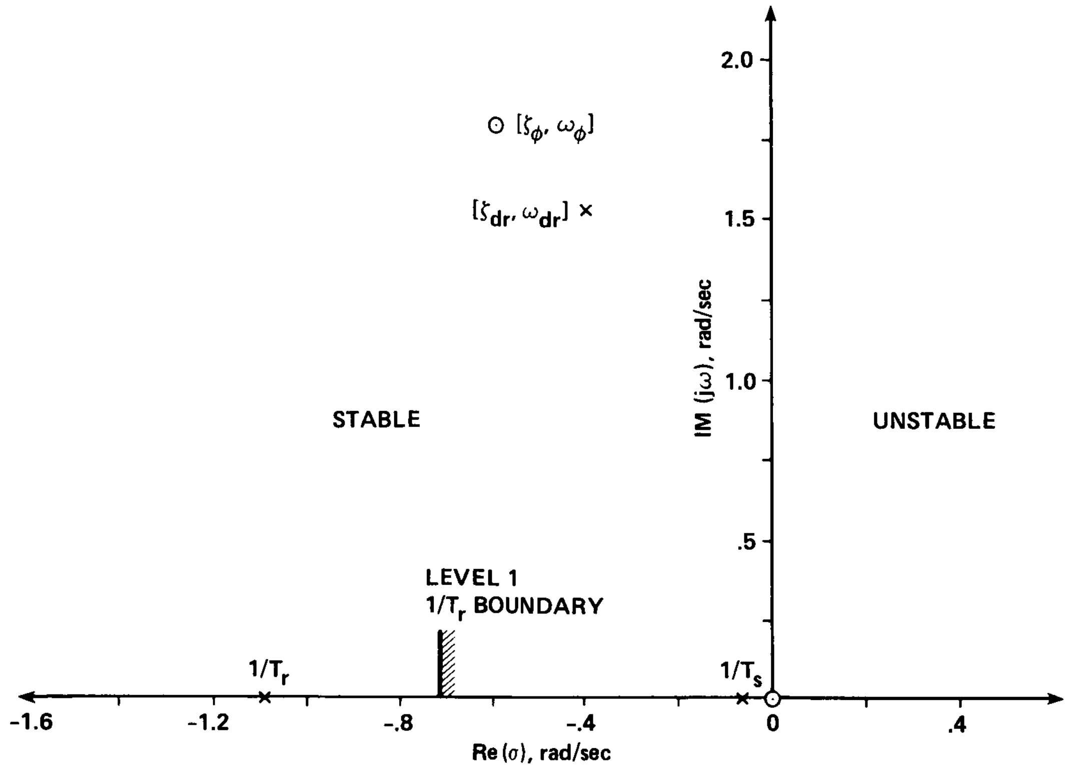

Fig. 5.8. Location of Roll-Rate Transfer-Function (p/δ_a) Parameters in the s-Plane.

(Ref. 17) shown in the figure. These results indicate very good lateral handling qualities for the cruise flight, in contrast to the poor open-loop lateral handling qualities for hover.

The identified transfer functions of Eqs. (5.3) and (5.4) are compared with the simulation perturbation transfer functions in Table 5.1. Comparison is seen to be excellent for all of the transfer function parameters, including the high-frequency sideslip response zeros. This comparison is a reflection of the very close frequency-response results presented in Figs. 5.2 and 5.4. The slightly more shallow phase roll-off for both the roll and sideslip responses

TABLE 5.1 Summary of Identification Results for Cruise

Frequency-Domain Identification	Nonreal-Time Simulation
$\frac{p}{\delta_a}(s) = \frac{-4.49(0)[0.313,\ 1.89]e^{-0.0450s}}{(0.0630)(1.09)[0.248,\ 1.58]}$	$\frac{p}{\delta_a}(s) = \frac{-4.76\ (0.00810)[0.322,\ 1.78]}{(0.0803)(0.937)[0.275,\ 1.66]}$
$\frac{\beta_{cg}}{\delta_r}(s) = \frac{-0.0510(0.0860)(0.818)(48.0)e^{-0.0260s}}{(0.0630)(1.09)[0.248,\ 1.58]}$	$\frac{\beta_{cg}}{\delta_r}(s) = \frac{-0.0688(0.028)(0.794)(45.8)}{(0.0803)(0.937)[0.275,\ 1.66]}$
$\frac{q}{\delta_e}(s) = \frac{-7.38(0.890)e^{-0.00500s}}{[0.536,\ 2.021]}$	$\frac{q}{\delta_e}(s) = \frac{-12.4(0.0454)(0.823)(6.37)}{[0.140,\ 0.168][0.505,\ 2.57](6.30)}$
$\frac{a_z}{\delta_e}(s) = \frac{-0.0230(-6.70)(7.59)e^{-0.00200s}}{[0.536,\ 2.021]}$	$\frac{a_z}{\delta_e}(s) = \frac{-0.0128(-0.00940)(0.0352)(6.49)(10.6)(-13.8)}{[0.140,\ 0.168][0.505,\ 2.57](6.30)}$

Units: p, q, r : deg/sec $\quad a_z$: g
δ_a, δ_e, δ_r : deg $\quad \beta_{cg}$: deg

(Figs. 5.6b and 5.7b) is reflected in the Dutch roll damping ratio discrepancy (11%).

5.2 Longitudinal Dynamics

5.2.1 Frequency-Response Identification

The elevator surface to pitch rate open-loop frequency response q/δ_e is shown in Fig. 5.9. The short-period-mode excitation causes a peak in the pitch-rate response at about 2.0 rad/sec, with an associated phase lag of -45 deg. At higher frequencies, the magnitude response

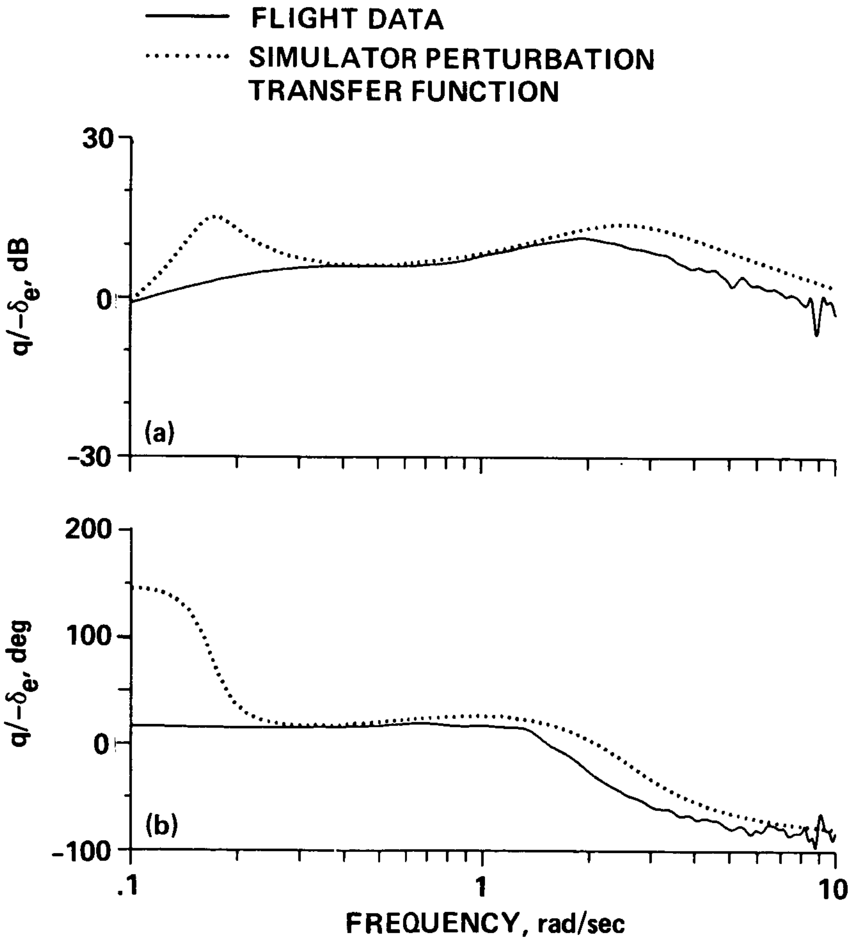

Fig. 5.9. Pitch-Rate Response to Elevator ($q/-\delta_e$). (a) Magnitude; (b) Phase.

rolls off at -20 dB/decade and the phase shift approaches -90 deg owing to the K/s pitch-rate characteristic and negligible flexibility/servolag effects. The drop in the magnitude response and associated positive phase response for frequencies below 0.3 rad/sec are due to the phugoid dynamics.

The coherence function shown in Fig. 5.10 is strong over the frequency range of 0.2-7.0 rad/sec. For input frequencies above

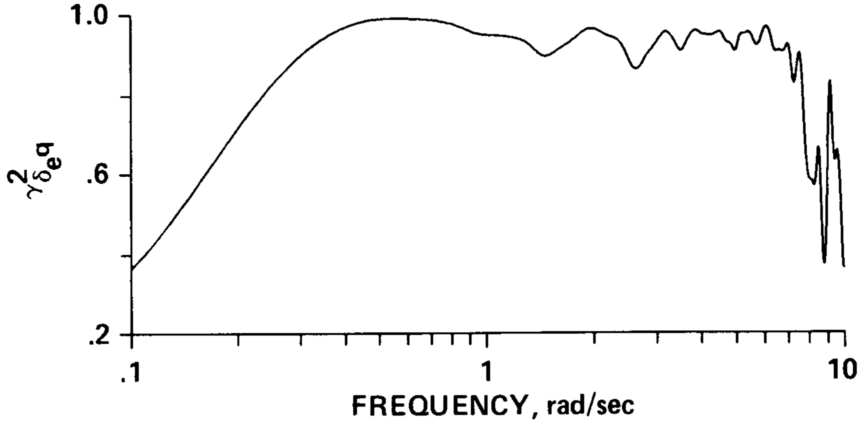

Fig. 5.10. Coherence Function ($\gamma^2_{\delta_e q}$) for Pitch-Rate Response Identification.

7.0 rad/sec, the coherence function becomes erratic and the transfer-function identification is less accurate. For low-frequency inputs (less than 0.3 rad/sec), the pitch-rate response decreases, even for the nearly constant input amplitude, owing to the effect of the phugoid dynamics. This results in a decrease of information transfer and an associated drop in the coherence function. This coherence function roll-off is also attributable to atmosphere turbulence effects, which become more important at low frequency where the turbulence spectrum peaks (Ref. 46).

The pitch-rate frequency response obtained from the simulation perturbation transfer function is shown with the flight data in Fig. 5.9. The comparison is excellent in the frequency range of 0.3-1.0 rad/sec showing that the mathematical model correctly predicts the steady-state pitch-rate response to elevator inputs. The differences at very low frequency are not conclusive because of the poor coherence for frequencies below 0.2 rad/sec (Fig. 5.10) and the lack of governor dynamics in the simulation perturbation transfer-function models. In the frequency range of 1-10 rad/sec there is a significant shift in the magnitude and phase curves between the aircraft and simulation responses. This discrepancy indicates that both the high-frequency gain and dominant response frequency are in error in the model. However, the fact that the steady-state gain is correct suggests a dynamic response rather than a static response error. This observation in addition to the fact that very good static trim correlation has been achieved in cruise (Ref. 5), suggests an error in the pitching moment-of-inertia, as was also indicated in the hover results. As previously discussed, ballast which is used in the aircraft for c.g. control, is not included in the present simulator data base and is a likely cause of this moment-of-inertia error. The nearly parallel shift between the simulation and flight data curves indicates that except for this error, the dominant vehicle dynamics are accurately modeled.

The normal-acceleration response to elevator, a_z/δ_e, is shown in Fig. 5.11. The response is dominated by the classical second-order short-period mode over most of the frequency range. The magnitude curve is flat at mid-frequency, indicating a constant normal acceleration (load factor) response to a step elevator input, with a roll-off in

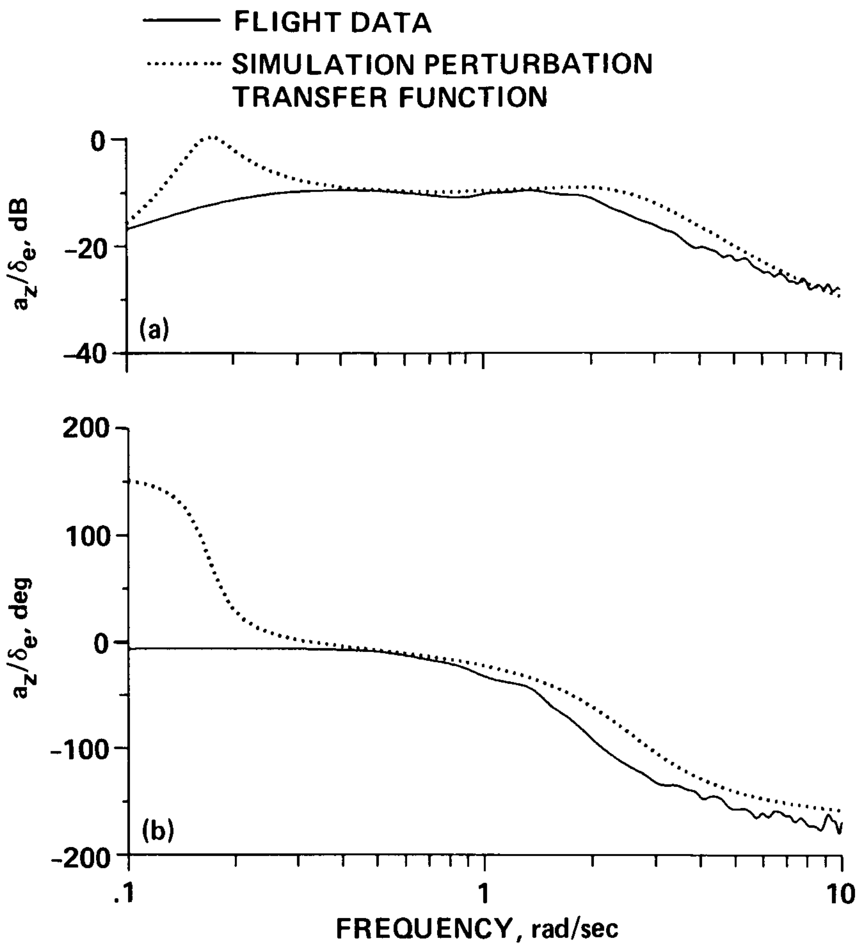

Fig. 5.11. Vertical-Acceleration Response to Elevator (a_z/δ_e). (a) Magnitude; (b) Phase.

response for frequencies beyond the short-period mode. The fall-off in normal acceleration response for frequencies below 0.3 rad/sec is probably a result of the dominance of the phugoid dynamics. The phase curve exhibits the classical second-order characteristic, that is, 0 deg of phase lag at low frequency, 180 deg of phase lag at high frequency, and 90 deg of phase lag at the second-order mode ($\omega \doteq 2.0$ rad/sec). This is consistent with the previous pitch-rate results. The coherence function for the normal acceleration response shown in Fig. 5.12 is strong over

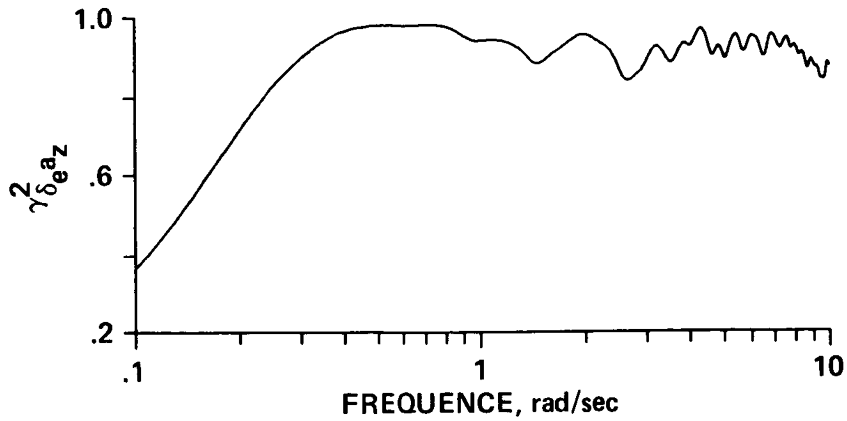

Fig. 5.12. Coherence Function ($\gamma^2_{\delta_e a_z}$) for Vertical-Acceleration Response Identification.

the wide frequency range of 0.3-10.0 rad/sec, with the fall-off at low frequency again resulting from the dominance of phugoid dynamics and turbulence effects. The simulation frequency-response is shown with the flight data in Fig. 5.11. As in the pitch case, the steady-state response to elevator inputs is accurately modeled in the simulation (0.3-1.0 rad/sec). Also, there is a parallel shift at high frequency in both the magnitude and phase curves, which as with the previous pitch-rate results, indicates an error in the assumed pitching moment-of-inertia.

5.2.2 Transfer-Function Models

Examination of the longitudinal frequency responses of Figs. 5.9 and 5.11 indicates that the longitudinal dynamics for this flight condition are dominated by short-period mode ($\omega_{sp} \doteq 2$ rad/sec). Therefore, the classical pitch-rate and center-of-rotation normal-acceleration responses to elevator are applicable:

$$\frac{q(s)}{\delta_e(s)} = \frac{M_{\delta_e}(1/T_{\theta_2})e^{-\tau_\theta s}}{[\zeta_{sp}, \omega_{sp}]} \tag{5.5}$$

where the $q(s)/\delta_e(s)$ is the Laplace-transformed pitch rate response to elevator surface deflection (deg/sec/deg-elevator); M_{δ_e} is the elevator pitch sensitivity; $1/T_{\theta_2}$ is the first-order numerator inverse time-constant; ζ_{sp} and ω_{sp} are the equivalent short-period mode damping and natural frequency, respectively; and τ_θ is the effective time delay. And

$$\frac{a_z(s)}{\delta_e(s)} = \frac{a_{z_{\delta_e}} e^{-\tau_{a_z} s}}{[\zeta_{sp}, \omega_{sp}]} \tag{5.6}$$

where $a_z(s)/\delta_e(s)$ is the Laplace-transformed vertical (positive downward) acceleration response at the instantaneous center-of-rotation to elevator surface deflection (g/deg-elevator), $a_{z_{\delta_e}}$ is the elevator vertical sensitivity and the denominator parameters are identical to those of Eq. (5.5). The effective time delay for the vertical-acceleration response is τ_{a_z}. The low-frequency phugoid dynamics are ignored, since, as seen in Figs. 5.9 and 5.11, these are important only for inputs of the very lowest frequencies.

The transfer-function parameters of Eqs. (5.5) and (5.6) are iteratively varied in order to obtain a best least-squares fit between the equations and the frequency-responses of Figs. 5.9 and 5.11 over the selected frequency range; commonality of the denominator parameters is imposed. For a first-cut model, the center-of-gravity (c.g.) and longitudinal instantaneous center-of-rotation (ICR) are assumed to be coincident. The iterative fitting procedure is completed using the LONFIT computer program. For the present case, the selected range for simultaneous fitting of the pitch-rate and normal acceleration responses is 0.3-7 rad/sec. In this frequency range, the dynamics are clearly dominated by the short-period mode and the coherence is strong for both transfer functions. Once the short-period damping and natural frequency ζ_{sp} and ω_{sp} are obtained for the simultaneous fit, the high-frequency gain for the normal acceleration response $a_{z_{\delta_e}}$ is varied, holding the damping and frequency constant. This procedure is analogous to that used in the lateral/directional case and optimizes the a_z fit over the frequency range 0.3-10.0 rad/sec, since the coherence function for this measurement remains strong out to higher frequencies. The transfer-function parameters for the pitch-rate and normal-acceleration responses are finally obtained:

$$\frac{q}{\delta_e}(s) = \frac{-7.73(1.04)e^{-0.0160s}}{[0.554,\ 2.18]} \tag{5.7}$$

$$\frac{a_z}{\delta_e}(s) = \frac{1.60e^{-0.0180s}}{[0.554,\ 2.18]} \tag{5.8}$$

A comparison of these lower-order models with the flight-test results is presented in Figs. 5.13 and 5.14. The pitch-response model [Eq. (5.7)] matches the data very well over the selected fitting range (0.3-7.0 rad/sec for q/δ_e), which shows that the short-period approximation adequately represents the high- and mid-frequency dynamics. For low-frequency inputs ($\omega < 0.3$ rad/sec), the phugoid mode causes a drop in the pitch response, a characteristic which is not "captured" by the

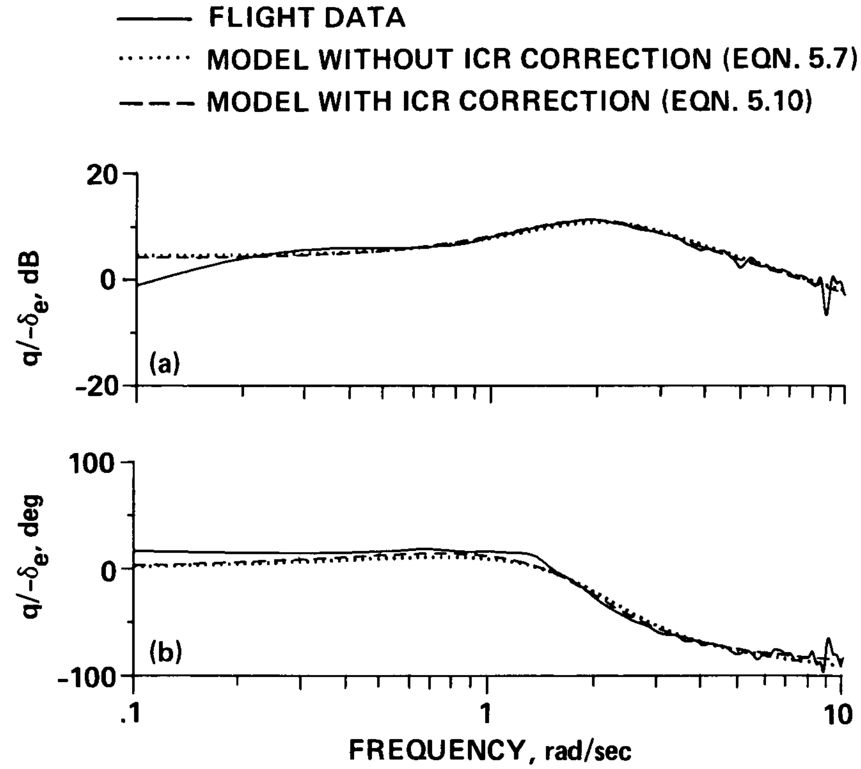

Fig. 5.13. Transfer-Function Model Identification for Pitch-Rate Response to Elevator ($q/-\delta_e$). (a) Magnitude; (b) Phase.

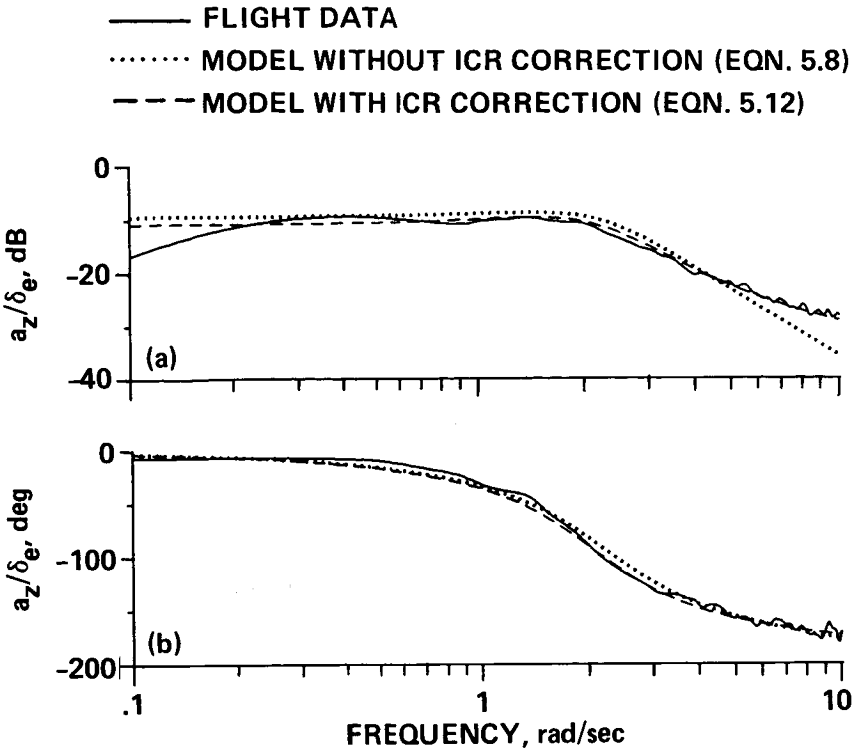

Fig. 5.14. Transfer-Function Model Identification for Vertical Acceleration Response to Elevator (a_z/δ_e). (a) Magnitude; (b) Phase.

short-period model. The match between the normal acceleration transfer function [Eq. (5.8)] and the flight data is not nearly as good in the fitting range, and shows a noticeable discrepancy in the magnitude response for frequencies greater than 2 rad/sec.

Such an error in the mid- and high-frequency a_z model could arise if the c.g. and ICR are not coincident. Then the vertical acceleration response at the c.g. is given approximately by

$$\frac{a_{z_{cg}}}{\delta_e}(s) \doteq \frac{a_{z_{ICR}}}{\delta_e}(s) - x_{cg}\, s\, \frac{q}{\delta_e}(s) \tag{5.9}$$

where x_{cg} is the (unknown) axial location of the center-of-gravity relative to the instantaneous center-of-rotation,

$$\frac{a_{z_{ICR}}}{\delta_e}(s) = \text{acceleration response at the ICR}$$

$$= \frac{a_z}{\delta_e}(s) \text{ of Eq. (5.6)}$$

$$\frac{q}{\delta_e}(s) = \text{Eq. (5.5)}$$

The frequency responses of Figs. 5.13 and 5.14 were refitted with the models of Eqs. (5.5) and (5.9), with x_{cg} included in the parameter search. The resulting model of pitch-rate response [Eq. (5.5)] is

$$\frac{q}{\delta_e}(s) = \frac{-7.38(0.890)e^{-0.00500s}}{[0.536,\ 2.02]} \tag{5.10}$$

The vertical acceleration response at the center-of-rotation [Eq. (5.6)] is

$$\frac{a_z}{\delta_e}(s) = \frac{1.17}{[0.536,\ 2.02]} \qquad (\tau_{az} = 0) \tag{5.11}$$

and the location of the c.g. relative to the ICR is $x_{cg} = -5.73$ ft (c.g. behind ICR). The resulting acceleration response at the c.g. is obtained from Eq. (5.9):

$$\frac{a_{z_{cg}}}{\delta_e}(s) = \frac{-0.0230(-6.70)(7.59)e^{-0.00200s}}{[0.536,\ 2.02]} \tag{5.12}$$

which is a higher numerator-order model than the simple model of Eq. (5.8), and displays the nonminimum phase (right-half plane) zero that results from the c.g. being located behind the ICR.

The pitch-rate model of Eq. (5.10) is shown in Fig. 5.13 for comparison with the previous results. Neither the frequency response nor the transfer-function parameters of the q/δ_e model are significantly altered by including the x_{cg} degree-of-freedom. However, the c.g. acceleration model of Eq. (5.12) fits the extracted frequency response much more closely, as shown in Fig. 5.14. Thus the noncoincident c.g. and ICR appear to be a likely source of the discrepancy obtained when the simple model of Eq. (5.8) is used.

The identified short-period damping and frequency ($\zeta_{sp} = 0.536$ and $\omega_{sp} = 2.02$ rad/sec) are consistent with preliminary observations, which were based on the raw Bode plot information. The relatively high degree of damping is a reflection of the small response peak of the pitch-rate transfer function. The small effective time delays (in the pitch attitude and normal acceleration transfer-function fits) indicate that the high-frequency flexibility effects are not important for this flight condition, as noted earlier. The military standards requirements (Ref. 17) for lower-order equivalent system pitch response are given in terms of the parameters $\omega_{sp}T_{\theta_2}$, ζ_{sp}, τ_θ. The values of these parameters given in Eq. (5.10) are well within the Level I, category A, indicating desirable longitudinal handling for cruise flight.

The identified transfer functions are compared with the simulation perturbation transfer functions in Table 5.1. The simulation transfer functions contain an additional complex mode associated with the phugoid dynamics and a nearly canceling pole/zero pair associated with the rotor angular velocity (rpm) degree-of-freedom. The fact that the rpm mode nearly cancels and that the phugoid mode is at very low frequency justifies ignoring these dynamics and adopting the simple short-period models.

The pole and zero locations of the simulation transfer functions compare very well with the flight-extracted results. The good correspondence of the numerator factors in the vertical acceleration response supports the corrections based on instantaneous center-of-rotation effects [Eqs. (5.9), (5.12)]. The differences in short-period frequency and pitch-response sensitivity can both be explained by the error in pitching moment-of-inertia. The pitch-axis sensitivity M_{δ_e} is the pitching moment (foot-pounds) per inch of elevator normalized by the pitching inertia (I_y) (Ref. 41). The ratio of pitch sensitivities for the simulation and flight results (Table 5.1) gives:

$$\frac{(M_{\delta_e})_{sim}}{(M_{\delta_e})_{flight}} = 1.67 = \frac{(I_y)_{flight}}{(I_y)_{sim}} \qquad (5.13)$$

The short-period frequency ω_{sp} depends on the square-root of stability derivatives which are also normalized by the pitching moment-of-inertia (Ref. 41). Based on the short-period frequency:

$$\frac{(\omega_{sp})_{sim}}{(\omega_{sp})_{flight}} = 1.29 = \sqrt{1.67} = \left[\frac{(I_y)_{flight}}{(I_y)_{sim}}\right]^{1/2} \qquad (5.14)$$

which is the same result as in Eq. (5.13). Thus, an error in pitch inertia would explain the differences in both pitch sensitivity and short-period frequency, while not disturbing the good static trim correlation. An underestimation of pitch inertia in the simulation is indicated from both the hover and cruise results, although there is some discrepancy in the error ratio (67% from the cruise results and 25% from the hover results).

5.3 Verification of Transfer-Function Models

The high degree of inherent bare-airframe stability for the cruise flight condition makes open-loop verification inputs much easier to complete than in the hover condition. Steady initial conditions and clean long-duration (6-8 sec) step inputs are easily obtained. The aircraft (filtered) roll-rate response to a step aileron input is shown in Fig. 5.15. The transfer-function model of Eq. (5.3) shown in the

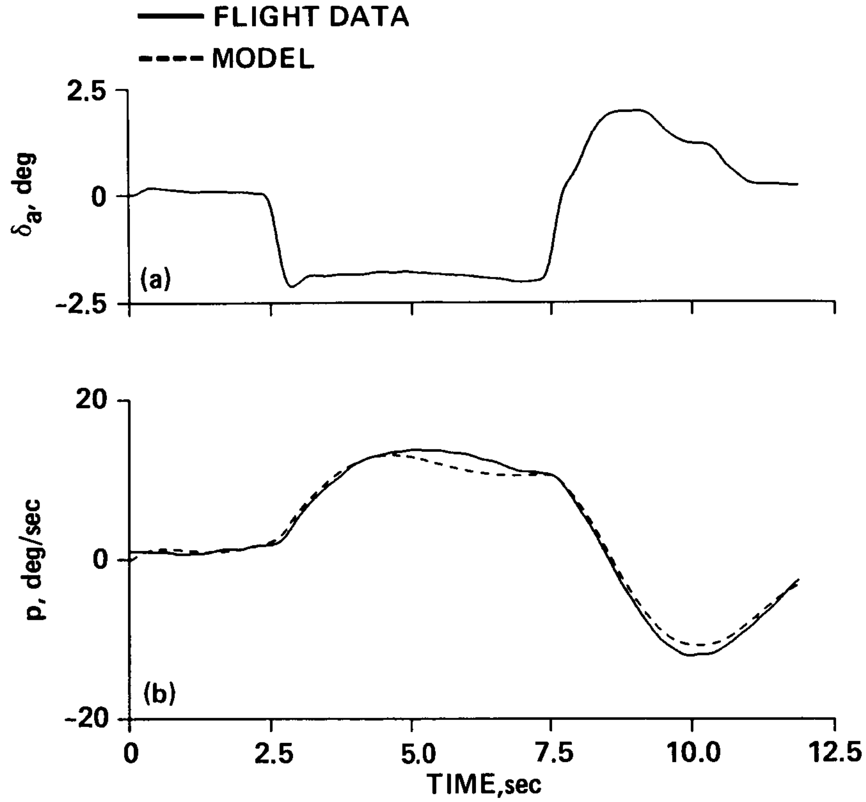

Fig. 5.15. Roll-Response Model Verification Using SCAS-off Flight Data. (a) Aileron Input; (b) Roll-Rate.

dashed line matches the flight data quite well for the entire input duration, except for some discrepancy in steady-state roll rate. This error may be associated with the p/δ_a transfer-function model mismatch at mid-frequency (Fig. 5.6), some nonlinear effects associated with the large steady-state roll rate, or simply a gust. The sideslip response to a step rudder input is shown in Fig. 5.16, with the appropriate corrections for the nose-boom position. The transfer-function model of Eq. (5.4) matches the flight data almost identically for the entire time-history.

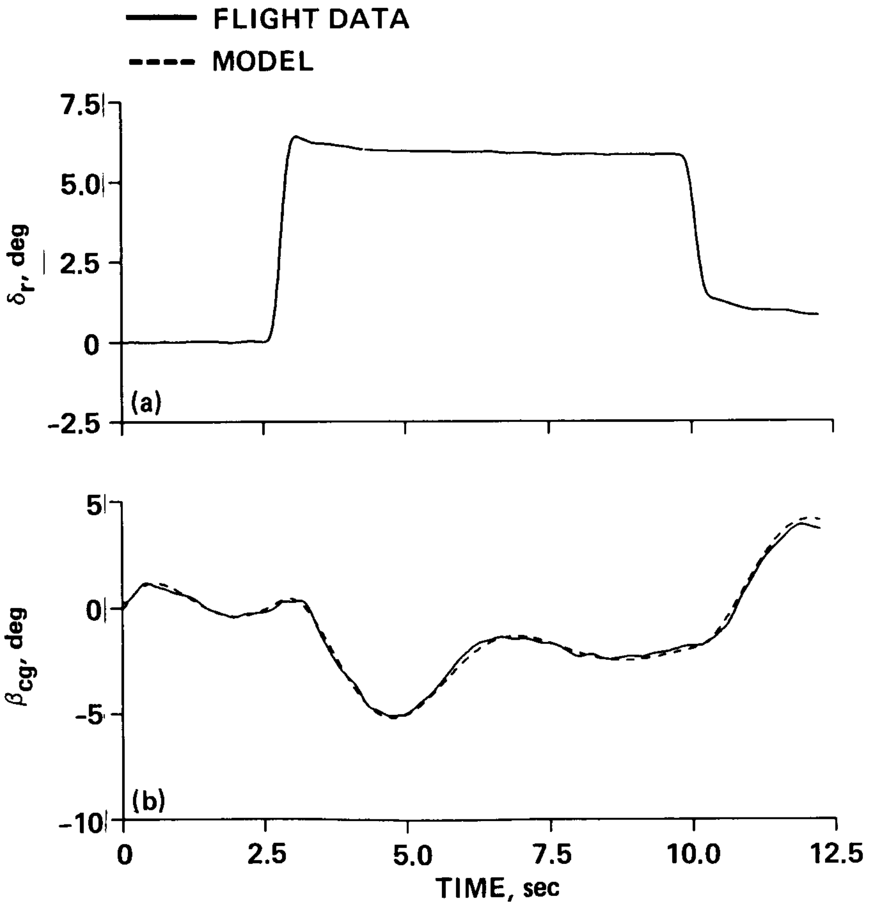

Fig. 5.16. Sideslip-Response Verification Using SCAS-off Flight Data. (a) Rudder Input; (b) Sideslip Response.

For most of the flight tests, frequency-sweeps and step inputs were performed consecutively for each flight condition, thus maintaining constant altitude, airspeed, and loading condition. Unfortunately, the open-loop elevator step response data for $V_i = 170$ knots were taken at $H_d = 2800$ ft (density altitude), whereas $H_d = 10{,}000$ ft for the sweeps. Since the indicated airspeed was constant and, therefore, also the dynamic pressure, the derived pitch-rate model is valid for the lower-altitude step responses. However, the significant difference in true airspeed (about 20 knots) and associated centripetal acceleration ($= U_0 q$) makes an a_z step response comparison invalid for these data. The response to elevator doublet inputs, obtained from closed-loop (SCAS-on) tests, for $V_i = 170$ knots and $H_d = 12{,}000$ ft is used to validate the a_z model, although the aircraft loading condition (and altitude) is still not exactly matched.

The SCAS-off (open-loop) pitch-rate response to step elevator deflection ($H_d = 2800$ ft) is shown in Fig. 5.17. The elevator input corresponds to about 40% of the maximum control deflection. The comparison between the ICR-corrected model response [Eq. (5.10)] and the flight data is seen to be very good over most of the time-history. The slight deviations occurring toward the end of the run are due to the inadequacy of the short-period approximation in modeling the low-frequency (phugoid) dynamics (see Fig. 5.13a). Even so, the short-period approximation clearly gives an excellent characterization of the important initial response dynamics.

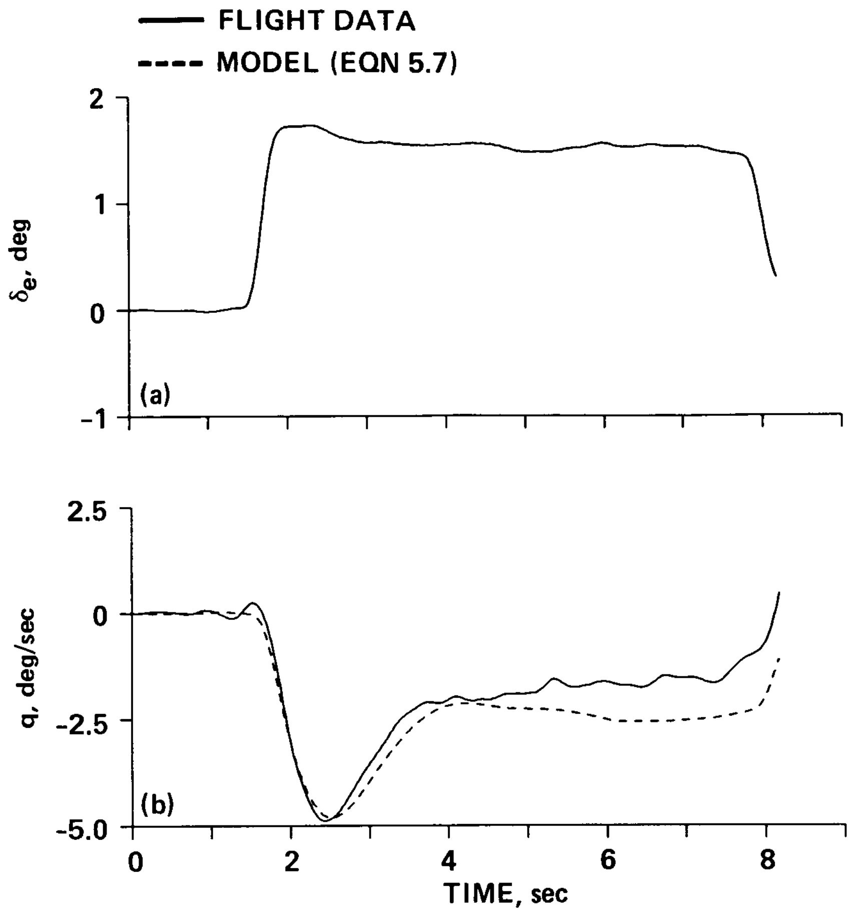

Fig. 5.17. Pitch-Response Model Verification Using SCAS-off Flight Data (h_d = 2800 ft). (a) Elevator Input; (b) Pitch Rate.

The pitch-rate model also compares favorably with the flight data for the response to an elevator doublet input, as shown in Fig. 5.18c. However, the normal-acceleration model of Eq. (5.12) is not very good. The initial reversal predicted by the model (effect of the x_{cg} correction) does not occur in the flight response in Fig. 5.18c. In fact, if the original center-of-rotation model of Eq. (5.8) is used, the match with the flight data is much better, as is also shown in Fig. 5.18c. These results indicate that the $a_{z_{cg}}/\delta_e$ model which includes the center-of-rotation correction [Eq. (5.12)] is highly tuned to the

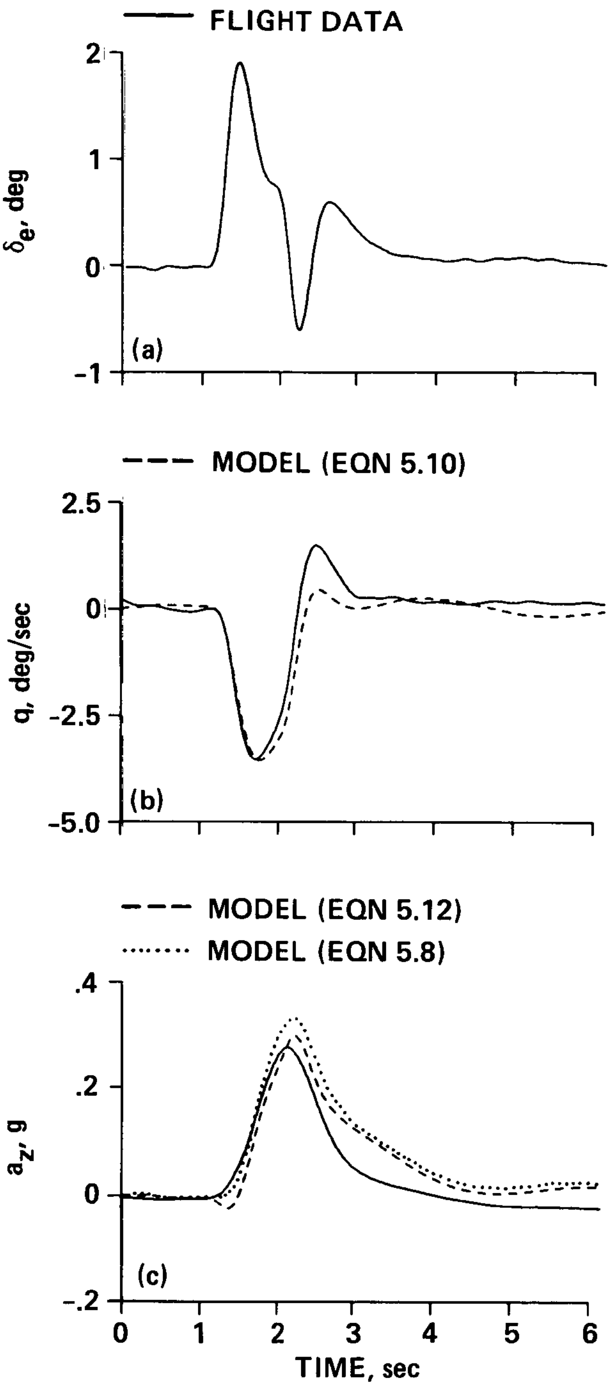

Fig. 5.18. Pitch and Vertical-Acceleration Response Model Verification Using SCAS-on Flight Data (h_d = 12000 ft). (a) Elevator Input; (b) Pitch Rate; (c) Vertical-Acceleration Response.

measured frequency response for sinusoidal inputs (Fig. 5.14) and is not robust to small changes in flight condition and input form. The fact that acceleration is a higher-order state derivative than the other angular-rate derivatives further exaggerates the sensitivity of this model, especially for the initial (high-frequency) response dynamics. Therefore, the lower-order model of Eq. (5.8) should be used for future handling qualities and control-system analyses of this flight condition. This is a good example of the dangers of model overparameterization. The capability to evaluate directly the effect of model order on response fitting is also clearly seen in this example, again representing a unique advantage of the frequency-domain approach for this kind of comparison.

Overall, these verification results indicate that the derived lower-order transfer functions are very good predictors of the open-loop vehicle response in cruise over a wide frequency range.

Chapter 6

CONCLUSIONS

The following conclusions are separated into those specifically associated with the analysis of the XV-15 and those associated with the analysis of the frequency-response identification method in general.

6.1 Analysis of the XV-15

Specific findings from the identification of the open-loop hover dynamics are as follows.

1. Heave response to power lever and yaw response to rudder are decoupled from the other degrees-of-freedom and are very lightly damped.

2. Pitch and roll open-loop dynamics exhibit unstable low-frequency oscillations. High pilot work-load should be expected in the event of a SCAS failure in either of these axes.

3. Significant coupling of yaw response to aileron has been identified. Pedal deflection equal to about 50% of lateral stick inputs is necessary to maintain a fixed heading.

4. The effective high-frequency time-delays are small in all axes and are probably not important in determining the handling-qualities of the XV-15 aircraft.

5. The comparison of piloted simulation and flight-test dynamic results for high-frequency inputs ($\omega > 1.0$ rad/sec) is generally favorable in all axes, with larger anomalies existing for low-frequency inputs. However, underestimates in the pitch and yaw inertias used in the simulation model caused the overprediction of pitch- and yaw-control sensitivities.

6. Small-perturbation transfer functions obtained from the piloted-simulator (VMS) are poor representations of the low-frequency dynamics. However, perturbation transfer functions for the current nonreal-time simulation compare more favorably with the flight data, suggesting that the corrections to the mathematical models have been appropriate.

7. The step responses of the identified transfer-functions and the aircraft generally match quite well, even for large-amplitude motions. This verifies that an accurate representation of the open-loop hover dynamics has been achieved, and that the hover transfer-function models derived herein can be used for future XV-15 control system and handling-qualities analyses.

Specific findings from the identification of the open-loop cruise (V_i = 170 knots) dynamics are as follows.

1. The response characteristics are very stable and decoupled, and indicate desirable open-loop handling-qualities.

2. Standard lower-order equivalent models adequately match the identified dynamics in all degrees-of-freedom except for the normal acceleration responses to elevator deflection. Although a center-of-rotation correction is needed to accurately fit the a_z/δ_e frequency-response data, the resulting higher-order model is not robust to small changes in flight condition and input form.

3. Small perturbation transfer functions and associated frequency responses from the nonreal-time simulation correlate very well with the flight-extracted results except for an error in the simulation pitch and yaw inertias.

4. The step responses of the identified transfer functions and the aircraft generally match very well.

6.2 Frequency-Response Identification Method

1. Non-parametric frequency-response identification techniques produce an excellent physical understanding of basic vehicle dynamics.

2. Non-parametric techniques are especially useful for documenting the response characteristics of a new configuration for which a prior parametric model is not known.

3. Extraction of open-loop responses from closed-loop data is feasible with frequency-sweep inputs. Closed-loop testing of rotorcraft with highly unstable bare-airframe dynamics allows the execution of long duration inputs needed for low-frequency response identification.

4. Multi-input/multi-output frequency-domain methods are suitable for extracting the coupled responses of rotorcraft.

Chapter 7

RECOMMENDATIONS FOR FUTURE STUDY

The objectives of the XV-15 study (Sec. 1.1) have been achieved. The following recommendations pertain to future studies of the frequency-response identification method.

Future studies in frequency-response identification should focus on advancing the method in two major areas:

1. Reconstruction of physical stability-derivatives from the transfer-function matrix
2. Generalization of two-input/single-output frequency-response identification to multi-input/multi-output (MIMO) systems

7.1 Reconstruction of Physical Stability Derivative Parameters

The frequency-response method illustrated in this study yields a transfer-function matrix for the coupled system. The next logical step in a full identification procedure is to reconstruct the physical stability-derivative (state-space) realization rather than a canonical realization as in the present aproach. The MIMO state-space reconstruction approach given by Chen (Ref. 47) is well suited for this purpose because it takes into account the physical redundancy in the transfer-function zeros. Frequency-domain parameter identification would thus be completed in a three step procedure:

Step 1. Frequency-response identification

Step 2. Transfer-function modeling

Step 3. Stability-derivative reconstruction

By breaking the parameter-identification approach into these three distinct steps, maximum benefit can be gained from the nonparametric identification before the parametric step is attempted. This approach may yield both a more accurate, and physically meaningful and consistent state-space model than can be identified using direct time-domain or frequency-domain parameter-identification procedures.

Stability-derivative reconstruction should be tested on the XV-15 transfer-functions for the hover flight condition, since a complete state-space model has previously been identified for this condition using time-domain identification methods (Ref. 22). The frequency-domain parameter-identification procedure should then be tested on a single-rotor helicopter which has more highly-coupled system dynamics than the XV-15.

7.2 Generalization to MIMO Systems

Spectral quality assessment is conducted on each input/output record pair to determine the runs suitable for concatenation and best window sizes. Although this assessment is relatively straightforward, the process is computer and labor intensive, and could be automated using a rule-based algorithm. This would be especially useful for MIMO identification where the number of required frequency responses increases rapidly with additional cross-coupling paths.

The two-input identification software tools developed (or adapted) in this study (TISOSA, TFTHISTORY, NAVFIT, LONFIT, LATFIT) need to be further improved to allow MIMO identification and verification of systems with more than two control inputs. A general matrix formulation will allow extension to the multi-input case.

Multi-input/multi-output frequency-response identification tools should be tested on a modern single-rotor helicopter to assess their suitability for highly-coupled, hingeless (or bearingless) rotor systems.

Appendix A

CHIRP z-TRANSFORM

Existing computer programs for identifying frequency-responses from flight data generally use the standard (Cooley-Tukey) FFT procedure to transform data from the time-domain to the frequency-domain (Refs. 10, 11, 13). Initial versions of the FRESPID program also used a standard FFT algorithm, but this was later replaced by the chirp z-transform (CZT). The mathematical basis for this algorithm is given in Refs. 28 and 32, and is not discussed in this appendix. The CZT provides more flexibility in selection of computational parameters than is allowed by the standard FFT. However, it has increased computational time and storage requirements.

Three important differences between the FFT and the CZT are reviewed in this appendix: (1) Resolution, Δf; (2) Starting frequency, f_0; and (3) Window size, $L\Delta t$. These parameters define the discrete Fourier transform calculation (DFT), which is repeated from Eq. (3.2):

$$X(f_k) = X(k\Delta f) = \Delta t \sum_{n=0}^{N-1} x_n \exp[-j2\pi(kn)/N] \; ; \quad k = 0, 1, 2, \ldots, N-1 \tag{A.1}$$

where

$X(f_k)$ = Fourier coefficients

$x_n = x(n\Delta t)$

Δt = time increment

N = number of discrete frequency points

A.1 Resolution

The (frequency) resolution of the standard FFT (Δf) is determined by the width of the window ($L\Delta t$, sec), since for this algorithm the number of time-history points (L) is also the same as a number of output spectral points (N):

$$\Delta f = \frac{1}{L\Delta T} \text{ ; Hz} \tag{A.2}$$

which in terms of the sampling frequency $f_s = 1/\Delta t$ is

$$\Delta f = \frac{f_s}{L} = \frac{f_s}{N} \tag{A.3}$$

Thus, the FFT output frequencies are N evenly spaced points around the unit circle. Since the z-transform is a mirror image with respect to the Nyquist frequency ($f_c = f_s/2$), the second half of the spectrum ($f_s/2 < k\Delta f < f_s$) is redundant and is not actually calculated in the FFT procedure of Eq. (A.1). Furthermore, the Nyquist frequency is generally selected to be much greater than the upper end of the identification frequency range (0.1-10.0 rad/sec = 0.016-1.59 Hz in the present study) to avoid digital distortion, so many of the spectral calculation points are not needed ($1.59 < k\Delta f < f_s/2$).

The basic difference in the CZT algorithm is that the spectral calculation is completed along an arbitrary specified arc in the z-plane. When, as in the present case, this arc is taken as a segment of the unit circle, the CZT provides the Fourier coefficients. A key characteristic of the CZT is that the number of calculation points N

within this segment is arbitrary; thus, the frequency resolution is also arbitrary[†]:

$$\Delta f = \frac{f_1 - f_0}{N} \tag{A.4}$$

where

f_0 = starting spectral frequency (arbitrary, Sec. A.2)

f_1 = ending spectral frequency (arbitrary, Sec. A.2)

A commonly held misconception is that arbitrary frequency resolution can also be achieved using the standard FFT by simply "padding" the input sequence with zeroes (artificially increasing L). However, padding with zeroes only allows interpolation between true frequency resolution points ($\Delta f = f_s/L$) and does not increase the frequency resolution. The only way to increase the true frequency resolution of the standard FFT is to increase the width of the window, which decreases the amount of averaging and so increases the random error (Sec. 3.2.3).

A.2 Starting Frequency

The minimum output frequency f_0 that can be identified using the standard FFT procedure is also the frequency spacing:

$$f_0 = \Delta f = \frac{1}{L\Delta t} \tag{A.5}$$

[†] The author has encountered numerical problems with the CZT algorithm when the number of output points (N) is much greater than the number of input points (L), $N \geq 2L$. However, since all the output points are concentrated within the desired frequency range, the resulting frequency resolution is still substantially higher than is achievable with the standard FFT procedure.

Reducing the starting frequency to allow an identification of the lower frequency dynamics means selecting wider windows and, therefore, reducing the amount of spectral averaging [and increasing the spectral variance, Eq. (3.10)]. In the CZT, the initial (and final) frequency f_0 (and f_1) is arbitrary. Thus, the initial frequency is independently selected to correspond to the lower end of the frequency range of interest ($f_0 = 0.1/2\pi = 0.016$ Hz in this case).

A.3 Window Size

In both the standard FFT and CZT procedures, window size ($L\Delta t$) controls the balance between low-frequency signal content and spectral averaging (Sec. 3.2.1). In the standard FFT, the number of time-history points in the window must be an integer power of 2 (a "composite number," e.g., 512, 1024, 2048). Thus, the allowable adjustment in the width of window is coarse (only halving or doubling in size), for a fixed sample interval (Δt). The chirp z-transform allows the arbitrary selection of L (including prime numbers). The capability to independently set the starting frequency (f_0, Sec. A.2) and then finely tune the window size yields both improved coherence and lower spectral variance over a wide frequency range as compared to the standard FFT.

These three characteristics of the chirp z-transform make it a significantly more flexible algorithm than the standard FFT; this flexibility can yield a substantial improvement in the spectral resolution and dynamic range, especially at the low-frequency end. The author has found the flexibility of the chirp z-transform to be very important in achieving high-quality frequency-response identification from (noisy) flight data.

Appendix B

LIMITATIONS IN CLOSED-LOOP IDENTIFICATION

The identification of low-frequency helicopter dynamics requires long-duration inputs. In hover flight the dominant open-loop dynamics are unstable, so execution of these inputs with the stability and control augmentation system disengaged (SCAS-off) is not practical. Therefore, it is desirable to extract the open-loop dynamics from flight-test data obtained with the augmentation system engaged ("closed-loop identification").

This appendix derives the fundamental relationships for single-input/single-output closed-loop identification in the presence of process noise. A simple relationship relating bias errors in the identified open-loop frequency-response to the input-to-process noise ratio is developed. A numerical study illustrates the important concepts using a simple model of the XV-15 unstable dynamics in hover.

B.1 Spectral Relationships

Consider the identification of the single-input/single-output roll-rate response to aileron from closed-loop tests as illustrated in Fig. B.1. The closed-loop system is the same as that previously discussed in Sec. 3.2.4 (Fig. 3.7), except in the present case the compensation element (G_c) is placed in the forward loop. This provides a steady-state closed-loop gain of approximately unity--independent of the compensation gain. The other elements of Fig. B.1 are as follows.

1. δ_L = pilot lateral-stick input
2. p = measured roll-rate (measurement noise is neglected here)

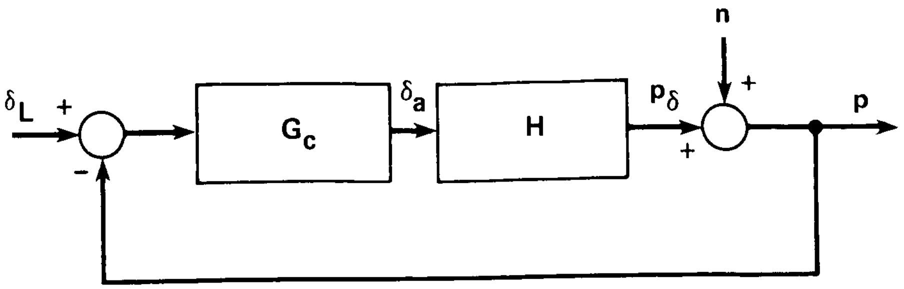

Fig. B.1. Closed-Loop Identification.

3. δ_a = total aileron surface deflection
4. $H = p_\delta/\delta_a$ = open-loop roll-rate frequency-response
5. n = roll-rate process noise.

Some common sources of noise are: (a) turbulence, the autospectrum of n is determined from the turbulence velocity autospectrum and the roll-rate response to turbulence velocity inputs; (b) neglected secondary inputs; (c) nonlinear remnants which are not accounted for by the linear open-loop frequency-response H. The external inputs from the pilot and process noise sources are assumed to be uncorrelated; viz., $G_{\delta_L n} = 0$.

The desired open-loop frequency-response estimate is obtained from Eq. (3.8):

$$\hat{H} = \frac{G_{\delta_a p}}{G_{\delta_a \delta_a}} \tag{B.1}$$

The cross-spectrum $G_{\delta_a p}$ is determined from Fig. B.1 (Ref. 28):

$$G_{\delta_a p} = G_{\delta_a p_\delta} + G_{\delta_a n} \tag{B.2}$$

Substituting Eq. (B.2) into Eq. (B.1):

$$\hat{H} = \frac{G_{\delta_a p_\delta} + G_{\delta_a n}}{G_{\delta_a \delta_a}} \qquad (B.3)$$

$$\hat{H} = \underbrace{H}_{\text{True response}} + \underbrace{\frac{G_{\delta_a n}}{G_{\delta_a \delta_a}}}_{\text{Bias error}} \qquad (B.4)$$

which shows that the spectral estimate is biased by correlation between the aileron surface and process noise inputs. This bias term is zero for open-loop systems since the pilot and process noise inputs are uncorrelated; the undesirable correlation results from the feedback of the process noise around the loop. Equation (B.4) also shows that the true (unbiased) open-loop frequency-response is identified regardless of the level of compensation when process noise is not present.

The cross-spectrum $G_{\delta_a n}$ is determined from the closed-loop relationship between process noise inputs and aileron surface response (Ref. 28)†:

$$G_{\delta_a n} = (G_{n\delta_a})^* = G_{nn}\left(\frac{\delta_a}{n}\right)^*$$

$$= G_{nn}\left(\frac{-G_c}{1 + G_c H}\right)^* \qquad (B.5)$$

---

† Asterisk (*) denotes complex-conjugate.

The aileron surface input-autospectrum is composed of components from the two external (uncorrelated) excitations:

$$G_{\delta_a\delta_a} = G_{\delta_L\delta_L}\left|\frac{\delta_a}{\delta_L}\right|^2 + G_{nn}\left|\frac{\delta_a}{n}\right|^2$$

$$= G_{\delta_L\delta_L}\left|\frac{G_c}{1 + G_cH}\right|^2 + G_{nn}\left|\frac{-G_c}{1 + G_cH}\right|^2 \qquad \text{(B.6)}$$

Substituting Eqs. (B.5) and (B.6) into Eq. (B.4):

$$\hat{H} = H - \frac{G_{nn}[G_c/(1 + G_cH)]^*}{|G_c/(1 + G_cH)|^2(G_{\delta_L\delta_L} + G_{nn})} \qquad \text{(B.7)}$$

But,

$$\left|\frac{G_c}{1 + G_cH}\right|^2 = \left(\frac{G_c}{1 + G_cH}\right)^* \left(\frac{G_c}{1 + G_cH}\right) \qquad \text{(B.8)}$$

so,

$$\hat{H} = H - \frac{G_{nn}}{[G_c/(1 + G_cH)][G_{\delta_L\delta_L} + G_{nn}]} \qquad \text{(B.9)}$$

When the closed-loop system is excited only by process noise (i.e., no pilot inputs), $G_{\delta_L\delta_L} = 0$ and

$$\hat{H} = H - \frac{G_{nn}}{[G_c/(1 + G_cH)]G_{nn}}$$

$$\text{(B.10)}$$

$$\hat{H} = -\frac{1}{G_c}$$

which is the limiting condition of identifying the inverse compensation. This result is in agreement with the simple analysis of Eqs. (3.11 and 3.12).

When pilot and process noise inputs are both present, we can define the signal-to-noise ratio:

$$S^2(\omega) \equiv \frac{G_{\delta_L \delta_L}(\omega)}{G_{nn}(\omega)} \tag{B.11}$$

which depends on frequency.

Substituting Eq. (B.11) into Eq. (B.9) and normalizing the estimate by the true frequency-response yields the following normalized bias error:

$$\varepsilon_b = \frac{b[\hat{H}]}{H} = \frac{-1}{[G_c H/(1 + G_c H)][S^2(\omega) + 1]} \tag{B.12}$$

where it should be recognized that the denominator term in Eq. (B.12) $G_c H/[1 + G_c H]$ is the closed-loop transfer-function. The open-loop unstable modes of rotorcraft are generally at frequencies well below the open-loop crossover frequency ω_c (defined as frequency at which $|G_c H| = 1$) for hovering vehicles. In the case of the XV-15, the dominant open-loop unstable modes are at a frequency of about $\omega = 0.5$ rad/sec [Eq. (4.4)], compared to a crossover frequency of $\omega_c = 2.5$ rad/sec (closed-loop time-constant = 0.4 sec, Sec. 2.1.4). At low frequency ($\omega < \omega_c$), the closed-loop transfer-function becomes (Ref. 41)

$$\left.\frac{G_cH}{1 + G_cH}\right|_{\omega<\omega_c} \doteq 1 \qquad \text{(B.13)}$$

which when substituted into Eq. (B.12) gives the following simple expression for the normalized bias error in the frequency range of the open-loop dynamics:

$$\varepsilon_b = \frac{1}{S^2(\omega) + 1} \qquad \text{(B.14)}$$

Equation (B.14) indicates that the normalized bias error can be kept to within 10% ($\varepsilon_b < 0.10$) for a signal-to-noise ratio:

$$S(\omega) > 3 \qquad \text{(B.15)}$$

In terms of the noise-to-signal ratio $\hat{\sigma}(\omega) \equiv 1/S(\omega)$, the requirement is

$$\hat{\sigma}(\omega) < 0.33 \qquad \text{(B.16)}$$

which was quoted in Sec. 3.2.4.

This analysis shows that the pilot's input must exceed the input from process noise by at least a factor of 3 across the frequency range of interest to reduce the normalized bias error to an acceptable value. The use of the frequency-sweep, which generates a persistent and relatively large vehicle response over the entire identification frequency range, ensures that this condition is maintained and that the bias errors are small. Multi-step inputs generally do not have uniform power distribution. If process noise inputs are large in the frequency range where the multi-step signal content is small, large bias errors may result, making such inputs poorly suited for closed-loop identification.

B.2 Numerical Study

A numerical study was conducted to illustrate the concepts discussed in the preceding section and to validate the expression for normalized bias error given in Eq. (B.14). A simple model of the XV-15 dynamics in hover is used to facilitate a clear physical understanding of the limitations of closed-loop identification, which is important for future applications.

B.2.1 Simplified Closed-Loop Model

The open-loop roll-rate response in hover [Eq.(4.4)] is represented by a simple (normalized) first-order unstable transfer-function:

$$H(s) = \frac{e^{-0.005s}}{s - 0.5} \tag{B.17}$$

where the 5 msec time-delay is included to account for numerical integration.

The compensation transfer-function is assumed to be a pure gain:

$$G_c = K \tag{B.18}$$

The closed-loop time-constant of the XV-15 roll-response in hover is 0.4 sec (Sec. 2.1.4), which implies a closed-loop first-order roll-mode at $s = -2.5$ rad/sec, yielding a compensation gain of:

$$K = 3.0 \tag{B.19}$$

The pilot lateral-stick excitation was derived by passing a Gaussian random sequence (200-sec duration) through a low-pass filter (1.0 rad/sec roll-off frequency). This yields an input-autospectrum ($G_{\delta_L \delta_L}$) approximating that of the lateral-stick frequency-sweep of Fig. 4.2. For illustrative simplicity, the process noise spectrum was also obtained by passing a Gaussian random sequence through the 1.0 rad/sec low-pass filter. This yields a signal-to-noise ratio $S(\omega)$ which is independent of frequency, and is just equal to the stick input-to-noise rms ratio.

A simulation program was developed to numerically integrate the governing equations of Fig. B.1 and provide time-histories for frequency-response identification using the FRESPID program. Results were obtained as a function of the noise-to-signal ratio $\hat{\sigma} = 1/S$ for the nominal compensation gain of the XV-15 (K = 3.0) and a gain typical of a high-bandwidth control system (K = 6.5 rad/sec).

B.2.2 Results of Numerical Study

The open- and closed-loop frequency-responses (p/δ_a and p/δ_L, respectively) for the nominal gain (K = 3.0) are shown in Figs. B.2 and B.4, along with the ideal transfer-functions. The associated coherence functions shown in Figs. B.3 and B.5 indicate nearly perfect identification over the entire frequency range, with a slight random error for the open-loop response in the frequency range near the dominant open-loop mode ($\omega = 0.5$ rad/sec). The open-loop frequency-response is

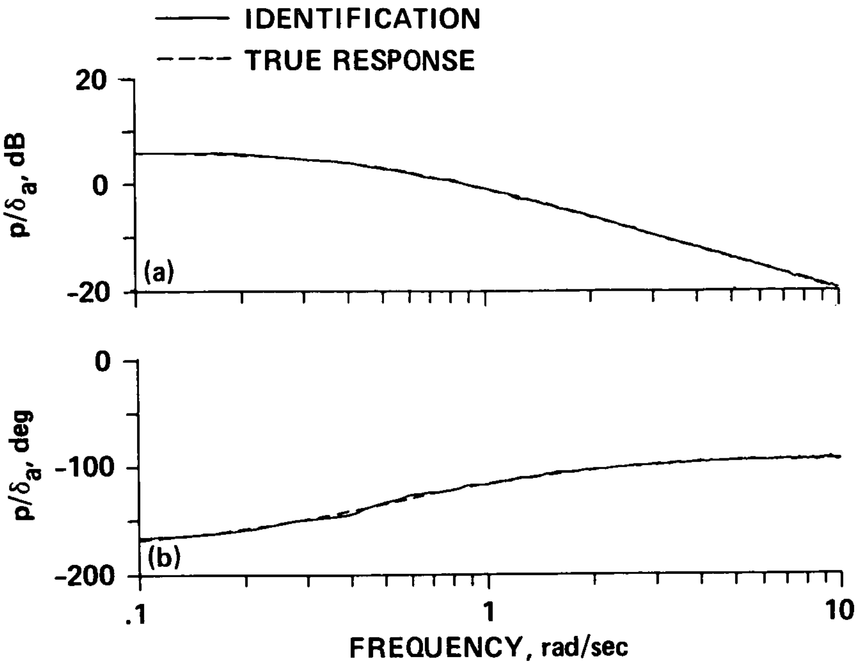

Fig. B.2. Identification of Open-Loop Frequency Response for the Nominal-Gain System, K = 3.0. (a) Magnitude; (b) Phase.

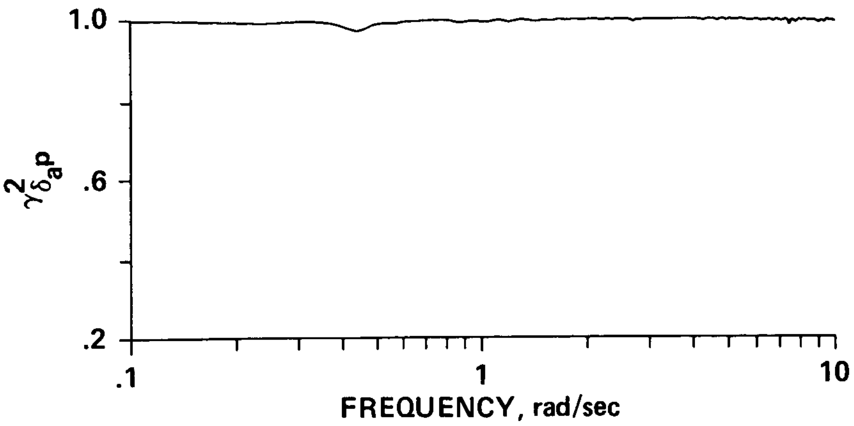

Fig. B.3. Coherence Function for Open-Loop Roll-Rate Identification, Nominal-Gain System, K = 3.0.

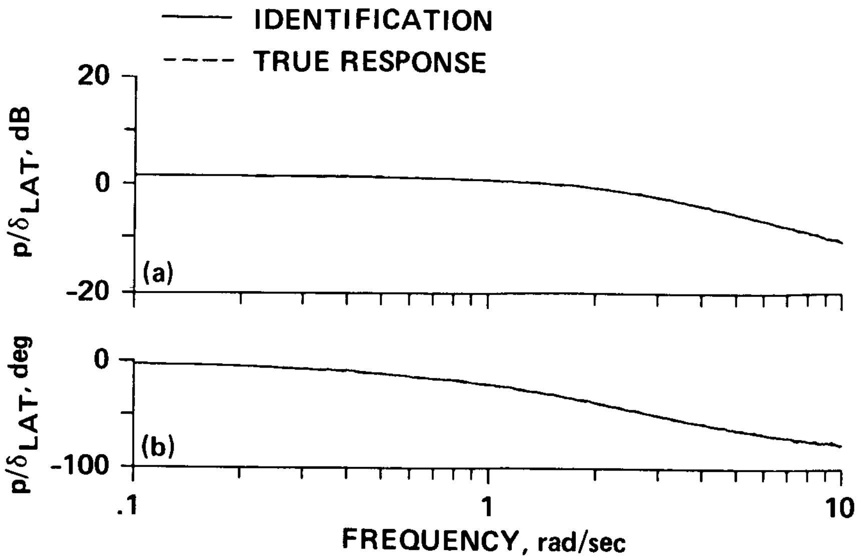

Fig. B.4. Identification of the Closed-Loop Frequency-Response for the Nominal-Gain System, K = 3.0. (a) Magnitude; (b) Phase.

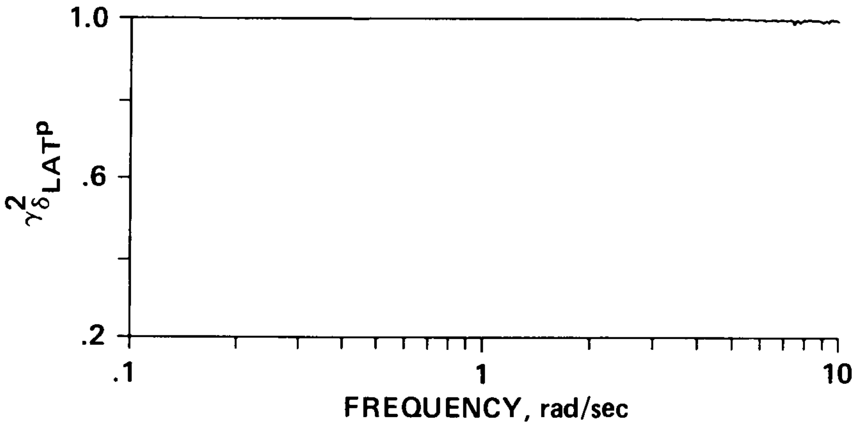

Fig. B.5. Coherence Function for Closed-Loop Response Identification, Nominal-Gain System, K = 3.0.

also identified with almost no error for the high-gain case (Figs. B.6, B.7); the higher-bandwidth closed-loop frequency-response matches the true response (Figs. B.8, B.9).

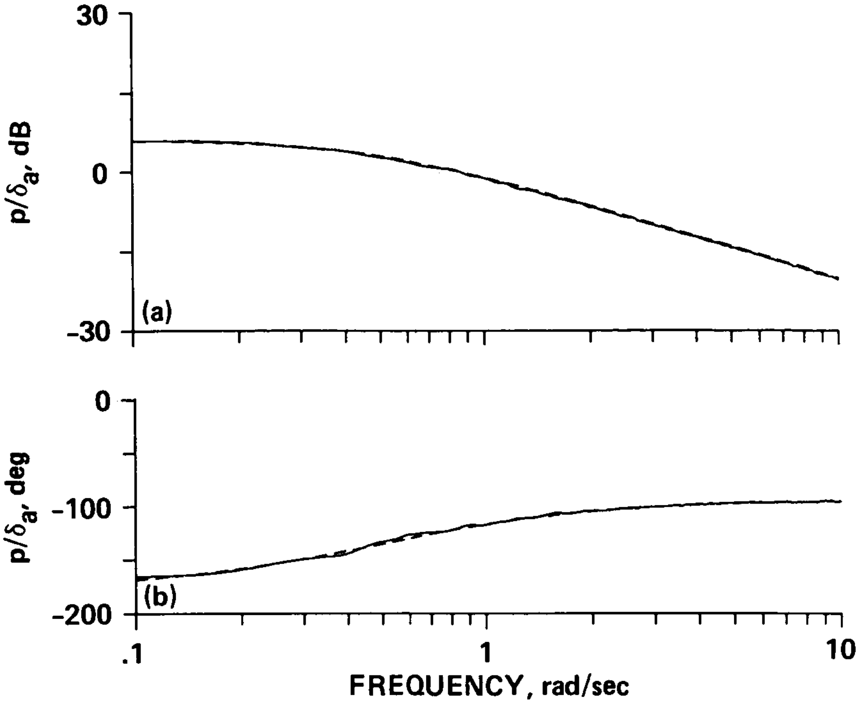

Fig. B.6. Identification of the Open-Loop Frequency-Response for the High-Gain System, K = 6.5. (a) Magnitude; (b) Phase.

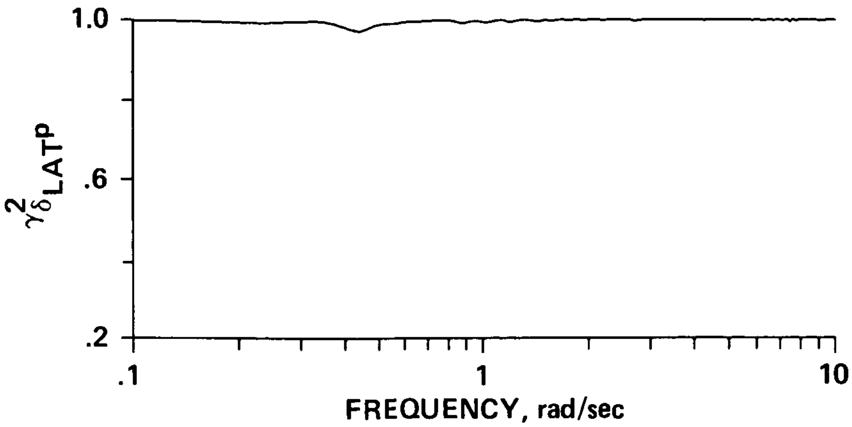

Fig. B.7. Coherence Function for Open-Loop Response Identification, High-Gain System, K = 6.5.

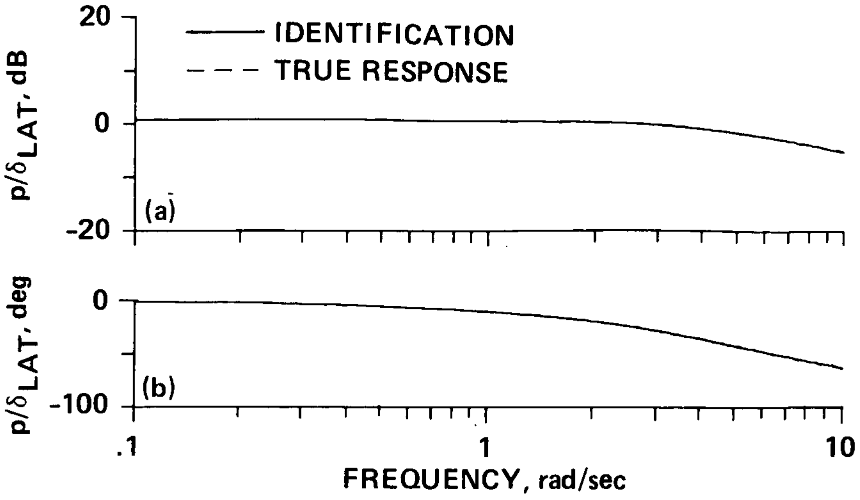

Fig. B.8. Identification of the Closed-Loop Frequency-Response for the High-Gain System, K = 6.5. (a) Magnitude; (b) Phase.

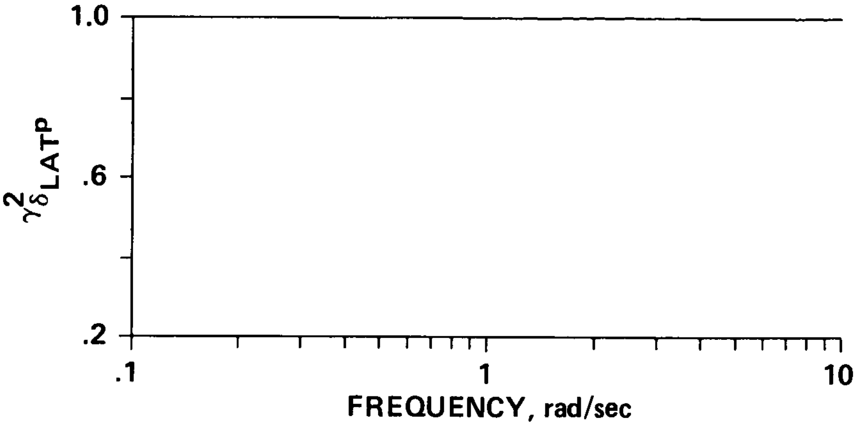

Fig. B.9. Coherence Function for Closed-Loop Response Identification, High-Gain System, K = 6.5.

The effect of increasing the noise-to-signal ratio $\hat{\sigma}$ on the open-loop identification for the nominal gain system is shown in Figs. B.10 and B.11. Very little error is apparent for noise-to-signal ratios of $\hat{\sigma} < 0.3$. At moderate noise-to-signal ratios ($\hat{\sigma} = 0.3$-1.0), the identification errors (associated with both bias and random error

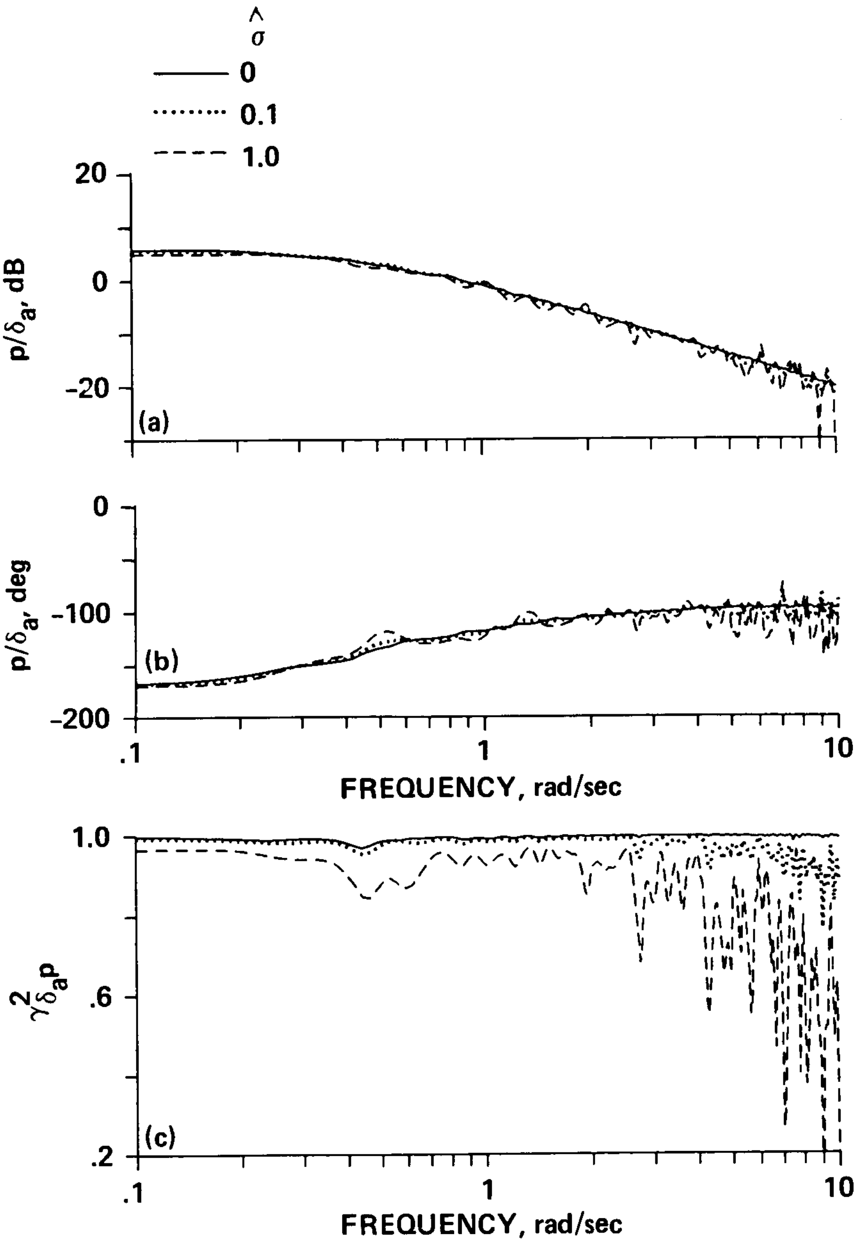

Fig. B.10.* Effect of Noise-to-Signal Ratios $\hat{\sigma}$ = 0, 0.1, 0.3 on the Identification of the Open-Loop Frequency-Response for the Nominal-Gain System, K = 3.0. (a) Magnitude; (b) Phase; (c) Coherence.

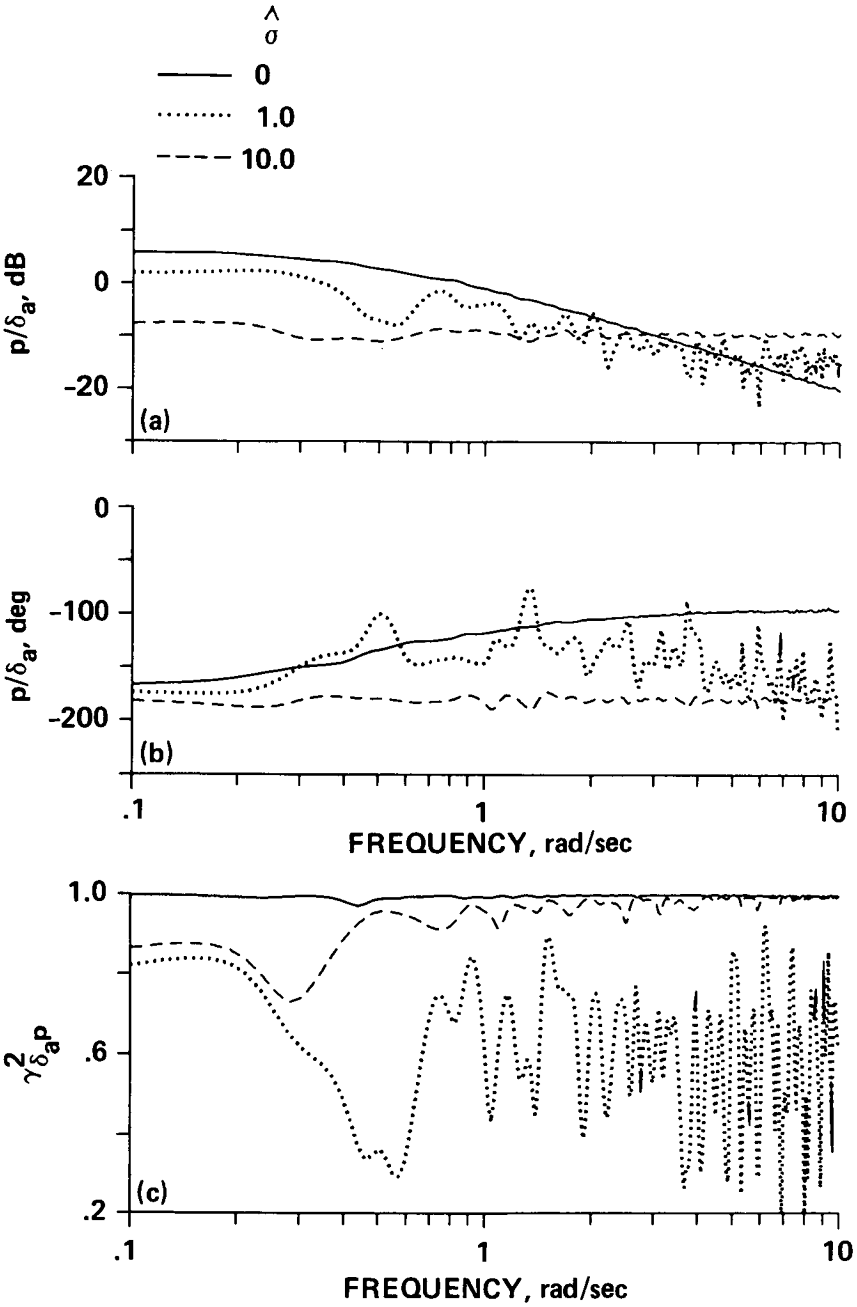

Fig. B.11. Effect of Noise-to-Signal Ratios $\hat{\sigma}$ = 0, 1.0, 10.0 on the Identification of the Open-Loop Frequency-Response for the Nominal-Gain System, K = 3.0. (a) Magnitude; (b) Phase; (c) Coherence.

contributions) are significant and are reflected by the drop in the coherence function. Thus, for low and moderate noise levels, the coherence function remains a good indicator of spectral accuracy for closed-loop identification. The case of nearly infinite noise-to-signal ratio ($\hat{\sigma} = 10$) shows that the open-loop frequency-response identification approaches the inverse compensation transfer-function as indicated in Eq. (B.10):

$$\left|-\frac{1}{G_c}\right| = \left|-\frac{1}{K}\right| = 0.333 = -9.54 \text{ dB}$$

$$\measuredangle\left(-\frac{1}{G_c}\right) = \measuredangle\left(-\frac{1}{K}\right) = -180 \text{ deg} \tag{B.20}$$

and the associated coherence function approaches unity (Fig. B.11c).

A better quantitative appreciation for the effect of process noise on the identified open-loop frequency-response is achieved by looking at two measures of error. The first measure is the total rms error. This relates the deviation between the estimated open-loop frequency-response $\hat{H}$ and the true open-loop frequency-response H [Eq. (B.17)]:

$$\sigma_{e_g} = \left[\frac{1}{20}\sum_{n=1}^{20}[\hat{H}_{dB}(\omega) - H_{dB}(\omega)]^2\right]^{1/2}$$

$$\sigma_{e_p} = \left[\frac{1}{20}\sum_{n=1}^{20}[\hat{H}_{deg}(\omega) - H_{deg}(\omega)]^2\right]^{1/2} \tag{B.21}$$

These calculations are performed by the NAVFIT program, which selects 20 linearly spaced frequency points across the logarithmic scale (Sec. 3.3.2). The total rms magnitude and phase errors are plotted as a function of noise-to-signal ratio $\hat{\sigma}$ in Figs. B.12a and B.12b for the

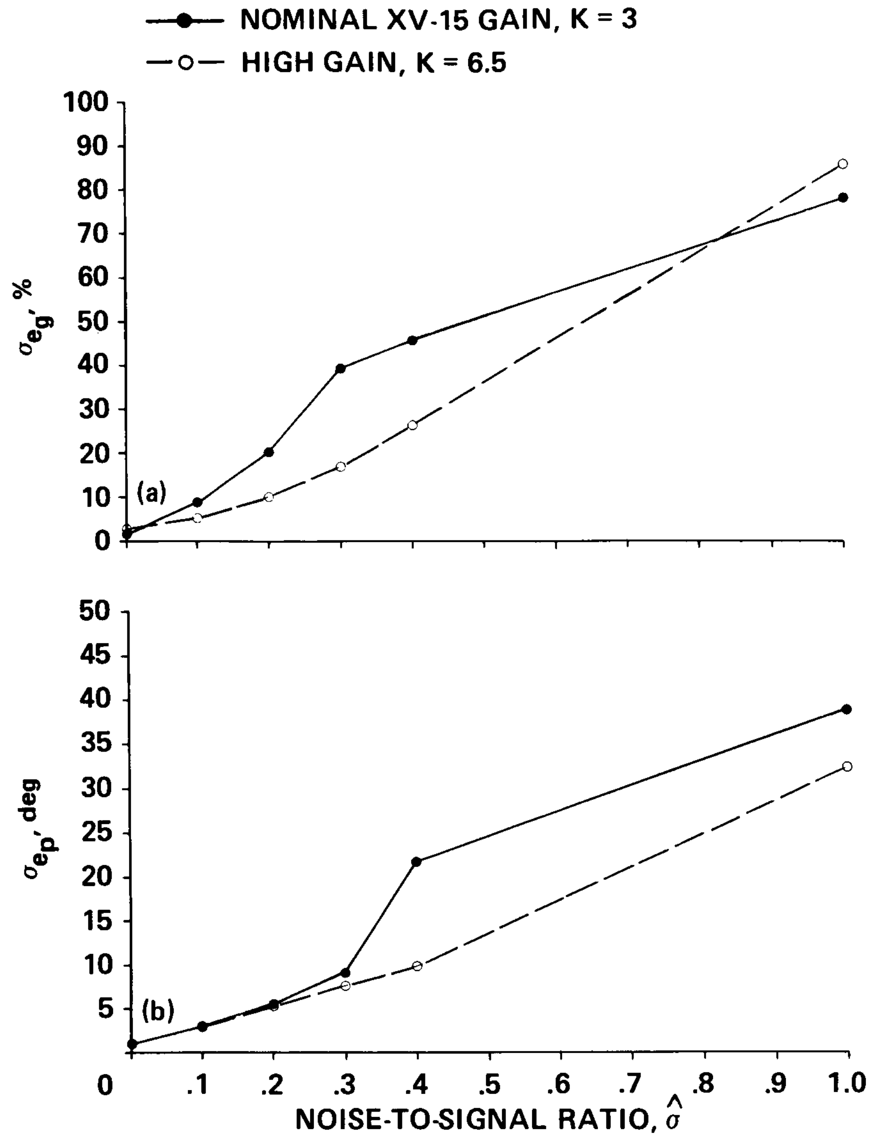

Fig. B.12. Variation in the Total rms Errors with Noise-to-Signal Ratio for the Identification of the Open-Loop Frequency-Response. (a) Magnitude Error; (b) Phase Error.

nominal and high-gain cases. Based on an allowable magnitude error of 10% (σ_{e_g} = 0.92 dB), the results of Fig. B.12a indicate that the noise-to-signal ratio should be $\hat{\sigma} < 0.11$ for the low-gain case and $\hat{\sigma} < 0.20$ for the high-gain case. Adopting the relative error weighting of 1 dB magnitude error to 7 deg phase error (Sec. 3.3.2) yields an allowable rms phase error $\sigma_{e_p} = 6.4$ deg (= 7 × 0.92 dB). Based on this phase error limit, the results of Fig. B.12b indicate an acceptable noise-to-signal ratio of $\hat{\sigma} < 0.22$ for the low-gain case and $\hat{\sigma} < 0.25$ for the high-gain case. Thus, the noise limits based on the magnitude criteria are more restrictive for this study. The larger allowable levels of noise for the high-gain case occur because the resulting closed-loop system is more resistant to excitation from process noise, thereby reducing the total level of random error. For large noise-to-signal ratios $\hat{\sigma} >> 1$, the magnitude errors asymtotically approach different levels for the two feedback gain cases because the associated inverse compensation gain values $-1/K$ are different. The rms phase errors approach a common value because the open-loop identification tends toward $\Phi = -180$ deg, independent of the gain level Eq. (B.20).

A direct measure of parameter bias error is obtained by fitting each of the frequency-responses in Fig. B.10 (and similarily for the high-gain case) with the first-order transfer-function model:

$$\hat{H} = \frac{K\,e^{-\tau s}}{s - a} \tag{B.22}$$

and tabulating the bias errors normalized with respect to the true open-loop transfer-function parameters of Eq. (B.17):

$$\begin{aligned} \varepsilon_b[\hat{K}] &= \frac{b[\hat{K}]}{K} = \left|\frac{K - 1}{1}\right| \times 100\% \\ \varepsilon_b[\hat{a}] &= \frac{b[\hat{a}]}{a} = \left|\frac{a - 0.5}{0.5}\right| \times 100\% \end{aligned} \tag{B.23}$$

The normalized bias errors for transfer-function gain $\epsilon_b[\hat{K}]$ and mode location $\epsilon_b[\hat{a}]$ are plotted in Figs. B.13a and B.13b. The small

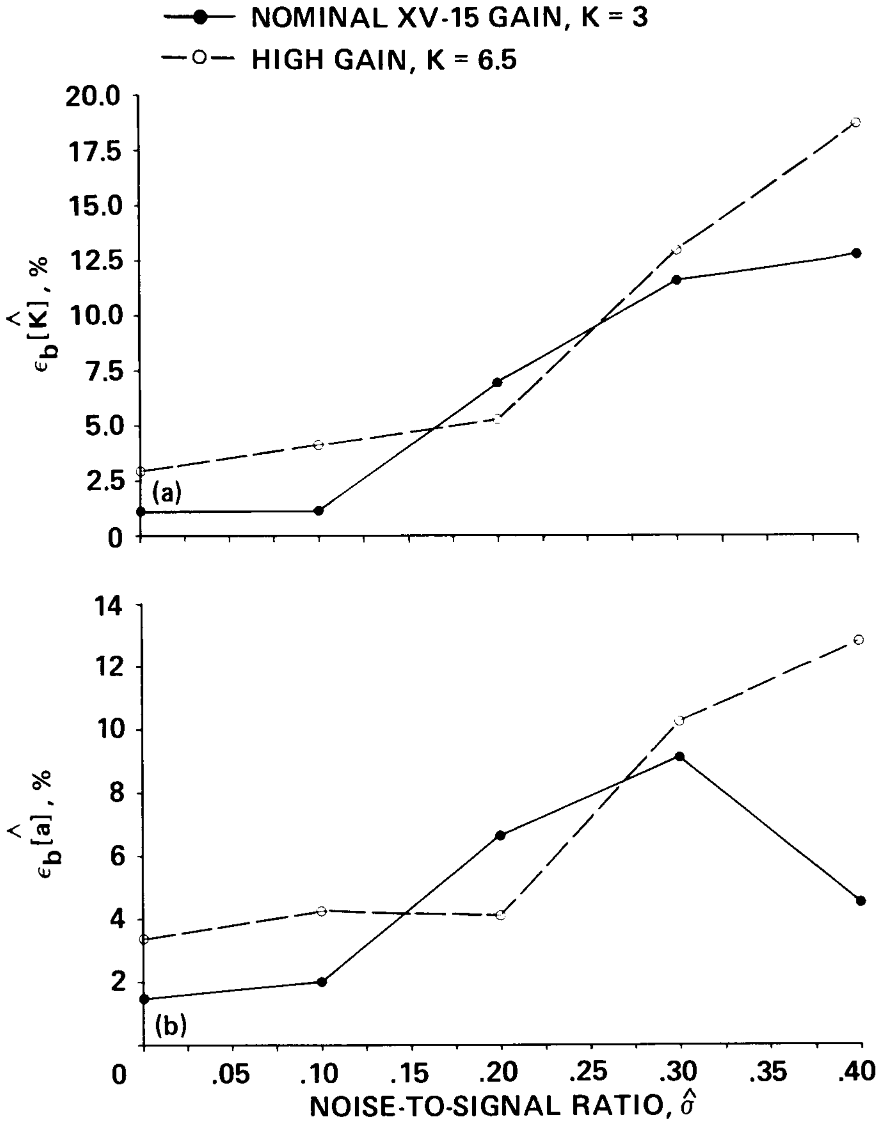

Fig. B.13. Variation in Normalized Bias Errors with the Noise-to-Signal Ratio for the Identification of the Open-Loop Frequency Response. (a) Normalized Gain Error; (b) Normalized Mode Location Error.

bias error for no process noise is associated with the overall spectral identification procedure (Ref. 28). The increase in bias error for the high-gain case at low process noise levels ($\hat{\sigma} < 0.1$) probably results from the integration errors which become more significant at the higher closed-loop natural frequencies. Restricting the maximum bias error (gain and mode) to within 10% indicates a requirement for noise-to-signal ratios of $\hat{\sigma} < 0.3$, which is in good agreement with the theoretical results of Eq. (B.16). The fact that the bias errors are very small for process noise ratios of $\hat{\sigma} < 0.10$ indicates that the random error contribution is the significant factor in the total rms error results of Fig. B.12a and B.12b. By limiting the noise ratio to $\hat{\sigma} < 0.10$ in order to maintain acceptable levels of total rms error, negligible bias errors are ensured.

B.3 Conclusions of Closed-Loop Identification Study

Two major conclusions can be drawn from this study of limitations on closed-loop identification:

1. Identifying the open-loop frequency-response from closed-loop flight data results in a biased estimate whenever process noise is present. Common sources of process noise which must be considered are turbulence, extraneous unaccounted for inputs, and nonlinearities.

2. Process noise causes random and bias errors in the estimates. Numerical studies based on the simplified model of XV-15 dynamics suggest that allowable levels of noise are determined more from the effects of random error than from those of bias error. Total error can be kept to an acceptable level when the noise-to-signal rms ratio is $\hat{\sigma} < 0.10$. Bias errors do not become important until process noise ratios reach $\hat{\sigma} > 0.3$. The coherence function is a good indicator of the level of total random error for low and moderate process noise

levels, and can be used to assess the quality of the open-loop frequency-response identification from closed-loop test data.

This relatively simple numerical simulation provides a good appreciation for the effects of process noise and closed-loop compensation. Similar studies should be conducted (perhaps using more sophisticated models of vehicle response and noise environment) to support future closed-loop identification experiments on rotorcraft.

REFERENCES

1. "Stability and Control and Handling Qualities Analysis," Vol. 2, V/STOL Tilt Rotor Research Aircraft, 301-199-002, Bell Helicopter Company, Fort Worth, Tex., 1973.

2. Harenda, P. B., Joglekar, M. J., Gaffey, T. M., and Marr, R. L., "A Mathematical Model for Real-Time Flight Simulation of the XV-15 Tilt Rotor Research Aircraft," NASA CR-114614, 1973.

3. Hanson, G. D. and Ferguson, S. W., "Generic Tilt-Rotor Simulation (GTRSIM) Users' and Programmers' Guide," NASA CR-166535 (NAS2-11317), 1983.

4. Churchill, Gary B. and Dugan, Daniel C., "Simulation of the XV-15 Tilt Rotor Research Aircraft," NASA TM-84222, 1982. (Also AVRADCOM TR 82-A-4, 1982).

5. Ferguson, Samuel W., Hanson, Gregory D., Churchill, Gary B., "Simulation Validation of the XV-15 Tilt-Rotor Research Aircraft," Paper A-84-40-09-4000, 40th Annual National Forum of the American Helicopter Society, Arlington, Va., 1984.

6. Chen, R. T. N. and Tischler, M. B., "The Role of Modeling and Flight Testing in Rotorcraft Parameter Identification," System Identification Session, 42nd Annual National Forum of the American Helicopter Society, Washington, D.C., June 1986.

7. Milliken, William F., "Progress in Dynamic Stability and Control Research," Journal of the Aeronautical Sciences, Vol. 14, No. 9, Sept. 1947, pp. 493-499.

8. Greenberg, Harry, "A Survey of Methods for Determining Stability Parameters of an Airplane from Dynamic Flight Measurements," NACA TN-2340, Apr. 1951.

9. Schofield, B. Lyle, Twisdale, Thomas R., Kitto, William G., and Ashurst, Tice A., "Development of Handling Qualities Testing in the 70's: A New Direction," AGARD Proceedings on Criteria for Military Handling Qualities of Military Aircraft, AGARD-CP-333, Apr. 1982.

10. Twisdale, Thomas R. and Ashurst, Tice A., Jr., "System Identification from Tracking (SIFT), A New Technique for Handling-Qualities Test and Evaluation" (initial report), AFFTC-TR-77-27, 1977.

11. Marchand, M. and Koehler, R., "Determination of Aircraft Derivatives by Automatic Parameter Adjustment and Frequency Response Methods," AGARD Conference on Methods for Aircraft and State and Parameter Identification, AGARD CP-172, 1975.

12. Hoh, R. H., Myers, T. T., Ashkenas, I. L., Ringland, R. R., and Craig, S., "Development of Handling Quality Criteria for Aircraft with Independent Control of Six Degrees of Freedom," Air Force Wright Aero Lab TR-81-3027, April 1981.

13. Jex, Henry R. and Mitchell, David G., "Stability and Control of the Gossamer Human-Powered Aircraft by Analysis and Flight Test," NASA CR-3627, 1982.

14. Hodgkinson, John, LaManna, W. J., and Heyde, J. L., "Handling Qualities of Aircraft with Stability and Control Augmentation Systems--A Fundamental Approach," Aeronautical Journal, Vol. 80, No. 782, Feb. 1976, pp. 75-81.

15. Bischoff, David E. and Palmer, Robert E., "Investigation of Low Order Lateral Directional Transfer Function Models for Augmented Aircraft," AIAA Paper 82-1610, San Diego, Calif., 1982.

16. Mitchell, David G. and Hoh, Roger H., "Low-Order Approaches to High-Order Systems: Problems and Promises," AIAA Journal of Guidance, Control, and Dynamics, Vol. 5, No. 5, 1982, pp. 482-489.

17. Hoh, Roger H., Mitchell, David G., Ashkenas, Irving L., Klein, Richard H., Heffley, Robert K., and Hodgkinson, J., "Proposed MIL Standard and Handbook--Flying Qualities of Air Vehicles, Vol. II: Proposed MIL Handbook," AFWAL-TR-82-3081, 1982.

18. Tischler, M. B., Leung, J. G. M., and Dugan, D. C., "Frequency-Domain Identification of XV-15 Tilt-Rotor Aircraft Dynamics in Hovering Flight," AIAA Paper 83-2695, AIAA/AHS 2nd Flight Testing Conference, Las Vegas, Nev., Nov. 1983. (Also published in condensed version in the Journal of the American Helicopter Society, Vol. 30, No. 2, April 1985, pp. 38-48).

19. "Draft Specifications and Background Information and User's Guide (BIUG) for Flying and Ground Handling Qualities of the LHX," WP-1194-5, Systems Technology, Inc., Hawthorne, Calif., Nov. 1984.

20. Tischler, M. B., Fletcher, J. W., Diekmann, V. L., Williams, R. A., and Cason, R. W., "Demonstration of Frequency-Sweep Testing Technique using a Bell 214-ST Helicopter," NASA TM-89422, 1987.

21. Hilbert, K. B., Lebacqz, J. V., and Hindson, W. S., "Flight Investigation of a Multivariable Model-Following Control System for Rotorcraft," 3rd AIAA/AHS Flight Testing Conference, Las Vegas, Nev., Nov. 1985.

22. Tischler, M. B. and Kaletka, J., "Modeling XV-15 Tilt-Rotor Aircraft Dynamics Using Frequency and Time-Domain Identification Techniques," Paper No. 9, AGARD Flight Mechanics Panel Symposium on Rotorcraft Design for Operations, Amsterdam, The Netherlands, Oct. 1986. (Also NASA TM-89405, 1986.)

23. Acree, C. W. and Tischler, M. B., "Using Frequency-Domain Methods to Determine XV-15 Aeroelastic Modes," in preparation, 1987.

24. Tischler, M. B., Leung, J. G. M., and Dugan, D. C., "Identification and Verification of Frequency-Domain Models for XV-15 Tilt-Rotor Aircraft Dynamics in Cruising Flight," AIAA Journal of Guidance, Control, and Dynamics, Vol. 9, No. 4, July-Aug. 1986, pp. 446-453.

25. Churchill, Gary B. and Gerdes, Ronald M., "Advanced AFCS Developments on the XV-15 Tilt Rotor Research Aircraft," Paper No. A-84-40-10-4000, 40th Annual National Forum of the American Helicopter Society, Arlington, Va., 1984.

26. Aponso, B. L., DiMarco, R. J., and Mitchell, D. G., "Obtaining Bandwidth from Frequency Sweep Data Using the STI Frequency Domain Analysis (FREDA) Package," Working Paper 1194-100-1, System Technology, Inc., Hawthorne, Calif., Sept. 1985.

27. Jex, H. R., Hogue, J. R., Magdaleno, R. E., and Gelhausen, P. A., "Dynamic Flight-Tests of the Skyship-500 Airship," TR-1151-4, System Technology, Inc., Hawthorne, Calif., Mar. 1986.

28. Bendat, Julius S. and Piersol, Allan G., Random Data: Analysis and Measurement Procedures, 2nd ed., John Wiley and Sons, Inc., New York, 1986.

29. Otnes, Robert K. and Enochson, Loren, Applied Time Series Analysis, John Wiley and Sons, Inc., New York, 1978.

30. Rabiner, Lawrence R. and Gold, Bernard, Theory and Application of Digital Signal Processing, Prentice-Hall, Inc., Englewood Cliff, N.J., 1975.

31. Carter, Clifford G., Knapp, Charles H., and Nuttall, Albert H., "Estimation of the Magnitude-Squared Coherence Function Via Overlapped Fast Fourier Transform Processing," IEEE Transaction on Audio and Electroacoustics, Vol. AU-21, No. 4, Aug. 1973, pp. 337-344.

32. Rabiner, Lawrence R., Schafer, Ronald W., and Rader, Charles M., "The Chirp z-Transform Algorithm and Its Application," The Bell System Technical Journal, May-June 1969, pp. 1249-1292.

33. Graham, Dunstan and McRuer, Duane T., Analysis of Nonlinear Control Systems, Dover Publications Inc., 1971.

34. Bendat, Julius S. and Piersol, Allan G., Engineering Applications of Correlation and Spectral Analysis, John Wiley & Sons, Inc., New York, 1980.

35. Wingrove, Rodney C. and Edwards, Frederick G.," A Technique for Identifying Pilot Describing Functions From Routine Flight-Test Records," NASA TN D-5127, 1969.

36. Corliss, Lloyd D. and Carico, G. Dean, "A Preliminary Flight Investigation of Cross-Coupling and Lateral Damping for Nap-of-the-Earth Helicopter Operations," Paper No. 81-28, 37th Annual National Forum of the American Helicopter Society, New Orleans, La., 1981.

37. Hodgkinson, J. and Buckley, J., "NAVFIT General Purpose Frequency Response Curve Fit (Arbitrary Order)," McDonnell Aircraft Company, St. Louis, Mo., Oct. 1978.

38. Givan, M. E., LaManna, W. J., and Hodgkinson, J., LONFIT User's Guide, McDonnell Aircraft, St. Louis, Mo., 1978.

39. Givan, M. E., LaManna, W. J., and Hodgkinson, J., LATFIT User's Guide, McDonnell Aircraft, St. Louis, Mo., 1978.

40. Tayler, L. W., Jr., "Application of a New Criterion for Modeling Systems," AGARD-CP-172, Nov. 1974.

41. McRuer, Duane T., Ashkenas, Irving L., and Graham, Dunstan, Aircraft Dynamics and Automatic Control, Princeton University Press, Princeton, N.J., 1973.

42. Johnson, Wayne, Helicopter Theory, Princeton University Press, Princeton, N.J., 1980.

43. Hoh, Roger H. and Ashkenas, Irving L., "Development of VTOL Flying Qualities Criteria for Low Speed and Hover," NADC-77052-30, 1979.

44. Heffley, Robert K., "A Compilation and Analysis of Helicopter Handling Qualities Data, Vol. 2, Data Analysis," Systems Technology, Inc., Hawthorne, Calif. (Also, NASA TR-1087-2, 1979.)

45. Wolkovitch, J. and Johnston, D. E., "Automatic Control Considerations for Helicopter and VTOL Aircraft with and without Sling Loads," STI TR 138-1, Systems Technology, Inc., Hawthorne, Calif., Nov. 1965.

46. Etkin, Bernard, "The Turbulence Wind and Its Effect on Flight," (AIAA Wright Brothers Lecture, 1980), UTIAS Review 44, Aug. 1980.

47. Chen, Robert T. N., "Transfer-Characterization and the Unique Realization of Linear Time-Invariant Multivariable Systems," Cornell Aeronautical Laboratory, Inc., 1972 Joint Automatic Control Conference of the American Automatic Control Conference, Stanford, Calif., Aug. 1972.

NASA
National Aeronautics and Space Administration

Report Documentation Page

1. Report No. NASA TM 89428 USAAVSCOM TM-87-A-1	2. Government Accession No.	3. Recipient's Catalog No.

4. Title and Subtitle

Frequency-Response Identification of XV-15
Tilt-Rotor Aircraft Dynamics

5. Report Date

May 1987

6. Performing Organization Code

7. Author(s)

Mark B. Tischler

8. Performing Organization Report No.

A-87103

10. Work Unit No.

505-61-51

9. Performing Organization Name and Address

Aeroflightdynamics Directorate, U.S. Army
Aviation Research and Technology Activity,
Ames Research Center, Moffett Field, CA 94035 and
Ames Research Center, Moffett Field, CA 94035

11. Contract or Grant No.

12. Sponsoring Agency Name and Address

National Aeronautics and Space Administration
Washington, D.C. 20546 and
United States Army Aviation Systems Command
St. Louis, Missouri 63120

13. Type of Report and Period Covered

Technical Memorandum

14. Sponsoring Agency Code

15. Supplementary Notes

Point of contact: Mark B. Tischler, Ames Research Center, MS 211-2, Moffett Field, CA 94035 (415) 694-5563 or FTS 464-5563

16. Abstract

The timely design and development of the next generation of tilt-rotor aircraft (JVX) depend heavily on the in-depth understanding of existing XV-15 dynamics and the availability of fully validated simulation models. Previous studies have considered aircraft and simulation trim characteristics, but analyses of basic flight vehicle dynamics have been limited to qualitative pilot evaluations. The present study has the following objectives: (1) documentation and evaluation of XV-15 bare-airframe dynamics, (2) comparison of aircraft and simulation responses, and (3) development of a validated transfer-function description of the XV-15 needed for future studies. A nonparametric frequency-response approach is used which does not depend on assumed model order or structure. Transfer-function representations are subsequently derived which fit the frequency responses in the bandwidth of greatest concern for piloted handling-qualities and control-system applications.

17. Key Words (Suggested by Author(s))

Flight test; Parameter identification;
Rotorcraft; XV-15; Tilt-rotor;
Simulation

18. Distribution Statement

Unclassified-Unlimited

Subject category: 08

19. Security Classif. (of this report) Unclassified	20. Security Classif. (of this page) Unclassified	21. No. of pages 189	22. Price A09

NASA FORM 1626 OCT 86

For sale by the National Technical Information Service, Springfield, Virginia 22161

GPO 787-804/79158